

Walking on virtual ground: physics, perception, and interface design

Yon Visell



Department of Electrical & Computer Engineering
McGill University
Montreal, Canada

March 2011

A thesis submitted to McGill University in partial fulfillment of the requirements for the degree of Doctor of Philosophy.

© 2011 Yon Visell

Abstract

The sensorimotor capacities of the foot are crucial to human locomotion in diverse environments, to gathering information about walking surfaces, and to interacting with objects on the ground. Locomotion is increasingly employed to allow users to control and navigate within immersive virtual environments, but, in contrast to the hand, little attention has been given to the rendering of haptic sensations for the feet.

This thesis addresses several challenges motivated by the problem of realizing haptic experiences of walking on virtual ground surfaces. First, a novel family of interfaces is introduced, based on a vibrotactile display integrated in a rigid floor plate. Its structural dynamics and controller have been optimized to ensure its ability to accurately reproduce mechanical vibrations over a wide frequency band, which was instrumental to realizing the perceptual study presented in the second part of the thesis. Distributed arrays of these devices are used to simulate virtual ground surfaces and floor-based multi-touch surfaces, whose usability for human-computer interaction is empirically demonstrated.

The second component of this thesis is an experimental study of the contribution of vibrotactile sensory information to the perception of ground surface compliance. A novel haptic perceptual illusion is demonstrated, in which the apparent compliance of a floor surface is increased by vibrations felt via the plantar sole of the foot. This investigation also revealed the surprising ability of the vibrotactile floor interface to overcome, in part, a core limitation: its inability to display kinesthetic force-displacement information.

The third part of the thesis analyzes texture-like mechanical signals produced through inelastic physical processes in complex, disordered materials like those encountered during walking in many natural terrains. Patterns of fluctuations accompanying sliding friction and fracture processes in quasi-brittle, heterogeneous materials subjected to time-varying loads are characterized using methods from statistical physics. This analysis was used to formulate novel algorithms for the haptic synthesis of high-frequency signatures of fracture processes in fiber composites and compressed granular media.

In conclusion, this thesis presents an innovative hardware interface and techniques for interacting with virtual ground surfaces. It also demonstrates a new haptic perceptual effect that lends justification to the display paradigm adopted here. Finally, it analyzes and models transient, texture-like physical phenomena associated with stepping onto complex, natural ground materials.

Résumé

Les capacités sensori-motrices du pied sont essentielles à la locomotion humaine, à la collecte d'informations sur les surfaces de marche, et à l'interaction avec des objets au sol. La locomotion est de plus en plus utilisée pour interagir et naviguer dans les environnements virtuels immersifs, mais, contrairement à la main, peu d'attention a été accordée au rendu des sensations haptiques pour les pieds.

Cette thèse aborde plusieurs problèmes liés à la réalisation d'expériences haptiques de marche sur des terrains virtuels. Tout d'abord, une nouvelle famille d'interfaces est présentée, fondée sur un dispositif vibrotactile intégré dans un carreau rigide. Sa dynamique structurelle et son contrôleur ont été optimisés pour assurer sa capacité à reproduire fidèlement les vibrations mécaniques dans une large bande de fréquence, ce qui était nécessaire à la réalisation de l'étude de perception présentée en deuxième partie de la thèse. Un pavage de ces dispositifs est utilisé pour simuler des terrains virtuels et des planchers tactiles multi-points, dont l'ergonomie est démontrée de manière empirique.

Le deuxième volet de cette thèse est une étude expérimentale sur la contribution de l'information vibrotactile à la perception de la compliance du sol. Une nouvelle illusion perceptuelle haptique est démontrée, dans laquelle la compliance apparente du sol est augmentée par les vibrations ressenties par la plante du pied. Cette étude a également révélé l'étonnante capacité de l'interface vibrotactile à surmonter, en partie, une limitation intrinsèque : son incapacité à transmettre des informations kinesthésiques force-déplacement.

La troisième partie de la thèse analyse les signaux mécaniques complexes produits par les processus physiques inélastiques dans les matériaux désordonnés tels que ceux rencontrés lors de la marche en terrain naturel. Les modèles de fluctuations accompagnant le frottement de glissement et les processus de fracture dans les matériaux hétérogènes quasi-fragiles soumis aux charges variables sont caractérisés par des méthodes de physique statistique. Cette analyse est utilisée pour formuler de nouveaux algorithmes pour la synthèse haptique des signatures à hautes fréquences des processus de fracture dans les composites de fibres et les matériaux granulaires compressés.

En conclusion, cette thèse présente un dispositif vibrotactile et des techniques novateurs pour interagir avec des terrains virtuels. Elle démontre un nouvel effet perceptuel qui justifie le paradigme d'interaction haptique adopté ici. Enfin, elle analyse et modélise certains phénomènes physiques associés à la marche sur des terrains naturels complexes.

Acknowledgments

This thesis would not have been possible without the support of my colleagues, mentors, and friends. I would like to thank Prof. Jeremy Cooperstock for his supervision, and for his openness and enthusiastic support of this research despite changes in its direction. A number of colleagues at McGill collaborated with me on this work and greatly enriched it. Bruno Giordano, a collaborator on the study presented in Chapter 6, taught me a great deal about perception and experimental rigour. Guillaume Millet was often the one ready to ask questions that weren't being raised. He collaborated on the experiments of Chapter 6, and also provided valuable input on the material simulations presented in Chapter 7. Work by Alvin Law, Severin Smith, and Jessica Ip was instrumental to realizing the multimodal floor interface described in Chapter 5. I would like to thank all of members of the Shared Reality Environments lab for sharing their own energies and realities over the last few years.

I received vital input and encouragement at critical moments from members of my PhD committee, Prof. Vincent Hayward, Prof. Marcelo Wanderley, and Prof. Stephen McAdams. Special thanks to the staff in the Centre for Intelligent Machines and in the Centre for Interdisciplinary Research in Music Media and Technology, especially Cynthia Davidson, for helping everything to run smoothly, and to Don Pavlasek of the mechanical workshop, who provided helpful consulting and assistance with fabrication. Prof. Luc Devroye offered generous advice on the subtleties of random variate generation. External collaborators including Nizar Ouarti, Federico Fontana, Gabriel Cirio, Anatole Lécuyer, and Maud Marchal provided useful and stimulating discussion related to this work.

This research received support from the Québec Ministère du Développement économique, de l'Innovation et de l'Exportation (MDEIE) for the European Community 7th Framework Programme project Natural Interactive Walking (NIW, no. 222107), from the the European Community 6th Framework Programme project CLOSED (no. 029085), from student research awards from the Centre for Interdisciplinary Research in Music Media and Technology, and from an entrance award and international graduate student fellowships from the Department of Electrical and Computer Engineering.

I thank Karmen Franinović for lending me her support and inspiration, and for being my best collaborator on everything outside of this thesis.

Contents

1	Introduction	1
1.1	Scope	3
1.2	Overview	3
1.3	Summary of contributions	6
2	Background	9
2.1	Dynamics and forces in walking	9
2.2	Mechanical interactions and materials	11
2.3	Vibrotactile sensation and perception	11
2.4	Display and interaction techniques	13
2.4.1	Walking in virtual worlds	14
2.4.2	The foot in human-computer interaction	15
2.5	Vibrotactile interfaces and physically based synthesis	16
2.5.1	Hardware	16
2.5.2	Physically based synthesis	18
3	Floor Surfaces as Ambient Haptic Interfaces	21
3.1	Introduction	23
3.1.1	Potential Advantages	25
3.2	Background	26
3.2.1	Tactile sensation and psychophysics of the foot	26
3.2.2	Prior research on interfaces for the feet	28
3.3	Ambient haptic floors: display design	30
3.3.1	Roles for haptic communication	31
3.3.2	Physical interaction design considerations	32

3.3.3	Prototyping technologies and methods	32
3.3.4	Prototype vibrotactile device	34
3.3.5	Temporal interaction design considerations	35
3.3.6	Three interaction cases	36
3.3.7	Vibrotactile stimulus design	37
3.4	Evaluation	41
3.4.1	Methodology	42
3.4.2	Results and Discussion	43
3.5	Conclusion	48
4	Vibrotactile Display Design	51
4.1	Introduction	53
4.1.1	Vibrotactile augmentation of floor surfaces	53
4.1.2	Background	54
4.2	Display concept and motivation	55
4.2.1	Transparency	56
4.2.2	Application to normal force texture simulation	57
4.3	Components	58
4.3.1	Mechanical Structure	58
4.3.2	Sensing	59
4.3.3	Actuation	60
4.3.4	Electronics	60
4.4	Dynamic Response	61
4.4.1	Actuator Response	61
4.4.2	Plate Response	61
4.4.3	Elastic Suspension	65
4.4.4	Simulation	67
4.4.5	Modeling user-supplied loads	68
4.5	Evaluation	69
4.5.1	Frequency response measurement	70
4.5.2	Digital correction	71
4.6	Conclusion	71

5	Interaction Techniques	75
5.1	Introduction	77
5.2	Background	77
5.2.1	Floor Touch User Interfaces: Potential application space	78
5.3	System	79
5.4	Contact sensing	80
5.5	Channeling material interactions	83
5.5.1	Non-visual rendering	83
5.5.2	Visual animation and control	85
5.6	Floor Touch Surface Interfaces	86
5.6.1	Preliminary User Evaluation	87
5.7	Conclusions	90
6	Vibration Increases Haptic Perception of Surface Compliance	93
6.1	Abstract	95
6.2	Introduction	95
6.3	Materials and Methods	98
6.3.1	Ethics Statement	98
6.3.2	General Methods	99
6.3.3	Apparatus	99
6.3.4	General Procedure	99
6.3.5	Experiment 1	101
6.3.6	Experiment 2	105
6.4	Results	110
6.4.1	Vibration Stimulus Factors Influencing Subjective Compliance Judgments	110
6.4.2	Effect of Vibration Feedback on Compliance Perception	112
6.5	Discussion	116
7	Simulating Fracture Processes in Heterogeneous Materials	121
7.1	Introduction	122
7.2	Fracture processes in fiber composites: Fiber Bundle Model	124
7.2.1	Stochastic process formulation	126

7.2.2	Mean damage approximations	129
7.2.3	Numerical simulations	131
7.3	Stress fluctuations in compressed granular media	133
7.3.1	Inverse Fiber Bundle Model	134
7.3.2	Sequential algorithm and mean damage approximation	137
7.3.3	Numerical simulations	139
7.4	Real-time, interactive simulation	140
7.5	Conclusions	143
8	A first passage time problem associated with stick-slip oscillations	145
8.1	Introduction	146
8.2	Stick-slip motion as a first passage time problem	148
8.2.1	Approximate slip time densities	151
8.2.2	Joint first passage densities	153
8.2.3	Upcrossing densities	155
8.3	Stick-slip motion in a Langevin friction model	156
8.3.1	Upcrossing density	157
8.3.2	Results	159
8.4	Conclusion	166
9	Conclusions	167
9.1	Results	167
9.1.1	Devices	167
9.1.2	Information Display and Interaction Techniques	168
9.1.3	Perception	169
9.1.4	Mechanical Interactions	169
9.2	Future Work	170
	References	173

List of Figures

2.1	Vibration spectrogram $a(t, f)$ and low-frequency normal foot-ground force $F(t)$ measured at the hard sole of a men’s shoe during one footstep of a walker onto rock gravel.	10
3.1	A possible end-user scenario: Pedestrians receive vibrotactile cues via the ground surface, indicating the location of the crossing and state of its signal.	24
3.2	Image and diagram of the interactive, four-tile floor interface.	34
3.3	A 2×2 tile prototype seen from above. Force sensing resistors are positioned as shown.	35
3.4	Pictorial representations of three interaction paradigms.	37
3.5	The eight rhythms (R1 to R8) from which both sets of stimuli were built.	38
3.6	Waveforms used to generate the vibrotactile stimuli used in the experiment.	40
3.7	Example of a stimulus used in the experiment, resulting from the model settings that produced the first “impact” waveform of Figure 3.6 in combination with the first rhythmic pattern of Figure 3.5.	41
3.8	Correct identification rates for each vibrotactile message set.	44
3.9	Confusion pattern within the set of eight WS stimuli and the set of eight IT stimuli.	44
3.10	Mean correct identification rates in each session. The error bars show 95% confidence intervals.	45
3.11	Box plot summary of the mean correct identification rate for the IT (left side) and WS (right side) stimulus sets.	46
4.1	The experience of stepping onto a deformable object or surface is simulated via a rigid vibrotactile interface.	55

4.2	The haptic display concept.	56
4.3	Vibration spectrogram $a(t, f)$ and normal force $F(t)$ measured from one footstep onto rock gravel.	57
4.4	Normal force texture synthesis.	58
4.5	Vibrotactile floor interface hardware for a single tile unit.	59
4.6	Typical acceleration frequency response of the Clark Synthesis TST family of actuators.	61
4.7	Composite sandwich plate, shown in profile.	63
4.8	The suspension and tile system.	65
4.9	Resonant suspension frequency f_0 and static deflection δz vs. Young's modulus.	66
4.10	Visualization of the first two resonant modes of vibration.	67
4.11	FEM analysis of the acceleration response measured at four different points on the plate.	68
4.12	A simplified model of a user supplied load on the device.	69
4.13	The measured log magnitude frequency response of the display.	70
4.14	Corrected and uncorrected device response, without foot contact.	72
5.1	The floor interface, as situated within an immersive, rear projected virtual environment simulator.	79
5.2	Diagrammatic view of the floor interface.	80
5.3	Overview of system components and logical connections between them.	80
5.4	The normal force distribution $p_R(\mathbf{x})$ and associated contact centroid position \mathbf{x}_c	82
5.5	Results of 50 measurements comparing true normal force positions (circles) with contact centroid estimates (Xs).	82
5.6	A recorded sequence of contact centroids produced by an individual walking across the floor.	83
5.7	Still images of users interacting with the simulated frozen pond.	83
5.8	Behavior at the crack front \mathbf{c}_k is modeled using a simplified fracture mechan- ics treatment.	84
5.9	A crack pattern, modeled as a graph of lines between nodes \mathbf{c}_i extending from the seed location p_0	85
5.10	Still image from video of a user interacting with floor-based interface widgets.	86

5.11	Configuration and stimuli used in the floor touch surface experiment. . . .	88
5.12	Successful target selection rate vs. distance, angle of presentation (measured away from preferred foot), and button width, inclusive and exclusive of the farthest targets.	89
6.1	Apparatus for producing compliance and vibration stimuli.	100
6.2	Vibration feedback stimuli.	102
6.3	View of the variable compliance mechanism.	106
6.4	Force-displacement profiles and fits of stiffness vs. foam position used to calibrate the apparatus.	107
6.5	Experiment 1: Subjective compliance ratings for all 19 stimuli, averaged across subjects.	111
6.6	Experiment 1: Average compliance ratings for the three stimulus factors. .	111
6.7	Experiment 2: Mean proportion of comparison stimuli judged stiffer than the standard.	112
6.8	Experiment 2: Median values of the PSE and slope from per-subject psychometric fits at each vibration amplitude level.	114
6.9	Experiment 2: Psychophysical amplitude detection thresholds and response proportions at 90 N/mm.	115
7.1	Fiber Bundle Models have been successfully used to model fracture physics in quasi-brittle materials including fiber composites such as wood (left), and granular media, such as sand or gravel (right).	123
7.2	Fiber Bundle Model of fracture in a parallel array of N brittle fibers. . . .	125
7.3	The sequential sampling algorithm described equations (7.2-7.4).	128
7.4	Illustration of the mean damage model.	129
7.5	Typical stress-controlled loading responses of the Fiber Bundle Model. . .	131
7.6	The constitutive stress-strain relationship $\sigma(x)$ for models M , \tilde{M} , and \bar{M} . .	133
7.7	Statistical distribution of times between failure events.	134
7.8	Empirical distribution of the energy E of fracture fluctuations.	135
7.9	Granular flow through a tube can become obstructed by large forces resulting from force chains bridging the walls.	136

7.10	The inverse fiber bundle effectively models a compressed granular medium as a parallel array of fibers, which represent the percolation of one-dimensional force chains through the medium.	136
7.11	Compression results in rapid events through which force chains are restructured, becoming stronger, stiffer and straighter.	137
7.12	Response of the inverse Fiber Bundle Model under ramp loading conditions.	139
7.13	Empirical distribution of times between failure events, Δt and the size of energy fluctuations E	140
7.14	The response of a bundle of 2000 fibers to a dynamic load, simulating that due to a footstep.	141
7.15	Representative data from the interactive implementation of Fiber Bundle Model M . Data shown corresponds to a model with 350 fibers. Acoustic transfer is simulated by a resonant filter with 10 modes. Left column, Top to Bottom: Force input $F(t)$, strain $x(t)$, threshold $\xi(t)$, and time-frequency spectrogram of acoustic energy of fracture. Right: Fracture event waveform.	142
7.16	The simulation of high-frequency failure processes in localized domains within a distributed medium.	144
8.1	A viscoelastic body sliding across a surface, an example of a system that exhibits frictional stick-slip oscillations.	147
8.2	Phase-space portraits for three model friction laws.	149
8.3	152
8.4	Two phase space trajectories $(x(t), v(t))$ for the stochastic harmonic oscillator system.	160
8.5	The first upcrossing density, $n_1(t)$, which describes the level crossing behavior of the system in the absence of absorption from to slip-to-stick transitions.	161
8.6	Comparison of two different analytic approximations for the first passage time density.	162
8.7	Comparisons of the analytic approximation $\mathcal{F}_g^{(1)}(T)$ with simulation results.	163
8.8	The distribution of stick-slip oscillation periods.	163
8.9	Noise-driven excitation of stick-slip oscillations.	164
8.10	The distribution $p(d)$ of slip displacements: analytical result and Monte Carlo estimate.	165

List of Tables

6.1	Peak and RMS amplitudes of plate acceleration G for the high amplitude $A = 1.0$ vibration stimuli.	105
6.2	Experiment 2: Mean proportions of comparison stimuli that were judged to be stiffer than the standard.	113
6.3	Experiment 2: Median values of the PSE, slope, and intercept from per-subject psychometric curve fits at each vibration level.	114

Chapter 1

Introduction

Our feet are instruments of action and of self-motion, but are also used to perceive our surroundings through the sense of touch. Although tactile perception is finest in the hand, it is also highly developed in the lower extremities. The foot is capable of experiencing most of the range of haptic sensations that are felt via the hand, including kinesthesia (the sense of force and position) and cutaneous sensations including pain, temperature, and vibration. Arguably, the foot is the most often used haptic sensory organ, in the sense that it is nearly always active in touching the ground, regulating balance and locomotion. In this respect, it is one of the most important sources of haptic information about our surroundings.

Haptics plays a distinguished role relative to the other senses, as an important component of it is the bidirectional interaction with our physical surroundings, which, in the case of the foot, largely manifests as self-motion. A diverse variety of ground surfaces and features are encountered during everyday walking activities. Walking and interacting on foot generate a rich variety of multimodal information, much of it available through touch. This information is used to aid motor tasks with the feet, and to identify our surroundings. Nonetheless, the nature of haptic perception in the foot is less understood than in the case of the hand, having mainly been studied in relation to its effects on balance and locomotion.

Haptic interfaces for human-computer interaction have advanced greatly in the last two decades, but lag far behind visual and auditory displays. One reason is the difficulty involved in specifying and displaying haptic stimuli, which consist of forces or displacements distributed on the body surface and the dependence of these signals on body movements during interaction with objects in the environment. The large range and variety of signals

to which the haptic sense is sensitive amplifies this challenge. Existing interfaces are the result of severe tradeoffs concerning what aspects of haptic interaction are perceptually most important, which can be implemented most efficiently, and what paradigms are most useful or most likely to proliferate.

Just as walking is fundamental to the negotiation of natural environments, it is increasingly relevant to human-computer interaction, because immersive interactive systems are becoming more widely used, and because more everyday environments are being augmented with digital technology. Despite the important role played by the feet in numerous human activities, they have received limited attention as a means of interacting with computers.

Although rarely incorporated in early research on virtual environments, walking is increasingly investigated as a means of navigating in immersive virtual spaces, and has been found to have a positive effect on the sense of presence. However, despite remarkable advances in visual display and rendering techniques, little has been done to ensure that the haptic information users obtain about their surroundings through walking agrees with what they experience through the other senses.

The few haptic interfaces for the foot that have been developed have largely been designed to enable locomotion in virtual environments. Existing devices, which are based on similar principles to those used in motorized exercise equipment, have been used to simulate walking, running, turning, or other aspects of locomotion on uneven terrain. However, to date, almost no attention has been given to the simulation of other ground material properties. Indeed, no haptic interface is useful for displaying all possible force signals, and those that simulate kinesthetic aspects of locomotion, which involve large forces and body movements, are ill-suited to reproducing finer textural details that distinguish various natural and man-made ground surfaces.

Vibrotactile interfaces, which are designed to mirror the haptic subsystem that is most sensitive to fast or high-frequency mechanical stimuli, offer a complementary alternative. They are low in cost and complexity, because they are electronically and mechanically simple and can often be operated in open loop control mode. Although unable to simulate kinesthetic information, they have proven effective at rendering object properties, such as surface hardness and texture, that are reflected through high-frequency mechanical vibrations, and are poorly reproduced by most force-feedback devices.

However, little is known about the nature of vibrotactile stimuli that are produced during walking on natural ground surfaces, which include materials that are rarely used

in haptic simulations. Common examples, such as branches, snow, sand, or gravel, are heterogeneous, collective, and disordered, and the complex, inelastic mechanical responses that they exhibit when subjected to loads are responsible for the textural “feel” of walking on them. It appears to be computationally unfeasible to interactively simulate these distributed processes on a microscopic scale, due to the number of elements involved and to their complex organization. Effective statistical models have been developed in the science and engineering literature, but have not yet been applied to haptic rendering.

1.1 Scope

This thesis is motivated by the aim of allowing users to walk on and “feel” natural or man-made ground surfaces that are simulated in a virtual environment. The virtual ground surface is simulated by means of haptic (and, optionally, auditory or visual) feedback provided by a real, instrumented floor. The sensation of touching a virtual surface is produced by modifying the displacement of the floor in response to forces exerted by the foot. As a practical measure, only texture-like, high-frequency temporal components are displayed, because it is far less efficient to reproduce static forces or displacements. Thus, the simulation is based primarily on vibrations presented and felt through a flat, instrumented floor display.

The thesis addresses several problems motivated by this basic scenario. It presents the design of a novel vibrotactile floor interface and uses it to realize virtual ground and touch surface interfaces. It also investigates the contribution of vibrotactile sensory information to the perception of ground surface properties, and demonstrates that vibrotactile feedback can, to some extent, compensate for missing kinesthetic information. This seems to be attributable to the fact that the displacement of many natural materials or mechanisms is accompanied by texture-like vibrations that are produced through inelastic processes like friction and fracture. The manifestation of these processes in some disordered materials, like those found in natural ground surfaces, is analyzed using tools from stochastic physics.

1.2 Overview

This thesis is organized in nine chapters: this introduction, a review of prior literature, three previously published manuscripts, three chapters (not yet submitted for publication),

and a summary.

Chapter 2 provides a survey of prior literature relevant to the realization of experiences walking on, or interacting with, virtual ground surfaces. It contains an overview of relevant aspects of locomotion, a survey of vibrotactile sensation and perception in the feet, a discussion of mechanical interactions in walking on natural and man-made surfaces, a review of prior literature on human-computer interaction via the feet, a discussion of factors affecting the design of vibrotactile interfaces, and a review of methods for the physically based rendering of vibrotactile stimuli. Due to the breadth of the topics involved, further background is reviewed in the relevant sections of the chapters that follow.

Chapter 3 presents applications of a novel vibrotactile floor display to ambient information display in intelligent environments. Potential applications of such displays as navigational aids, non-intrusive information conduits, aids to visually impaired people, entertainment features, and components of immersive virtual environments are discussed. Two methods for the design of vibrotactile messages presented through a floor interface are presented and evaluated in an experiment. The results support the feasibility of ambient vibrotactile information display through floor surfaces, and provide guidelines for the design of usable vibrotactile messages.

Chapter 4 presents the re-engineered design of the vibrotactile floor interface, which was used in other chapters of this thesis to implement and evaluate interaction techniques and rendering algorithms for virtual ground surfaces. The most notable part of this chapter is the consideration given to optimizing the structural dynamics of the device subject to constraints imposed by the need to support static loads from users standing on it. Digital inverse filtering is used to further correct the unloaded device transfer function response, achieving a flat passband from 50 to 750 Hz, and making it well suited for use in the perceptual investigation conducted in Chapter 6.

Chapter 5 investigates new techniques for interacting with computationally augmented floor surfaces. It introduces a distributed, networked version of the vibrotactile floor interface presented in Chapters 3 and 4. Interaction techniques are developed for this distributed display, based on intrinsic contact sensing methods that make it possible to resolve foot-floor contact loci with a resolution of about 2 cm. They are used to realize interactive, multi-

modal simulations of natural walking terrains and multimodal touch surface interfaces for human-computer interaction. A usability evaluation was conducted, yielding preliminary guidelines for the design of such applications.

Chapter 6 presents a study that directly addresses an inherent limitation of the vibrotactile floor interface: its inability to display kinesthetic force-displacement information, hence to reproduce the compliant feel of different ground surfaces. A new haptic perceptual illusion is demonstrated, in which the perceived compliance of a floor surface is increased by vibration feedback felt through it. A series of experiments revealed that the effect scales monotonically with vibration amplitude, and is robust at amplitudes near to the psychophysical detection threshold for the stimuli. The results suggest that vibrotactile channels play a larger role in the control of locomotion than has been previously acknowledged.

Chapter 7 and **Chapter 8** investigate mechanical interactions associated with experiences of walking on disordered, heterogeneous materials like those commonly encountered in natural environments. Although Chapters 4 and 5 presented simple stochastic models for rendering texture-like vibrations associated with the inelastic compression of such materials, here a more fundamental basis for such algorithms is provided, based on statistical physics.

Chapter 7 presents and analyzes a novel methods for simulating failure processes in fiber reinforced composites and granular materials subjected to dynamic loads. An efficient, temporal model for these fracture-like processes is derived based on a stochastic process associated with random spatial variations in the local strain thresholds of a distributed medium.

Chapter 8 analyzes irregular stick-slip motion produced through frictional sliding or compression of rough or disordered surfaces, using methods from statistical physics. A novel first passage time problem is formulated, whose solutions determine the statistical properties of stick-slip motion in a generic class of stochastic friction models. Approximate solutions to this problem are developed here for the first time. They are shown to capture rich, pseudo-periodic motions that are not present in any deterministic limit, but instead correspond to noise activated transient oscillation modes similar to those associated with stochastic resonance phenomena observed in other physical and biological systems.

Chapter 9 concludes this thesis with a summary and a discussion of the main findings and implications for future research.

The novel aspects of this thesis involve hardware interface design, interaction techniques, models of material responses, and perception. The perceptual investigation provided a validation of the ability of the vibrotactile floor surface to simulate a key aspect of different ground surfaces. In addition, it can be regarded as a worst case assessment of the display paradigm proposed here, since it focused on a perceptual dimension that was, a priori, compromised in the original design. The possibility it demonstrated, of using vibrotactile feedback to evoke an illusory sense of compliance, was an unexpected outcome of this thesis.

1.3 Summary of contributions

This thesis contains the following main contributions:

- The design of a novel, high-fidelity vibrotactile interface in a rigid floor surface. The device was analyzed and structurally optimized to ensure a usable passband extending from about 50 to 750 Hz.
- The design of a distributed, touch-sensitive vibrotactile display, and techniques for using it to interact with multimodal simulations of natural ground terrains and touch surface interfaces.
- The demonstration of a new haptic perceptual-motor illusion, in which vibrotactile feedback was revealed to increase the perceived compliance of a rigid surface in a predictable manner.
- An analysis of pseudo-periodic stick-slip motion in a class of stochastic models of sliding friction. A novel first passage time problem was presented, whose solutions were demonstrated to capture the statistical properties of the motion. Noise-induced irregularities in stick-slip motion are characterized as stochastic resonance phenomena, a connection that is, to the best of our knowledge, established here for the first time.

- Time-domain methods for simulating fracture processes in stiff, heterogeneous materials. They are efficient enough to be used for the interactive rendering of vibrotactile and auditory feedback resulting from stress fluctuations in these materials.
- A demonstration of the feasibility of ambient information display with vibrotactile messages communicated through a floor surface, and usability guidelines for the design of such displays.

Chapter 2

Background

This chapter presents a general survey of prior literature pertinent to the research presented in this thesis. Due to the diverse range of topics addressed in different parts of this thesis, further review of specific background relevant to each component of this thesis is given in sections 3.1, 3.2, 4.1, 5.1, 5.2, 6.1, 7.1, and 8.1 of the chapters that follow.

2.1 Dynamics and forces in walking

Walking is a periodic activity, and a single period is known as the gait cycle. Typical human walking rates are between 75 and 125 steps per minute (about 1.25 to 2 Hz) [1]. It can be divided into two temporal phases – those of stance and swing (Fig. 2.1). The former comprises approximately 60 percent of the cycle, during which some part of the walker’s weight is carried by that foot, and can be characterized in terms of foot position and contact, decomposed into initial heel strike, followed by foot flat, heel off, knee flexion, and toe off. The subsequent swing phase spans the period from when the toe first clears the ground until ground contact is reestablished. Thus, the gait cycle is characterized by a mixture of postural attributes (e.g., the degree of flexion at the knee) and contact attributes (e.g., toe on or off). Several time scales are involved, including those of the walking tempo or pace, the footstep, encompassing an entire swing-stance cycle, and discrete events such as heel strike and toe slap.

The net force \mathbf{F} exerted by the foot against the ground is a vector with components tangential and normal to the ground surface. One can distinguish between low and high frequency force components, above and below about 50 Hz. The former is referred to as the

Ground Reaction Force (GRF), and is responsible for the center of mass movement of the individual and the support of his or her weight. Although approximately independent of footwear type, it varies between individuals and walking styles [2]. High-frequency forces are due to material-dependent transient, noise-like, or oscillatory interactions between the shoe and ground surface, and are responsible for airborne acoustic and mechanical vibrations generated during walking [3, 4, 5, 6, 7, 2]. Since these high-frequency signals depend energetically on walking movements that generated them, the gait frequency is readily detected in remote measurements via seismic and acoustic sensing [8, 7, 2, 9]. Signatures of individual footsteps are marked by the two key events: the heel strike and toe slap [3, 4] (Fig. 2.1). The time between the two is on the order of 100 ms for stereotypical walking. However, depending on the shoe type, activity, and ground surface shape, a more complex temporal dependence may be observed.

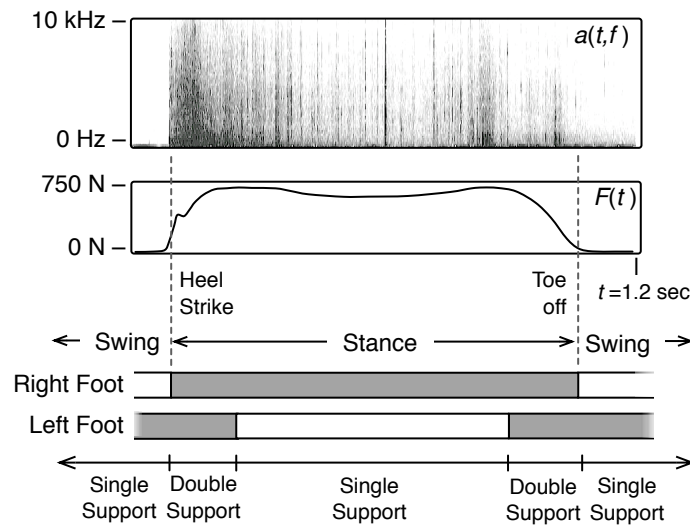


Fig. 2.1 Vibration spectrogram $a(t, f)$ and low-frequency normal foot-ground force $F(t)$ measured at the hard sole of a men's shoe during one footstep of a walker onto rock gravel, together with the corresponding foot contact states within the gait cycle (author's measurements). The dark vertical stripes in the spectrogram correspond to discrete impact or dislocation events that are characteristic of dynamic loading of a complex, granular medium.

2.2 Mechanical interactions and materials

Stepping onto a natural or man-made surface produces rich multimodal information, including mechanical vibrations that are indicative of the actions and types of materials involved. Stepping on solid floors in hard-soled shoes is typified by transient impacts due to initial heel strike with the floor surface and subsequent slap of the toe area, while sliding can produce either squeaking (when surfaces are clean) or textured noise. In indoor environments, the operation of common foot operated switches, used for lamps, dental equipment, or other machines, is often accompanied by transient contact events between solid mechanical elements.

The discrete quality of these mechanical signals can be contrasted with the more temporally extended nature of those generated by a step onto natural ground coverings, such as gravel, dry sand, or branches. Here, discrete impacts may not be as apparent, and can be accompanied by both viscoelastic deformation and complex transient, oscillatory, or noise-like vibrations generated through the inelastic displacement of heterogeneous materials [10]. A few of the processes that can be involved include brittle fracture and the production of in-solid acoustic bursts during rapid micro-fracture growth [10, 11, 12], stress fluctuations during shear sliding on granular media [13, 14, 15, 16], and the collapse of air pockets in soil or sand.

Thus, foot-ground interactions are commonly accompanied by mechanical vibrations with energy distributed over a broad range of frequencies. High-frequency vibrations originate with a few different categories of physical interaction, including impacts, fracture, and sliding friction. The physics involved is relatively well understood in restricted settings, such as those involving homogeneous solids, but less so when disordered, heterogeneous materials are involved. Due to the random nature of stress-strain fluctuations in these materials, statistical modeling approaches have seen considerable success in describing them [11, 10]. Chapters 7 and 8 of this thesis investigate stochastic models of fracture and friction associated with some of the aforementioned processes

2.3 Vibrotactile sensation and perception

The sense of touch in the human foot is highly evolved, and is physiologically highly similar to that in the hand, with the same types of tactile receptor populations as are present in

the former, including the fast-adapting (FA) type I and II and slow-adapting (SA) type I and II cutaneous mechanoreceptors [17, 18], in addition to proprioceptive receptors including Golgi organs, muscle spindles, and joint capsule receptors in the muscles, tendons, and joints. The sole is sensitive to vibrotactile stimuli over a broad range of frequencies, up to nearly 1000 Hz, with FA receptors comprising about 70% of the cutaneous population. Several differences between tactile sensation in the foot and hand have been found, including an enlargement and more even distribution of receptive fields in the foot, and higher physiological and psychophysical thresholds for vibrotactile stimuli [18, 19], possibly related to biomechanical differences between the skin of the hands and feet [20]. Further comparisons of the vibrotactile sensitivity of the hand and foot were performed by Morioka et al. [21].

It is almost a truism to say that self motion is the most fundamental function of walking, so it is not surprising that most of the scientific research in this area is related to the biomechanics of human locomotion, and to the systems and processes underlying motor behavior on foot, including the integration of multisensory information subserving planning and control. During locomotion, sensory input and muscular responses are coordinated by reflexes in the lower appendages [22, 23, 24], and prior literature has characterized the dependence of muscular responses on both stimulus properties and gait phase. The vibrotactile sense in the foot has been less studied in this regard, presumably because it is not a primary channel for acquiring information about low frequency forces and displacements that are most salient to the control of locomotion and balance.

Perceptual abilities of the foot are essential to the sensorimotor loop involved in the control of locomotion, but have been much less studied than those of the hand, to which it is serially homologous. Prior literature has emphasized perceptual-motor abilities related to the regulation of locomotion and balance on slippery, compliant, or slanted surfaces [25, 26, 27, 28, 29, 30, 31, 32]. The stepping foot is able to discriminate materials distinguished by elasticity [33, 34] or by raised tactile patterns [35, 36], as demonstrated in research aimed at evaluating the utility of these features for aiding visually impaired people in walking or navigating safely and effectively.

Although walking on natural ground surfaces generates rich haptic information [4, 2, 37], little research exists on the perception of such materials during locomotion. The author of this thesis collaborated on a prior study in which walkers were tasked with identifying synthetic and natural walking surfaces in different non-visual sensory conditions, while

wearing shoes [38]. Better than chance performance was observed in all conditions in which tactile information was unmodified. Performance was worse when tactile information was degraded by a vibrotactile masking signal supplied to the foot sole. Although the latter could have affected haptic information in multiple ways (by perturbing high- and low-frequency cutaneous tactile information and/or information from deeper joint and muscle proprioceptors) subsequent analyses indicated that this information was highly relevant for discriminating walking grounds. Furthermore, performance was not significantly improved when auditory information was provided in addition to tactile information, suggesting that similar high frequency information was communicated through both channels.

As mentioned, haptic perceptual abilities of the hand have, unlike those of the foot, been extensively studied in prior literature [39, 40, 41]. Vibrotactile information generated by manually tapping, scraping and scanning are salient to the perception of surface properties such as hardness, texture, or material composition [42, 43, 44, 45, 46, 47]. In the early 20th century, David Katz argued, in essence, that coarse textures are spatially coded, while fine textures are represented in the time domain [48]. The existence of spatial codes above a length scale of about 100 μm received support beginning with work by Lederman and others in the 1970s, while a complementary vibrotactile code for texture has been extensively described in more recent literature [49]. The vibrotactile sense is especially salient to the perception of fine surface textures, and to those felt through a rigid link. Available evidence suggests that the sensory information involved is preferentially acquired by FA II (Pacinian) receptors, which are sensitive to frequencies between about 40 and 1000 Hz [49]. A further indication that vibrations felt during surface scanning are involved in judgements about texture comes from the observation that imposing synthetic vibrations during manual surface scanning can increase perceived surface roughness [50].

2.4 Display and interaction techniques

In computing applications, the foot has been used to control interfaces for human-computer interaction and to enable navigation in immersive virtual environments, highlighting distinct functional uses of the lower appendage for touching objects near the floor, and supporting or moving the body.

2.4.1 Walking in virtual worlds

Walking is arguably the most intuitive way to navigate an environment. In most research on virtual environments, users are constrained to remain seated or to stand in place, which can have a negative impact on the sense of immersion [51]. Consequently, there has been much recent interest in enabling users of such environments to navigate by walking. One approach to this problem has resulted in the development of motorized interfaces that allow the use of normal walking movements to change position within a virtual world. Motorized treadmills have been extensively used to enable movement in one-dimension, and this paradigm has been extended to allow for omnidirectional locomotion through an array of treadmills revolving around a larger one [52]. Another configuration consists of a pair of robotic platforms beneath the feet that are controlled so as to provide support during virtual foot-ground contact, while keeping the user in place, while yet another consists of a spherical cage that rotates as a user walks inside of it [53]. The range of motion, forces, and speeds that are required to simulate omnidirectional motion make these devices intrinsically large, challenging to engineer, and costly to produce. In addition, while they are able to simulate the support and traction supplied by the ground, they cannot reproduce the feeling of walking on different materials.

Lower-cost methods for walking in virtual environments have been widely pursued in the VR research community. Passive sensing interfaces have been used to allow for the control of position via locomotion-like movements without force feedback [54]. Walking in place is another simple technique, in which movements of the body are sensed, and used to infer an intended movement trajectory [55]. For virtual environments that are experienced via an audiovisual head mounted display, a user's locomotion can be directly mapped to movements in a virtual environment. The real walkable workspace is typically much smaller than the virtual environment, and this has led to the development of techniques, such as redirected walking [56], that can engender the perceptual illusion that one is walking in a large virtual space.

The auditory and tactile experience of walking on virtual materials can be simulated by augmenting foot-ground interactions with appropriate sounds or vibrations. Although vibrotactile interfaces are simpler and lower in cost to implement than haptic force feedback devices [57], they have only recently been used in relation to walking in virtual environments. Auditory displays have been more widely investigated, and walking sounds are

commonly used to accompany first-person movements in immersive games, although they are rarely accompanied by real foot movements. Cook developed a floor interface (the Pholimat), for controlling synthesized walking sounds via the feet, inspired by foley practice in film [58, 59], and other researchers have experimented with acoustically augmented shoes [60]. Research on the use of vibrotactile displays for simulating virtual walking experiences via instrumented shoes [61] or floor surfaces [62] is still in its infancy.

2.4.2 The foot in human-computer interaction

Interactions via the feet have been explored in human-computer interaction for several decades, and prior to that, in various areas of human-machine interaction (e.g., for controlling sewing machines or surgical equipment). Game peripherals and computerized exercise equipment utilizing stepping movements were first popularized in the 1980s [63], while foot pedals for human-computer interaction were systematically studied shortly thereafter [64].

Manually operated (multi-) touch screens have achieved widespread commercial success, but touch-sensitive interfaces for the feet have received far less attention. Companies including Gesturetek and Reactrix (now defunct) have marketed interactive floor-based visual displays, in which foot locations are sensed via cameras. Such systems provide poor information about foot-ground contact, which limits their applicability for either functional floor-based interfaces or for simulating virtual foot-operated controls. Techniques for contact sensitive multi-touch interaction have been successfully adapted for use with the feet, although costs may be relatively high due to structural constraints [65]. Other systems have required users to wear instrumented shoes while interacting with a video projection on the floor, as in the Step WIM interface of LaViola et al. [66].

Although tactile displays do not seem to have been integrated in any of the aforementioned interfaces, several researchers have investigated the use of simple forms of tactile feedback for passive information conveyance to the feet. Actuated shoe soles used to provide tactile indicators related to meaningful computing events [67, 68], and rhythmic cues supplied to the feet via a stair climber have been found to be effective at maintaining a user's activity level when exercising. In automotive settings, tactile warning cues delivered via the accelerator pedal have been studied for many years [69], and eventually appeared in production vehicles. Tactile stimulation to the feet has also been explored as an additional feedback modality in computer music performance [70]. Further discussion is provided in

Chapter 3, which presents applications of a vibrotactile floor interface to ambient computing and human-computer interaction.

Floor- and shoe-based force sensing interfaces have been developed for applications in the movement and sports sciences, for gait and balance rehabilitation, the analysis of musical and dance performance, artistic and entertainment creation, architectural design, marketing, surveillance, virtual reality training, and transportation, among others. Tactile sensing solutions based on shoe- or floor-mounted arrays of force sensors are commercially available from companies like TekScan. Several distributed, force-sensing floors have been developed for interactive art and multimedia performance and surveillance, including the ASU-AME sensing floor, the GaitMat, Lightfoot, Magic Carpet, Z-Tiles, FootSee, Ada, and others [71, 72, 73, 74, 75, 76, 77]. A comparative overview is provided by Miranda and Wanderley [78]. A novel approach based on a sparse network of intrinsic force sensors in a distributed array of tiles is presented in Chapter 5 of this thesis.

2.5 Vibrotactile interfaces and physically based synthesis

A central topic to this thesis is vibrotactile interaction with virtual ground surfaces. Although simpler vibrotactile stimuli (e.g., status messages) were referred to in the foregoing, we reserve the term vibrotactile interface to describe devices that present mechanical vibrations (displacements or accelerations) interactively in response to user-generated forces or displacements, typically so as to simulate interaction with a virtual object. Examples of such interfaces include a handheld rod containing a virtual ball [79], and a graphics tablet through which virtual surface textures may be felt with a handheld stylus [80], in addition to the shoe- and floor-based devices mentioned in the preceding section.

2.5.1 Hardware

Although the vibrotactile sense is part of the haptic sensory system, there are at least two important differences between vibrotactile and force-feedback interfaces. First, the latter is used to render both static and dynamic forces over a macroscopic range of displacements. In meeting this goal, most haptic interfaces are compromised in their ability to accurately reproduce transient or other high frequency forces or displacements. A force-feedback interface has a usable frequency band from DC to an upper limit that is usually constrained by resonances or anti-resonances in the kinematic mechanism. For example, one device,

the Sensable Phantom 1.0A, was found to have a lowest structural resonance of 30 Hz [81], a value that excludes most of the vibrotactile frequency range from the usable passband of the device. A second difference is that a force-feedback display involves a closed control loop between displacement and force (impedance control), or force and displacement (admittance control), because the two are coupled at both the manipulandum and virtual object simulation. As a result, if care is not taken to ensure the energetic passivity of the haptic simulation, interactions with it can destabilize due to spurious energy created by the discrete-time realization of force-displacement relationships. In a vibrotactile interface this situation is not normally encountered, because the sensor and actuator signals can be specified to occupy non-overlapping frequency bands. Partly for this reason, most vibrotactile interfaces are operated in open loop control mode, and in this respect, and in their emphasis on the reproduction of transient or oscillatory signals, resemble audio displays.

Most consumer devices that integrate vibrotactile displays, such as mobile phones or game controllers, make use of inexpensive eccentric mass motors that cannot present vibrations with independently specified amplitude and frequency, hence are ill-suited for high fidelity vibrotactile display. Less restrictive actuators include inertial (voice coil) motors, DC motors, and piezoelectric actuators [82]. Inertial motors are able to present vibrations with a high dynamic range over a large bandwidth of frequencies, and are simple enough to be constructed by hand. They are based on an inertial slug driven by electromagnetic induction. The most common configuration consists of a magnet suspended elastically between the coils of an inductor, which is driven with an oscillating waveform, creating an axial Lorentz force. Vibrations are induced via conservation of momentum. By suitable specification of the magnet mass, suspension stiffness, and geometry, the acceleration frequency response can be designed to be approximately flat over a frequency range of interest [83]. When coupled to a manipulandum or other display components, the structural dynamics of the display must also be taken into account. Chapter 4 of this thesis presents the engineering design of a vibrotactile display integrated in a rigid floor plate.

Users can be enabled to interact with such a device in many ways – for example, by moving a handheld object, by pressing a surface, or exerting force against a manipulandum. Sensing can be accomplished via accelerometers, rotary position encoders, resistive or capacitive force sensors, or hall effect position sensors [82]. A simulation of a virtual object or material is then used in order to compute vibrations in response to the sensed movements or forces.

2.5.2 Physically based synthesis

A variety of techniques for synthesizing haptic forces or displacements during interaction with objects or surfaces in a virtual environment have been developed over the past 15 years [84], and many of them are also relevant for vibrotactile interfaces. The requirements of vibrotactile synthesis are, in addition, similar to those of sound synthesis, except that, in the former case, the usable frequency range extends to only 1000 Hz. Also, some aspects of sound perception, such as reverberation and spatial hearing, do not correspond to any tactile phenomena. Nonetheless, many techniques that have been developed for sound synthesis can be used for vibrotactile rendering [59, 85].

As noted in Section 2.2, walking in natural and man-made environments involves basic interactions, including viscoelastic deformation, solid friction, texture, and impacts, for which existing haptic rendering methods are applicable [84], and more complex processes, such as brittle fracture in heterogeneous solids and sliding on granular media, that lie beyond the state of the art. Two difficulties involved in the haptic rendering of such phenomena are the high sampling rates required for stable, artifact-free rendering, and the large number of degrees of freedom involved [84].

In computer graphics research, particle-based rendering methods have been used to animate granular media [86, 87, 88]. However, known algorithms are far too slow for haptic or vibrotactile interaction, and, due to the low frame rates and gross physical approximations entailed, they do not capture most of the spatial and temporal stress fluctuations that are observed in real granular materials. Similar remarks apply to computer graphics rendering methods for brittle fracture, which, despite recent advances, remain too costly for interactive haptic, vibrotactile, or audio rendering [89, 90, 91, 92, 93].

However, the disordered nature of these materials allows many aspects of their physics, such as disorder effects, acoustic emission, and stress fluctuations to be captured by more efficient, stochastic models that do not attempt to reproduce the full deterministic evolution of stress throughout the distributed medium [10, 11]. In haptic rendering, stochastic methods have been used to simulate random force components generated by sliding between rough, solid surfaces. Siira and Pai used the observation that height profiles of many solid surfaces are approximately Gaussian distributed to derive a simple time-domain stochastic texture rendering model [94]. The texture force was taken to be proportional to the surface height at the contact point, hence could be computed by sampling from a Gaussian

distribution at each time step. The resulting random force component was equivalent to additive Gaussian white noise, except in a small deadband around zero velocity. Green and Salisbury used a similar method to render haptic interactions based on measurements of sliding on sandpaper [95]. Fritz and Barner proposed extensions of this technique, including the use of filters or correlated noise to shape the distribution of frequency content in texture forces. They also applied it to rendering volumetric texture components associated with viscous forces (e.g., stirring a pool of ball bearings).

In the related field of sound synthesis, noise has also been used to represent random force components from frictional sliding [96] and scraping [97]. Cook developed efficient stochastic methods for synthesizing acoustic textures produced by systems composed of many loose particles, such as maracas [59]. The method assumes the texture is produced by a large number of discrete impacts occurring at different times, with different forces. The distribution of impact times is modeled as a Poisson process, where the time Δt between events is distributed according to a Poisson distribution $P(\Delta t) = \lambda \Delta t \exp(-\lambda \Delta t)$, where λ is the event rate. Heuristics are used to deduce a plausible relationship between $\lambda(t)$ and the forces $F(t)$ on the system, or the temporal evolution of other parameters [98]. Individual impacts may be rendered via playback of short, pre-recorded transients, or by a discrete-time simulation of shock impacts a Hertzian contact model, coupled to a resonant modal filter [99]. The drawback of these phenomenological methods is that their correspondence with the physics of any actual system is obscure. However, they have been used to synthesize a variety of different sound effects, including those produced by footsteps on different materials [59, 58].

Chapter 7 of this thesis develops an efficient temporal model of fracture in fiber composite materials based on a widely studied example from physics, while Chapter 8 analyzes stochastic models for irregular stick-slip oscillations associated with sliding on rough surfaces or granular media.

Chapter 3

Floor Surfaces as Ambient Haptic Interfaces

© 2009 IEEE Reprinted, with permission, from

Yon Visell, Alvin Law and Jeremy Cooperstock, “Touch is Everywhere: Floor Surfaces as Ambient Haptic Interfaces.” *IEEE Transactions on Haptics*, Volume 2, Number 3, pp. 148–159, 2009.

Copyright notice:

This material is posted here with permission of the IEEE. Such permission of the IEEE does not in any way imply IEEE endorsement of any of McGill University’s products or services. Internal or personal use of this material is permitted. However, permission to reprint/republish this material for advertising or promotional purposes or for creating new collective works for resale or redistribution must be obtained from the IEEE by writing to pubs-permissions@ieee.org.

By choosing to view this material, you agree to all provisions of the copyright laws protecting it.

Preface to Chapter 3:

This paper investigates the use of vibrotactile feedback presented via floor surfaces for ambient information display in intelligent environments. A number of potential applications are described, along with relevant design and engineering considerations. An encoding of vibrotactile communication messages by means of rhythmic sequences of virtual impacts is presented here for the first time, and is found to result in higher recognition performance than an encoding based on sequences of tone-like stimuli similar to those used in prior literature. The results support the feasibility of ambient vibrotactile information display through floor surfaces, and provide the first guidelines for the design of such interfaces.

Contributions of Authors:

Yon Visell designed the apparatus and display method, and designed, implemented and ran the experiments, and analyzed the data. He also produced the figures and wrote the manuscript. Alvin Law contributed to the design of the apparatus, implemented the apparatus, ran the experiments, and contributed to the data analysis. Prof. Cooperstock supervised the research and edited the manuscript.

Abstract Floor surfaces are notable for the diverse roles that they play in our negotiation of everyday environments. Haptic communication via floor surfaces could enhance or enable many computer supported activities that involve movement on foot. In this paper, we discuss potential applications of such interfaces in everyday environments, and present a haptically augmented floor component through which several interaction methods are being evaluated. We describe two approaches to the design of structured vibrotactile signals for this device. The first is centered on a musical phrase metaphor, as employed in prior work on tactile display. The second is based upon the synthesis of rhythmic patterns of virtual physical impact transients. We report on an experiment in which participants were able to identify communication units that were constructed from these signals and displayed via a floor interface at well above chance levels. The results support the feasibility of tactile information display via such interfaces, and provide further indications as to how to effectively design vibrotactile signals for them.

3.1 Introduction

Tactile feedback has received growing attention as a means of enhancing or enabling information display in diverse computing applications. As human computer interaction has extended beyond the desktop computing paradigm, and into every other domain of human activity, tactile display has grown in importance. This is attributable, in part, to its ability to overcome the sensory overload and attentional demands that arise in complex, multitasking environments.

Two new paradigms that have emerged within this context are those of mobile or wearable information appliances, and of ambient computing. While significant attention has been devoted to the opportunities for tactile display to enhance mobile applications, less has been given to haptic interaction with computationally augmented environments. Nonetheless, the fundamental role that floor surfaces play in our haptic negotiation of everyday environments suggests that they hold significant potential for active tactile information display.

The design of haptic information for ground surfaces has a long history, as is evidenced in urban environments. Haptic markers are commonly used to indicate locations or paths of interest to visually impaired people. Similarly, they are employed to emphasize low-lying features, such as subway stairs, that need to be highlighted even to sighted individuals.

Many everyday ground surfaces could also be profitably augmented with active tactile information displays. Such displays might find roles that are complementary to those that have been explored in the mobile computing domain. Some simple end-user scenarios may be helpful to guide the discussion:



Fig. 3.1 A possible end-user scenario: Pedestrians receive vibrotactile cues via the ground surface, indicating the location of the crossing and state of its signal.

- A visually impaired pedestrian is traveling to an appointment on foot and by public transportation. Reaching a noisy urban crosswalk, she is able to infer, via a vibrotactile cue received near the curb, that the crossing signal is red. Later she receives a cue indicating that it is safe to cross (Figure 3.1). She enters the subway and is able to feel, via haptic feedback supplied near the platform edge, that the train has not arrived. Once it arrives, similar cues indicate the locations of the train doors. She reaches the building of an office, and locates the elevator. While ascending to her destination, she receives a vibrotactile cue from the elevator floor, indicating the floor number that has been reached, and instantly knows when to disembark.
- An elderly person taking a shower in his home receives subtle vibrotactile feedback to his feet, unconsciously aiding him in maintaining his balance in response to sensed shifts in his center of mass and pressure.

- A rescue team is engaged in an augmented reality training simulation that aids them in learning to evaluate and respond to the changing conditions of a structure during an emergency. They receive realistic cues through the response of a haptically actuated floor delivering signals appropriate to the material and local stability of the ground surface in the simulation.

3.1.1 Potential Advantages

Floor-based haptic communication interfaces may share many positive features that are characteristic of other kinds of haptic communication:

- *Complementarity to other modalities:* Such displays can function well even when visual attention is occupied, or when the environment is noisy.
- *Attentional salience:* Tactile displays can be an effective means of directing attention to a significant event or location, in the presence of task load or sensory distraction.
- *Discreetness:* Information received through such a display need only be apparent to its user.

Haptic communication via floor interfaces may, in addition, offer some specific advantages, such as those of:

- *Ubiquity and unintrusiveness:* Reflecting the near universal presence of foot-floor contact in human environments.
- *Acceptibility:* While people may be averse to touching certain objects in public spaces such as restrooms, floor surfaces are broadly acceptable to touch, via the shoes.
- *Ready accessibility:* Floor-based interfaces need not require users to possess or wear any special technology, making them accessible to a wider range of users.
- *Lack of specific demands on visual or manual search:* An interface might be positioned at a location (such as a pedestrian crossing) in such a way that little visual or manual search is required to locate it. This can be an advantage for users with visual impairments.

- *Location, navigation, and event salience:* Such interfaces may be well suited to applications that involve pedestrian navigation, wayfinding, or location-based information display.
- *Locomotion-specific effects:* As noted below, a floor might be readily designed to actively enhance specific sensorimotor aspects of walking.

3.2 Background

While the literature on haptic interaction design for the feet is quite limited, much of what is known about haptic communication via other areas of the body may be readily extended to the case of interest. In addition, in large part through research conducted in the last two decades, more is now known about tactile sensation in the feet. This background knowledge can, by extension, inform the design of floor-based interfaces, and it also raises issues that are uniquely applicable to haptic communication design for floor surfaces.

3.2.1 Tactile sensation and psychophysics of the foot

The tactile sensory physiology and psychophysics of the foot have been the subject of considerable research, if to a lesser extent than in the case of the hand. The foot has, since the mid-20th century, been acknowledged as one of the most sensitive parts of the body to vibrotactile stimulation [100, 19]. The sensory physiology of the sole of the foot is similar to that of the glabrous skin of the hand, including the same types of tactile mechanoreceptors as are present in the latter [101], namely fast-adapting type I and II receptors (FA I, FA II) and slow-adapting type I and II receptors (SA I, SA II). Their nervous responses largely mirror those of receptors in the hand [18], although some differences in peripheral vibrotactile information coding have been identified (see, e.g., Ribot-Ciscar et al. [102]). With regard to the receptor spatial distribution, Kennedy and Inglis found those in glabrous skin of the foot sole to be relatively widely distributed, with (in contrast to the hand) little preferential accumulation in the toe areas [18]. Receptive fields were found to be larger than in the hand by a factor of about three. Physiological activation thresholds were determined to be higher on average – by a factor of approximately eight, in the case of FA II receptors [18]. This latter finding agrees with earlier observations of higher psychophysical thresholds to vibrotactile stimulation of the foot compared to the hand [19]. It has been suggested

that this is due, in part, to biomechanical differences between the skin of the hands and of the feet, and possibly to mechanoreceptor properties [20]. The ball and arch of the foot have been found to be the areas most sensitive to vibrotactile stimulation [103].

Sensitivity has also been assessed for populations of different ages, with elderly people demonstrating elevated thresholds for vibrotactile stimulation at FA II mediated frequencies [103] (i.e., those most often targeted by vibrotactile displays [104]). Thus, age is a significant factor in haptic interaction design for floor interfaces. As in other areas of haptic communication, such differences may be compensated by learning on the part of users, or by plasticity effects, whereby repeated exposure over time has been found to improve vibrotactile discrimination [105].

Distinctive functional characteristics of the foot relative to the hand include the reduced prehensile dexterity of the former (which is reflected in the kinds of activities in which it is involved), and the fact that static and dynamic forces on the feet during stance are higher and more sustained than those in the hand (i.e., on the order of 100 to 1000 Newtons in the former case). Thus, while the thresholds measured in the studies cited above were assessed as subjects were lying down or otherwise off their feet, when individuals are walking, those thresholds may be higher, due to adaptation effects resulting from the large forces involved [106]. As in the case of the hand, most of the receptor types of the foot are simultaneously active during normal motor activities, unlike the more segregated responses that are observed to accompany simpler cutaneous stimulation by static probes, vibrators, or electrodes [18, 101]. Ribot-Ciscar et al. observed that vibrotactile stimulation of the foot can lead to a transformation of physiological messages potentially leading to the overestimation of static forces through co-activation of SA I afferents [102]. As a result, the application of extrinsic vibrotactile stimulation can result in unintended behavioral modifications affecting posture and gait. Ribot-Ciscar et al., among others, have previously identified similar, manual sensorimotor impairments affecting workers exposed to high-amplitude vibrations [107]. Roll et al. have investigated various proprioceptive illusions that can be induced by vibrotactile stimulation [108].

Humans on foot are implicitly engaged in a sensorimotor task (e.g., quiet stance or normal walking). The cutaneous tactile channels addressed by the types of interface we describe here are active in the peripheral regulation of balance and locomotion through reflexes coordinating stimuli felt through the feet to muscles in the leg and foot (see, e.g., Tax et al. [22], Zehr et al. [23]). During locomotion, the coupling of motor reflexes to

cutaneous stimulation has been found to depend on both stimulus properties and on the instantaneous gait phase at the time of stimulation. Thus, if a display is meant to be accessed during locomotion, careful consideration is warranted of stimulus design and the timing of presentation. Such entanglements of tactile sensation in the feet and motor behavior suggest that constraints on the design of actuated floor displays are needed in order to avoid adverse effects on gait and stance. At the same time, certain applications might exploit such effects. For example, a person entering a dangerous area might stop more quickly if cued by a suitable vibrotactile warning signal from the floor.

Finally, there has been much recent interest in the observation that it is possible to enhance sensation in the feet, and thereby postural and gait control, by providing sub-threshold noise to the foot soles [109]. This effect is seen as significant for elderly populations, and for others with peripheral neuropathies. Sensory aids of this type could be implemented through the kinds of display described in this article, either as a central or complementary feature.

3.2.2 Prior research on interfaces for the feet

While there has been little research on the design of haptically actuated floor surfaces, much may be learned from past work in areas such as the passive haptic design of ground surfaces, tactile feedback in foot-based human computer interaction, and locomotion interfaces for virtual environments.

Haptic Design of Ground Surfaces

Public transit areas, such as urban sidewalks, pose special risks to pedestrians with visual impairments. This is partly due to the fact that they cannot make use of visual cues or signs that are the most common means of marking hazards (e.g., at intersections). Tactile ground surface indicators consist of regularly textured areas of ground, in the form of patterns of raised domes, bars, or other bumps, arranged on the sidewalk to mark significant paths or points of safety concern [34]. While international specifications for such markers remain to be established, they must be clearly identifiable, without being obtrusive. When higher than about 5 mm, they have been found to pose risks for stumbling or falling [36]. Alternative means of demarcating floor areas have been proposed to remedy this. Kobayashi et al. investigated the discrimination of floor areas by elasticity, in order to

determine the feasibility of using this type of material variation as a substitute for ground surface indicators [33]. An active vibrotactile cue supplied through the ground could provide another approach.

Haptic locomotion interfaces

One area of recent research has concerned the engineering of locomotion interfaces for virtual environments, as recently reviewed by Iwata [52] and Hollerbach [53]. However, this research has predominantly focused on the challenging problems of high-fidelity force-reflecting haptic interaction for omnidirectional virtual walking experiences. The display of vibrotactile information underfoot for the purpose of increasing immersion during locomotion in virtual environments has only recently begun to be addressed [110].

Tactile communication with the feet

Vibrotactile displays for presenting information-bearing stimuli to the soles of the feet have been little explored to date. Shoes for this purpose have, for example, been investigated for information conveyance via non-intrusive or hands-free interfaces [67, 68]. Rovers et al. found that users were able to identify several families of haptic icons, consisting of moving patterns on the foot sole presented through an array of small vibration motors in the sole of a shoe-like apparatus [67].

Despite the limited research that has addressed the feet, there is ample evidence that information can be transmitted via diverse body surfaces, devices, encodings, and under many different conditions; extensive reviews of related considerations from the literature in these areas are provided in [105, 104, 57]. Beginning in the 1960s, Geldard and others systematically studied the use of tactile displays for communicating symbolic information via different parts of the body. Later research on sensory substitution aimed at conveying information about shape, spatial configuration, or environmental conditions near a user of a distributed tactile display; Such displays were designed for body parts such as the tongue, forehead, thigh, or back [104]. Basic guidelines for stimulation by vibrotactile feedback are now being formulated [111]. Trends in recent research aim at uncovering central capacities for, and limitations on, tactile information processing [105], and at establishing a foundation for the design of large sets of structured vibrotactile messages, based on perceptual and usability criteria [57]. Although such guidelines necessarily depend on the display device,

application, and user community addressed, basic strategies have been successfully applied to many different interfaces and sensory modalities. We profit from prior research on musically-inspired tactile communication design in Section 3.3.7, below.

Human-machine and human-computer interfaces

There are many control interfaces for machine operation by foot (car accelerator pedals, dental equipment, sewing machines), and somewhat fewer for human computer interaction (foot controlled computer mice, sensing floors and shoes). Few of these have profited from active haptic feedback. Systems providing haptic warning cues via an automobile’s accelerator pedal have been researched for many years as means of improving driving safety [69], and implementations have now reached the market (e.g., Infiniti’s Distance Control Assist). Ferber et al. studied haptic communication during a human control task conducted on a haptically augmented stair climbing machine. They found some simple haptic cues supplied to the feet via an exercise machine to be effective at aiding participants in maintaining a target exercise level. The cues consisted of regularly spaced tapping sequences encouraging the person exercising to exert more effort when he or she slowed down [112]. Hayward and Rovin developed vibrotactile interfaces for furnishing additional feedback during computer music performance, including augmented floor tiles and in-shoe stimulators [70]. While they reported the feedback to be subjectively effective at conveying spatial and temporal information, no systematic evaluation was performed. We are not aware of any prior work on the design of vibrotactile information displays for pedestrians via the actuation of floor surfaces.

3.3 Ambient haptic floors: display design

Since ambient haptic floor displays have been only recently developed, the potential design space has been little explored to date. In this section, we highlight roles that such interfaces might profitably take on in future applications and discuss design issues, including prototyping methods. We present a prototype floor platform, and describe several design strategies we have implemented for it.

3.3.1 Roles for haptic communication

Although application requirements depend on factors that are difficult to anticipate outside of a case-based discussion, a number of possible roles for a haptic floor interface can be identified.

Location-based information display Due, in part, to the commonality of foot-ground contact, such a device may be suited to providing notifications about a current or future events associated with a location (e.g., the arrival of a bus at its stop), or of informing about an ongoing process.

Display of navigation-salient information Such a device could be highly suited to demarcating a location or region of interest to pedestrians (e.g., a crosswalk location, or an in-store promotion), a direction or directions of interest, or for indicating a pedestrian path or passage (e.g., the route to an nearby emergency exit).

Functional augmentation of features or devices In interactive settings, floors as interfaces may prove useful for supplementing the functionality of existing architectural features (e.g., steps, entrances, stairs, tactile ground surface indicators) or interfaces (e.g., foot switches, haptic locomotion interfaces, exercise machines [112]).

Creative, entertainment, or emotional communication They may also be used for diversion, comfort, entertainment or in the context of artistic creation, for example, by silently providing a common tempo to musical performers, or by communicating information to a computer music performer [70].

Sensorimotor aids Cutaneous tactile stimulation via the soles of the feet can be designed to improve locomotion during rehabilitation or normal activities [113, 114]. It could also be used to provoke reflexes meant to avert a pedestrian from stepping in the path of danger.

Virtual reality display Augmented floor surfaces can be used for simulating natural ground surface features (e.g., earth, sand, stone) for virtual reality or augmented reality simulations that involve movement on foot (see [62] and Section 3.3.5, below).

3.3.2 Physical interaction design considerations

Good design demands consideration of the device’s physical configuration and other factors affecting the interaction. Some relevant considerations include: Whether the interface is to be integrated with an existing feature or device (e.g., an area of tactile ground surface indicators), or if it is to constitute a new artifact, such as a custom-built floor platform; Whether the interaction is to be afforded to a single person or to a group; The required spatial resolution; The level of interactivity that is needed; The level of independence of stimulation to each foot. Such considerations can only be addressed in detail through a particular design.

3.3.3 Prototyping technologies and methods

Many of the technologies needed for prototyping vibrotactile floor displays are readily available and require comparatively little engineering to deploy. The necessary electronic components consist of vibrotactile transducers, amplifiers, and signal generation circuitry (typically some form of computer with associated digital to analog converter).

Among the distinguishing technical requirements are the relatively higher power demands, owing to both the elevated vibrotactile sensory thresholds in the feet relative to those in the hand, and to the requirement of actuating a floor surface bearing a large mass.

Among other commercially available actuation technologies, one suitable choice is the linear voice coil motor. It consists of a metallic mass suspended on an elastic structure between the coils of an electromagnet, which, when driven, exerts a force directly against a structure to which it is attached (see the recent review article [82] for a discussion). An advantage of these actuators is that they provide independent control over amplitude and frequency, which is not the case for simpler devices, such as the eccentric mass motors commonly used in mobile phones. A second advantage is that the entire actuator may be concealed within the device. Several commercially available voice coil actuators exist that may be suitable for prototyping floor surface applications such as those described here.¹ The main technical requirements are that they possess a usable frequency bandwidth overlapping the domain of sensitivity of FA II receptors in the feet and are capable of supplying sufficient power to actuate the surface. Such actuators can readily be driven

¹Examples include the IBEAM VT200 (Sonic Immersion LLC, Hürth, Germany) and the TST239 (Clark Synthesis, Inc., Littleton, CO, USA).

with normal audio amplifiers.

Some technical simplifications are made possible by presenting vibrotactile stimuli via a rigid, actuated floor surface. First, this approach facilitates the protection of all electronic components beneath the surface of the floor (see Section 3.3.4). Second, the size of the surface being actuated means that if it is driven at frequencies extending into the audible band, usable auditory feedback can be supplied through the same interface, allowing for cross-modal information display. Since vibrations above about 1000 Hz are not felt, higher frequency signal components may, in part, be shaped so as to improve the accompanying auditory feedback. While we have found this feedback usable in practice, there are significant limitations arising from structural resonances and emission characteristics of the foot-floor system.

In some cases, a stimulus may be supplied through the floor in a way that is conditional upon, or computed as a function of, forces supplied by a pedestrian stepping onto that area of the floor. For example, a floor surface may be configured to provide a response resembling a (virtual) foot switch, controlled by foot pressure. Interactivity may be enabled via an array of force sensors embedded in the floor. A detailed discussion is omitted here. One example is described below.

We would like to address a few concerns that may arise in the mind of the reader regarding such interactions. First, despite the coupling between actuator and sensor, the forces supplied by the former are often negligible, because the magnitudes involved (on the order of a few Newtons or less) are much smaller than the low-frequency forces exerted by pedestrians against the ground (i.e., as large as 1000 Newtons). Second, although actuator size or other constraints may dictate a coarse spatial arrangement of actuators (distributed with a spacing of one or several feet in distance) this need not necessarily be apparent to a user. A stimulus is generally felt through each area of the foot in proportion to the force it to the vibrating surface. Thus, even though the spatial density of actuators may be very coarse, the resulting experience is that the stimulus originates at the locus of foot-floor contact. The effect is similar to that used to present virtual tactile buttons on touchscreen displays. For similar reasons, boundaries between individual tiles are less noticeable than might be expected, provided similar responses are supplied by adjacent tiles.

3.3.4 Prototype vibrotactile device

The device used in our work has evolved through of a series of earlier prototypes [62]. to pedestrians standing or walking upon it. It is assumed that they are wearing their accustomed footwear, and no special equipment is required to be worn. In addition to the actuators, force sensing capabilities have been integrated to enable interactivity, along the lines described above. We have previously used this interface to interactively synthesize vibrotactile signatures similar to those that would normally be generated by walking on natural materials, such as snow or gravel [62].

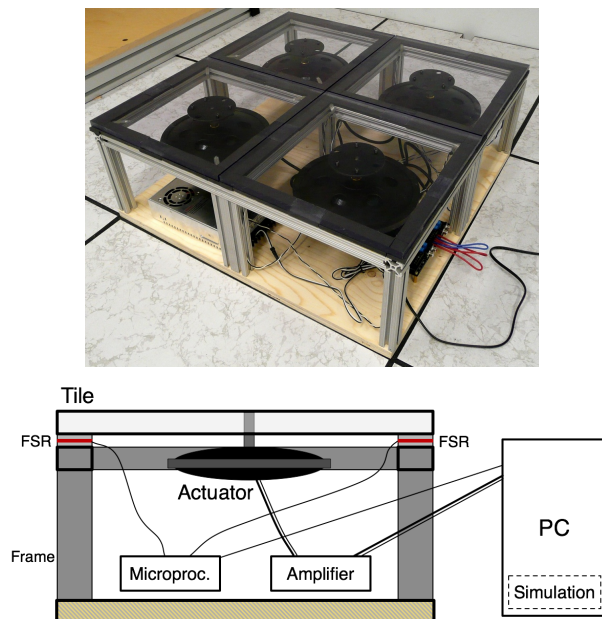


Fig. 3.2 *Top:* Interactive, four-tile prototype described in the text. *Bottom:* Diagram of same, with PC and rendering software.

The device is simple and robust in construction. A prototype is shown in Figure 3.2. The four tiles are rigid polycarbonate, of dimensions $30.5 \times 30.5 \times 1.25$ cm. They rest on an aluminum substructure. A force sensing resistor (Interlink model 403) encased in foam rubber 0.5 cm thick is positioned under each of the four corners of each tile (Figure 3.3).

A vibrotactile actuator is rigidly attached to the underside of each tile via a steel mounting bracket. In applications that are interactive, data from the force sensors is digitized and transmitted via a serial USB link to a personal computer that interactively generates the vibrotactile signals. The actuators are inertial voice coil motors (Clark Synthesis model

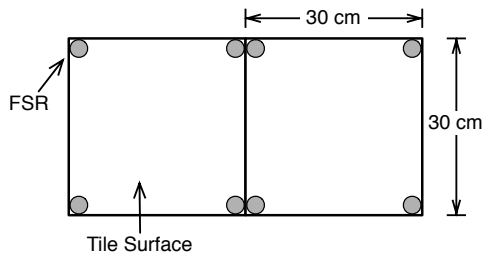


Fig. 3.3 A 2×2 tile prototype seen from above. Force sensing resistors are positioned as shown.

TST-239). They are capable of driving the floor surface with a greater power (by a factor of about four) than is required for the tiles used here. However, they are also used to prototype applications in which much larger tile surfaces are driven.

3.3.5 Temporal interaction design considerations

A floor-based haptic communication display, such as that described above, can also be characterized in terms of temporal properties of the stimuli involved, and the user interactions, if any, that generate them. Conceptually, one can group these qualities into those describing short-time properties of the vibrotactile signals being displayed, the manner in which they are patterned on longer time scales, and the type of interactivity afforded by the display and application.

For the purpose of this article, *short time* features are those related to time scales (smaller than about 200 ms) over which the stimulus may be thought to be relatively stationary or unitary. Such signals can be thought of as building blocks from which more complex stimuli can be built. They may be characterized by properties related to their frequency content, temporal extent, temporal amplitude envelope, or modulation that is applied to any of these. Alternatively, they might, as discussed below, be designed by analogy to a physical event, such as an impact transient, with properties resembling hardness or resonance.

Low-level signals can be profitably organized into structured *temporal patterns*. A motivation for doing so is to improve identifiability or to increase perceptual information content in a set of stimuli. The frequency bandwidth and temporal resolution of the tactile channel limit the amount of information that can be encoded via short-time features. In recent research on vibrotactile communication, musically inspired structures (motifs or rhythms)

have been profitably used to design larger sets of vibrotactile icons that are perceptually well distinguished from each other [115, 116, 117, 57]. An alternative approach, discussed further below, is to arrange low level signals to resemble the temporal pattern of a physical process, such as bouncing or breaking (for an example from an auditory perspective, see [118]).

Finally, properties related to the *interaction* itself refer to the manner in which vibrotactile signals are generated in response to user actions, as captured through sensors of the device. Here, one can also allow for the possibility that the device is non-interactive. Properties of the interaction are determined by the sensing method used, and the way in which the resulting data is used to control the synthesis of the vibrotactile signal. According to the nature of this control mapping, the interaction may be characterized as *discrete* or *continuous*. A continuous interaction gesture can be described as *effective* (in the gestural typology suggested by Cadoz [119]) if the vibrotactile signal is generated in a way that energetically increases with the energy of users' actions. A related notion is that stimuli may be synthesized as if generated by a virtual physical system, such as a bed of gravel, which is meant to be stepped upon.

3.3.6 Three interaction cases

To illustrate these design considerations, we present three different interaction case examples (Figure 3.4) developed for the interface described in Section 3.3.4:

1. A floor surface displays structured vibrotactile signals composed of abstract elements (such as a sum of sinusoids with a certain temporal envelope) resembling musical notes, and arranged in a rhythmic pattern (i.e., a *tacton*).
2. Such a surface presents stimuli that resemble the vibrational signature resulting from a physical object, such as a hammer, tapping with a rhythmic pattern on the underside of the tile. These representationally coded signals may be thought of as *tactile icons*.
3. A tile surface responds to the applied force exerted by a footstep with a signature approximating that of a natural ground material, such as gravel or snow. A computer simulation is responsible for rendering this feedback in a way that is highly dependent upon the measured force profile with which the step is executed in time [62].

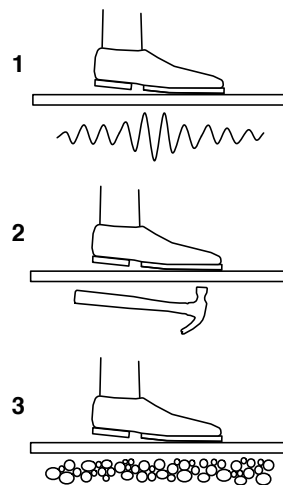


Fig. 3.4 Pictorial representations of three interaction paradigms. **1.** A vibrotactile message designed using waveform level properties (i.e., a *tacton*). **2.** One derived from a model of a physical process, such as an object tapping on the tile. **3.** A virtual physical material interaction, such as a step onto a bed of gravel.

Case 3 has been explored in an earlier publication by the authors [62]. Methods for the design of stimuli for cases 1 and 2 are described in detail in Section 3.3.7. They are evaluated in the experiments described in Section 3.4.

3.3.7 Vibrotactile stimulus design

Methods for the the presentation of structured vibrotactile stimuli corresponding to case examples 2 and 3 of Section 3.3.6 were prototyped. The approach is based in part on a musical phrase metaphor that has been evaluated positively in recent literature on vibrotactile display [117, 115, 116]. In it, a stimulus is encoded in a rhythmic phrase, characterized by a set of notes each having a certain onset time, duration, and amplitude. A phrase is constrained to consist of two or more repetitions of a musical bar. The time domain of a single bar is quantized into 24 unit steps. A tempo is set, determining the total duration of a bar (in seconds). Notes can begin at any step and possess durations given by integer numbers of steps. Only a single note is allowed to play at any time. The amplitude of each is specified at its onset. Notes within the pattern of a given vibrotactile signal differ only in their amplitudes and durations, so that all possess the same short time parameters (e.g., frequency and roughness). This limits the number of parameters that must be specified for

each stimulus. The algorithms used to synthesize the note-level signals are described in the sections that follow.

The vibrotactile signals used in the experiment described in Section 3.4 were built from a set of eight rhythmic patterns generated using this method. The corresponding bars are shown in Figure 3.5. The duration of each bar is between 450 and 750 ms, and each is repeated a fixed number of times (either 3 or 4). As shown in the figure, an accented note marks the beginning of each bar, serving as an “anchor” for the pattern [117]. The waveform of a stimulus from the experimental set, corresponding to rhythm R1 from Figure 3.5, is shown in Figure 3.7.

Waveshaping synthesis

The first approach we adopted to the design of short-time stimuli is based on the specification of basic signal properties affecting the frequency content, duration, amplitude

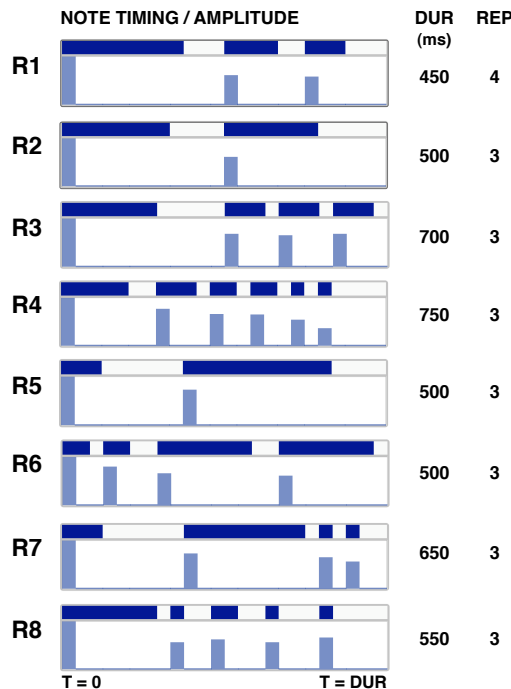


Fig. 3.5 The eight rhythms (R1 to R8) from which both sets of stimuli were built. Time runs left to right. The bold horizontal lines show the temporal extent of notes. The vertical bars coincident with the onsets indicate amplitude. Bar duration and number of repetitions are shown.

modulation, and amplitude temporal envelope of the signal, as prescribed in case example 1 of Section 3.3.6.

A basic harmonic signal $s(t)$ is composed of a sum of a fundamental sinusoidal component $s_0(t) = \sin(\omega_0 t)$ at angular frequency ω_0 , and N harmonic components at frequencies $\omega_k = k\omega_0$. The desired waveform can be efficiently generated by a standard technique from audio synthesis, known as Chebychev waveshaping [120]. In it, $s_0(t)$ is passed through a static nonlinear transfer function $w(x) = \sum_k a_k T_k(x)$, where a_k are the desired harmonic amplitudes, and $T_k(x)$ is the k th Chebychev polynomial. The result gives the desired harmonic signal $s(t)$ as

$$s(t) = w(s_0(t)) = \sum_k a_k T_k(s_0(t)) \quad (3.1)$$

$$= \sum_{k=0}^{N-1} a_k \sin(\omega_k t). \quad (3.2)$$

Using this method it is simple to design a waveform whose energy lies within the target frequency band, centered on approximately 250 Hz.

The complete short-time waveform $y(t)$ is obtained by multiplying the harmonic waveform $s(t)$ by an amplitude envelope function $e(t)$ with desired starting time t_s , duration T , amplitude A , attack and decay times t_a and t_d . Finally, it is subjected to form of roughening, via amplitude modulation with a signal $r(t) = 1 + m_r \sin(2\pi f_r t)$ of frequency f_r and modulation depth m_r . That is, $y(t) = s(t) e(t) r(t)$.

To generate the stimuli used in the experiment (Section 3.4), $N = 10$ harmonics were used, with fundamental frequency f_0 between 30 and 70 Hz, and a modulation frequency of $f_r = 25$ Hz. The harmonic amplitudes a_k , the roughness m_r , were set heuristically by the designer, as was the base frequency f_0 . Waveforms used in the experiments are shown in the top row of Figure 3.6.

Synthesis of virtual impact transients

The second method used to synthesize short-time stimulus components is based on virtual impact events, consisting of transient forces generated by the collision of two virtual elements: an exciting, but non-resonant object, termed the hammer, and a resonant object, termed the sounding object [121]. The impact force $F(t)$ is generated by an efficient, phys-

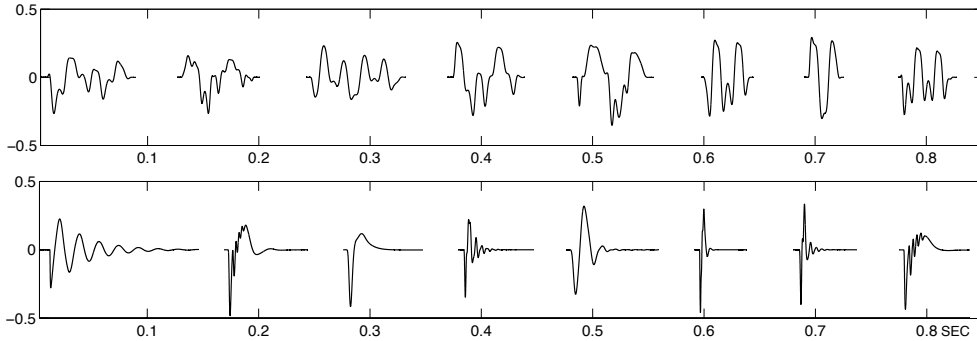


Fig. 3.6 Waveforms used to generate stimuli used in the evaluation, ordered as reported on in the experiment. *Top*: Those generated using waveshaping synthesis. *Bottom*: Those are generated using virtual impact transient model. The final stimulus sets result upon superimposing the rhythmic patterns described in Section 3.3.7.

ically based synthesis model obtained from a simplified version of Hertz' law, known as the Hunt-Crossley model [122]. It is obtained by numerically integrating the differential equation

$$F(t) = kx(t)^\alpha - \lambda x(t)^\alpha \dot{x}(t). \quad (3.3)$$

Here, $x(t)$ is the compression displacement and $\dot{x}(t)$ is the compression velocity. The impact force has parameters governing stiffness k , dissipation λ , and contact shape α . This force is provided as an input to the resonant sounding object. The latter is modeled as a set of N resonant filters operating in parallel, with a combined impulse response given by

$$y(t) = \sum_{i=1}^N a_i e^{-b_i t} \sin(\omega_i t), \quad (3.4)$$

and determined by a set of parameters governing the modal amplitudes a_i , decay rates b_i , and resonant angular frequencies ω_i . An impact event is synthesized by initializing Equation (3.3) with the desired velocity v_I of impact and subsequently integrating the composite system in time. See [121] for a more detailed discussion, including an overview of the numerical implementation we have used, which is based on the open source Sound Design Toolkit from the University of Verona.

The impact event transients used in the evaluation part of this paper were synthesized with two resonant modes ($N = 2$). The transients themselves exhibit more complex fre-

quency spectra than this might suggest, due to dynamic coupling of the nonlinear impact model with the modal resonant object [121]. Exemplary waveforms synthesized for the evaluation using this method are shown in the bottom of Figure 3.6.

3.4 Evaluation

An evaluation of the methods for vibrotactile information display via floor surfaces that were described above has been conducted. The aim was to determine whether vibrotactile signals designed in the two ways described could be distinguished when presented via a floor surface. Two sets of eight signals were designed, one based on the waveshaping method and the other based on the virtual impact transient method. (We refer to these as sets WS and IT respectively.) Both sets were designed using the same eight underlying rhythmic patterns (shown in Figure 3.5) as noted in Section 3.3.7.

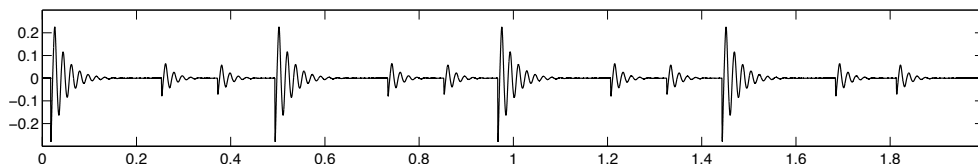


Fig. 3.7 Example of a stimulus used in the experiment, resulting from the model settings that produced the first “impact” waveform of Figure 3.6 in combination with the first rhythmic pattern of Figure 3.5.

The vibrotactile stimulus sets differed, therefore, only in the note-level signals from which they were composed. Each tacton from the waveshaping synthesis set (WS) was assigned distinct values of the fundamental frequency f_0 , ten harmonic amplitudes a_k , and amplitude modulation depth m_r . Stimuli from the impact transient (IT) set were each designed with different values of the hardness k , contact shape α , and of the frequencies ω_i and decay factors b_i of the two modes. The latter were chosen so that the frequency spectrum of the stimulus had most of its energy near 250 Hz.

Another significant difference between the two sets of stimuli is that the notes from the waveshaping synthesis (WS) set differ in duration according to the length of the note in the bar, while in the impact transient (IT) set, the amplitude envelope of each note decays exponentially as determined by the modal decay factors b_i . However, because the relevant decay times were generally short, as can be seen in row 2 of Figure 3.6, the durations were

shorter, in nearly all cases, than in the WS set, and they were independent of the note duration specified in the rhythmic pattern.

The experiment assessed both the rate of correct identification and learning for the two sets. In descriptive comments received during pre-testing, we observed a tendency for people to describe the the IT stimulus set in terms of familiar impact events. As a result, we hypothesized that these stimuli might prove more recognizable, despite the smaller number of parameters that were used to distinguish them, and the relative lack of note duration information in the patterns.

3.4.1 Methodology

A total of 24 people aged between 20 and 39 years took part in the experiment. All gave their informed consent in agreement with university ethics guidelines. Twelve of them were male and twelve were female. 14 of them were university students. The experiment was designed with a single independent factor, resulting in each group of twelve participants being presented with the task of identifying stimuli from one set. A between groups design was used because the rhythmic content in the two stimulus sets is identical, so participants exposed to one set would be expected to perform better than otherwise expected with the second set.

Each participant was given a pair of hard soled men's dress shoes in his or her size to wear during the experiment. Apart from size differences all the shoes were identical. The amplitude of vibration of the tile was adjusted as needed for each participant, depending on his or her ability to detect a reference vibrotactile noise signal. At the beginning of the session, participants received instructions, together with an explanation and demonstration of the experimental interface and the operation of the display. At all subsequent stages (except during pauses) participants were required to stand on the actuated floor surface, and to wear closed-ear headphones playing pink noise at a loudness sufficient to mask the (generally low-level) sounds produced by the apparatus. The software application used during the experiment ran on a personal computer, implementing the respective design method from Section 3.3.7. In addition to the floor tile, the interface consisted of a graphical user interface with numbered buttons, one for each icon, presented on a computer monitor. Participants selected items in the graphical user interface using a mouse.

The experiment was based on absolute identification of the 8 stimuli from the respective

set, with a unique correct response required for each (the numerical identifier of the icon, ranging from 1 to 8). The same stimuli were used for all participants within a given group, but they were presented in random order in each session of the experiment, with a different ordering presented to each participant.

After an introduction to the device and interaction method, participants were given five minutes of self-guided learning. During this time, they could select a numerical identifier and be presented with the stimulus corresponding to their selection. The rest of the experiment was divided into six sessions. During each session, all stimuli were presented twice. Thus, overall, each participant was asked to identify every vibrotactile stimulus from their set a total of twelve times. Each session took less than about four minutes to be completed. Participants were allowed a short break between sessions, but in most cases preferred to continue so as to avoid forgetting the learned associations. Participants were presented with stimuli sequentially. At each presentation, they could press a button to play the stimulus up to four times before supplying a response. Feedback, in the form of the correct stimulus ID, was provided after each response was given. As in previous studies [123], the reason for providing feedback was to facilitate the assessment of recognition after learning and rate of learning throughout the experiment.

3.4.2 Results and Discussion

A log of the stimuli and responses was recorded by the application throughout the experiments. Participants were also interviewed following the experiment.

The stimulus sets each included eight items, near the limit of what participants might be expected to retain in working memory. Training was limited, consisting of a maximum of, on average, 20 reinforced presentations of each stimulus at the end of the final session. The stimuli were not assigned any mnemonic, other than an arbitrary numerical index, that could be used to remember them. Although introducing a semantic association to each stimulus (for example, the name of a meaningful event) can be used to improve recall, good design of display and stimuli is a prerequisite to good performance [117]. Since our intention was to assess the suitability of the display methods behind these two stimulus sets, we wished to avoid introducing any external effects that might be associated to the choice of semantic labels.

The mean rate of correct identification after six sessions of enforced learning, averaged

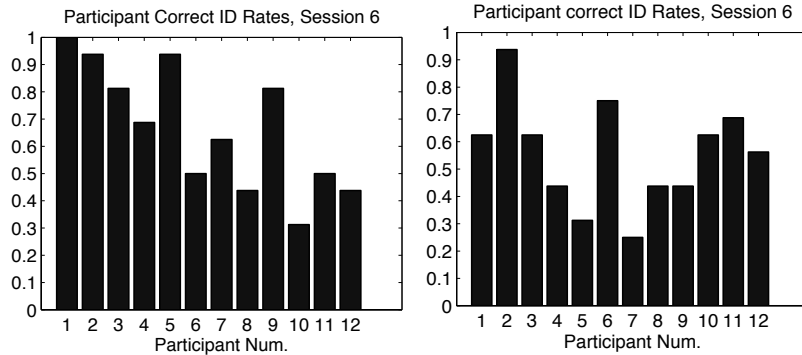


Fig. 3.8 *Top*: Correct identification rate for each of the twelve participants in group assigned to stimulus set IT, after 6 sessions of assessment with enforced learning. *Bottom*: Similar rates for the WS set group.

between all participants (including both stimulus sets) was 61%, with a standard deviation of 21%. Chance performance would correspond to 12.5%. Post-learning identification rates for participants in the impact transient (IT) group and for those in the waveshaping synthesis (WS) group are shown in Figure 3.8. Four of the twelve participants in the IT group were able to achieve 80% or better correct identification after less than 20 minutes of enforced learning. One of the twelve participants in the WS group was able to reach this level of performance.

The results obtained appear to be comparable to published results on absolute identification of vibrotactile stimuli via manual interfaces after short periods of learning. For example, Enriquez et al. reported average identification performance of 73% (vs. the expected chance performance rate of 33%) after an average of 20 minutes of learning [124].

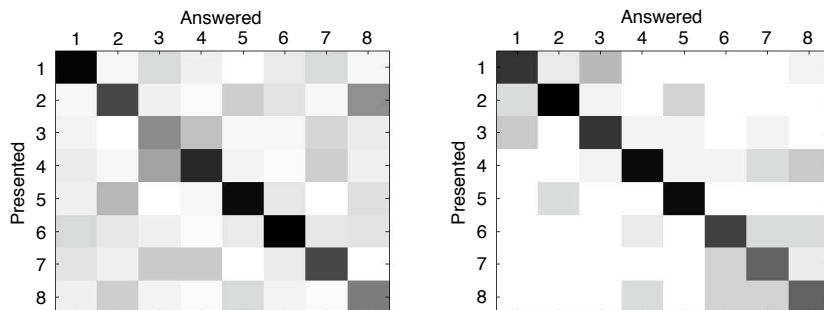


Fig. 3.9 *Top*: Confusion pattern within the set of eight WS stimuli in session 6, averaged between participants. *Bottom*: The same data for the set of eight IT stimuli.

The confusion patterns for the stimuli in each group of the experiment are shown in Figure 3.9, averaged between all sessions and participants. The least confused stimulus was identified at an average rate of 80%, while the most confused stimulus was identified at an average rate of only 25%. A close comparison of the confusions within each stimulus set with the stimulus properties themselves did not reveal any easily discernible feature of the rhythms or the short-time waveforms that caused them to be confused. Nonetheless, the confusion patterns for the two sets appear to be relatively distinguished from one another, which suggests that the short time features were perceived differently. Performance varied considerably between participants as the experiment proceeded, with a few showing consistently high improvement between sessions, while others showed nearly none. A summary of the mean correct identification rate using each icon set, averaged between all sessions, is provided in Figure 3.11. Mean performance on the impact transient (IT) set was higher than on the waveshaping synthesis (WS) set, but the level of significance is marginal (ANOVA 1-way $p=0.06$). Mean correct identification rates in each enforced learning session are shown in Figure 3.10. The mean correct identification rate after each of the first two training sessions was significantly higher for the IT set ($p=0.01$ and 0.02 respectively), but thereafter, the results lacked significance ($p > 0.1$ in all cases).

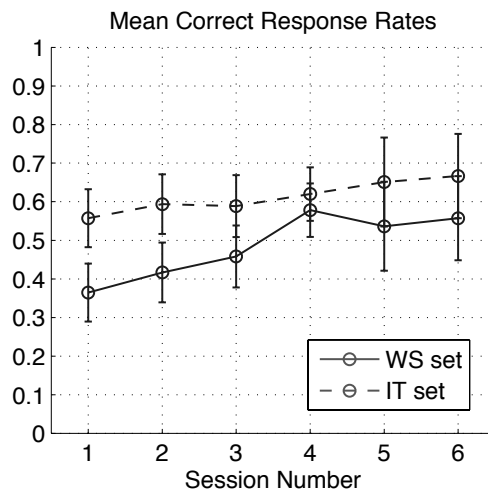


Fig. 3.10 Mean correct identification rates in each session. The error bars show 95% confidence intervals.

The IT group approached its peak performance with far fewer presentations of the stimuli than was the case for the WS group. Concretely, after session 1, the IT group

achieved more than 80% of the performance it reached in session 6, a rate that the WS group would not achieve until session 3. This suggests that stimuli similar to the IT set might be advantageous for applications in which little training would be expected, although further investigation of this is needed. Examples of such applications could include displays in public spaces, such as crosswalk indicators.

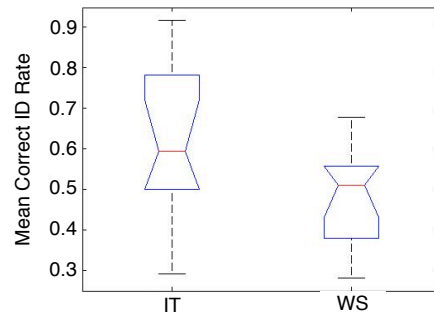


Fig. 3.11 Box plot summary of the mean correct identification rate for the IT (left side) and WS (right side) stimulus sets.

Subjective ratings and comments

Participants completed questionnaires after the experiment, rating the task difficulty, subjective properties of the stimuli, providing descriptive feedback regarding the strategies they adopted. Participants were asked to rate the difficulty of the first task session and the last session on a scale from 1 (very easy) to 5 (very hard). As expected, the first task session was rated as significantly harder than the last session (mean 3.96 vs. 3.04, with $p=0.04$).

An analysis of the rated difficulty of the first session (ANOVA 1-way), with the stimulus set type as the independent factor, revealed the WS set was perceived as initially harder than the IT set (mean 4.4 vs. 3.5, with $p=0.02$). However, there were no statistically significant differences between the rated difficulties of the stimulus sets during the last session. This echoes what was seen in the performance data: the IT stimulus set was more identifiable than the WS set at the beginning of the experiment, but the difference faded before the end of the experiment. Based on participant comments, cognitive fatigue may have been a factor here.

The study also aimed to assess the level of comfort to users of a vibrotactile display employing these stimuli. Participants were asked to rate the vibrotactile stimuli on a five point scale from 5 (comfortable) to 1 (uncomfortable). The average rating among all participants was 3.5 with a standard deviation of 1.1. No participants rated the stimuli as uncomfortable, and no significant differences in comfort ratings were found between the two groups. Some of them noted becoming uncomfortable with standing in the same place and posture during each session.

During subsequent interviews, several participants reported that the association part of the task, which required them to learn the numerical indices of the stimuli, was the hardest part of the experiment, and that they experienced cognitive fatigue as the experiment wore on. Some participants suggested the task may have been facilitated by the addition of semantic information, or a non-numerical mnemonic symbol (e.g., an animal name). As discussed above, this observation may hold potential for aiding the association part of the task, and, while it would certainly make sense for an application designer to consider, it does not necessarily speak to the design of the stimuli themselves.

Description of the cause of the stimulus

In a separate study, ten people who did not participate in the forgoing experiment were presented with the 16 stimuli from the sets used above, in random sequential order, and were asked to provide, using their own words, a short label describing what caused the vibration. Sensory conditions were the same as in the first experiment. The most common response was “unknown” (about 18% of IT set labels, and 40% of WS set labels). 113 other responses were obtained, 72 of which were unique, if often very similar (e.g., “door knock” and “angry door knock”). Among these labels, most were related to familiar impact events, including: “door knock”, “horse gallop”, “hammer”, “drum”, “foot falls overhead”, and “tapping”. To give one example, the second IT stimulus was described by seven of ten participants as a caused by a “knock” or “knocking”, and by another two as originating from a “hammer”. There appeared to be a greater tendency for IT set stimuli to be attributed to such events than was the case for WS set stimuli (mean 58% vs. 18%, with $p = 0.0002$). Here, however, we used our own judgement in deciding whether a label referred to an impact. Several labels were associated only to the WS set, including: “bass guitar”, “cellphone”, “machinery”, and “car start”.

While it seems likely that there are differences in causal interpretation between the two groups of stimuli, more research is clearly needed. It is tempting to suggest that such differences, if established, might be linked to the effectiveness of the stimuli at communicating information. However, analogous research in the auditory display domain, comparing the effectiveness of melodically designed “earcons” with representational “auditory icons”, has shown that this issue is far from simple or straightforward [125].

3.5 Conclusion

Floor surfaces already play roles that intimately link tactile sensation in the feet to our everyday activities. The use of such surfaces as displays for active haptic communication appears to be a valuable idea, and one that naturally extends accepted areas of practice in the design of haptic information for ground surfaces. We have highlighted the range of roles that such an interface might play in future applications, and have pointed to a few potential end user applications that illustrate these roles.

Distinguishing advantages of these displays include their applicability to a wide range of settings and environments, their ready accessibility to anyone on foot, and their potential for seamlessly presenting dynamic information linked to a specific location, navigational or locomotor task.

We have outlined design considerations for haptic communication through floor surfaces, and detailed a device and set of interaction studies that have been developed to embody these. The technological feasibility of such devices is high, and the cost of prototyping them is low.

A characterization in terms of temporal interaction properties was used to organize different possible interaction designs presented through the floor interface, and three demonstrations we have developed were described and situated within it. Stimulus design methods based on signal-level specifications were highlighted, by close analogy to prior work on vibrotactile information display. Design methods based on physical metaphors, such as virtual impact events or structured materials were also presented.

The experimental results support the identifiability of vibrotactile messages conveyed through floor surfaces, and point toward the adaptation of design guidelines developed for other modes of haptic display to this setting. They also suggest that physical metaphors may hold promise for improving the design of stimuli for such an information display,

although further research is needed on this subject.

Chapter 4

Vibrotactile Display Design

© 2010 IEEE Reprinted, with permission, from

Yon Visell and Jeremy Cooperstock, “Design of a Vibrotactile Display via a Rigid Surface.” *Proc. of the IEEE Haptics Symposium*, 2010, pp. 133–140.

Copyright notice:

This material is reproduced here with permission of the IEEE. Such permission of the IEEE does not in any way imply IEEE endorsement of any of McGill University’s products or services. Internal or personal use of this material is permitted. However, permission to reprint/republish this material for advertising or promotional purposes or for creating new collective works for resale or redistribution must be obtained from the IEEE by writing to pubs-permissions@ieee.org.

By choosing to view this material, you agree to all provisions of the copyright laws protecting it.

Preface to Chapter 4:

This paper presents an analysis and redesign of the vibrotactile floor interface that was described in the preceding chapter. The structural dynamics of the device was greatly improved at little added cost, and digital equalization is used to enable the display of mechanical vibrations accurately within a flat passband from 50 to 750 Hz.

This redesign was substantially motivated by the perceptual investigation presented in Chapter 6, where it was required to ensure that the range of vibrotactile stimuli investigated could be presented, as far as possible, without artifacts. In particular, as noted in the paper that follows, the transfer function of the original floor tile display contained a prominent resonance below 400 Hz, a frequency of vibration to which the vibrotactile sense is highly sensitive. Were this resonance not eliminated, most energy in a generic stimulus presented through the tile display would be concentrated near 400 Hz, irrespective of the actual waveform commanded to the actuator. Alternatively, stimuli used in our investigation could have been designed to exclude any frequency content near 400 Hz, but this would have eliminated a frequency band that is highly salient to vibrotactile perception.

Contributions of Authors:

Yon Visell is responsible for the entirety of the work, which was supervised by Prof. Cooperstock, who edited the manuscript of the paper.

Abstract This paper describes the analysis, optimized redesign and evaluation of a high fidelity vibrotactile interface integrated in a rigid surface. The main application of the embodiment described here is vibrotactile display of virtual ground surface material properties for immersive environments, although the design principles are general. The device consists of a light, composite plate mounted on an elastic suspension, with integrated force sensors. It is actuated by a single voice coil motor. The structural dynamics of the device were optimized, within constraints imposed by the requirements of user interaction, and corrected via digital inverse filtering, in order to enable accurate simulation of virtual ground materials. Measurements of the resulting display demonstrate that it is capable of accurately reproducing forces of more than 40 N across a usable frequency band from 50 Hz to 750 Hz.

4.1 Introduction

Vibrotactile display devices consist of palpable interfaces that are capable of vibrating at frequencies salient to human tactile perception, but are not necessarily capable of static force display [104]. Advantages of such displays include their low cost, power efficiency, and capability of rendering transient or textural effects accurately, at high temporal resolution, when suitable actuators are used.

4.1.1 Vibrotactile augmentation of floor surfaces

The work presented here concerns the design of a vibrotactile display device integrated in a rigid panel. The specific embodiment involved is an augmented floor panel designed to enable vibrotactile interaction with ground surfaces. Potential applications of such a device include the simulation of ground textures for virtual and augmented reality simulation [126] or telepresence (e.g., for remote planetary simulation), the rendering of abstract effects or other ecological cues for rehabilitation, or the presentation of tactile feedback to accompany the operation of virtual foot controls, control surfaces, or other interfaces [127]. This device constitutes a redesign and optimization of an interface that was introduced in earlier work by the authors [128]. The goal was to systematically improve its fidelity. One motivation for doing so is to avoid artifacts that can affect realism and prevent careful control of stimuli in experiments involving human vibrotactile perception. The main artifacts alleviated by the redesign are due to selective variations in the device frequency response within the range of

human vibrotactile sensitivity. We have also attempted to provide enough documentation that the device, or others like it, may be produced by researchers or practitioners interested in vibrotactile display via rigid surfaces. The sections that follow present the device concept, its mechanical and electronic structure, the optimizations that were undertaken to improve its dynamic response, and an analysis of the results.

4.1.2 Background

The fidelity of a haptic device depends on the selection and arrangement of electronic components, and on its structural design, as has long been emphasized in the research literature on force-feedback displays. Many of the analogous questions for the design of vibrotactile (VT) displays have received less attention. The vibrotactile augmentation of touch surfaces has been widely investigated for HCI applications [129, 130, 131], although design issues affecting their perceptual transparency have often been neglected. A few examples demonstrating optimized vibrotactile device engineering [132] or software compensation of their dynamics [133] do, nonetheless, exist. Issues related to sensor and actuator selection are covered in recent reviews of haptic hardware prototyping [134], while the extensive literature on acoustic and vibration engineering provide the knowledge needed for structural dynamics optimization [135, 136, 137].

We are not aware of any prior work on the systematic design of vibrotactile floor panels for haptic interaction. Passive floor-based vibrotactile actuation has been used to present low frequency information in audiovisual display applications, for special effects (e.g., vehicle rumble), in immersive cinema or VR settings [138]. The fidelity requirements that must be met by an *interactive* haptic display are, all things being otherwise equal, higher, since its users are able to actively sample its response to actions of the feet.

Many designs for vibrotactile-augmented shoes or insoles have been proposed [139, 140, 141], but nearly all have been designed for symbolic information display (e.g., directional indicators or encoded messages) or biofeedback stimuli, rather than for presenting virtual ecological stimuli. State of the art haptic force feedback interfaces for walking [142] are capable of preserving kinesthetic degrees of freedom but are restricted to a small fraction of the bandwidth that our device achieves. As noted below, a wide bandwidth interface is advantageous for reproducing the rich variety of high-frequency force information that is generated during walking in natural environments [143].

4.2 Display concept and motivation

The interface of the device (Fig. 4.5) consists of a rigid plate that supplies vibrations in response to forces supplied by a user’s foot, via the shoe. The total normal force $F(t)$ applied to the plate by a user is measured. It can be assumed to consist of two components: isolated transients with high frequency content, generated by foot impacts with the plate, and low-frequency forces generated by active human motions, limited in bandwidth to no more than 10 Hz [144, 37]. Vibrotactile feedback is assumed to be constrained, due to actuator limitations, to frequencies greater than a minimum value on the order of 20 Hz.

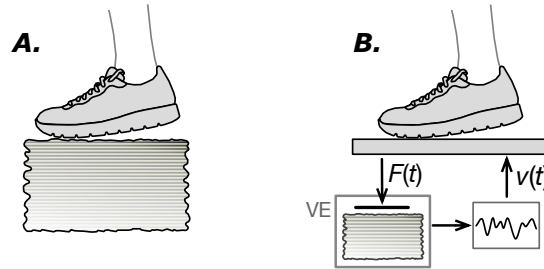


Fig. 4.1 (A.) The experience of stepping onto a deformable object or surface is (B.) simulated via a rigid vibrotactile interface.

A haptic simulation (Fig. 4.1) provides feedback approximating the vibration response felt during interaction with a virtual object. Our rendering algorithms are of admittance type, computing velocities of displacement in response to forces applied to the virtual object. An example of such an algorithm is described in Sec. 4.2.2. As with most vibrotactile displays, vibrations are presented in open loop fashion. During the course of interaction, user coupling to the device interface is expected to vary from no contact to full-foot contact with large forces. In the virtual environment, interaction is mediated by an idealized proxy that is constrained to a constant region on the virtual object surface, at which force is applied. In these respects, the contact state is entirely modeled in the real world (Fig. 4.2). In other words, user-supplied forces (zero or otherwise), as measured by the device, are continuously mapped to the simulation, and there is no modeling of contact variation within the virtual environment.

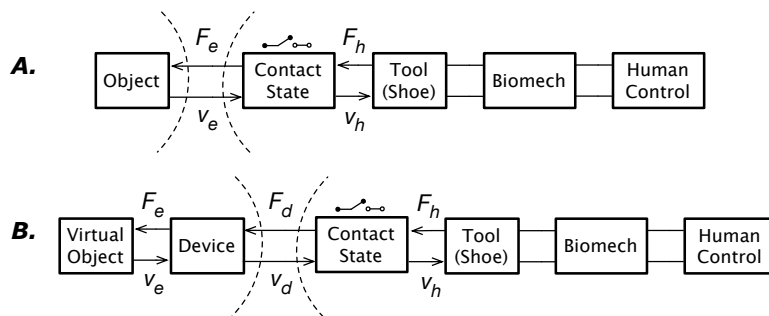


Fig. 4.2 The haptic display concept. (A.) A real system being simulated involves interaction with an object via a tool (the shoe) in a user’s grasp. The user exerts a force $F_h(t)$ and experiences a vibration $v_h(t)$. (B.) The display mediates interaction with the virtual environment. The dashed lines demarcate system components associated with the object, or its haptic presentation, from those of the user.

4.2.1 Transparency

In order to ensure perceptual transparency of the display, the admittance of the virtual object it presents should resemble as closely as possible that of its real counterpart. As illustrated in Figure 4.2, this requires that the (velocity) feedback generated from forces applied to the virtual object closely match those produced by interaction with the real one, and that the device transfer function $H_d(s)$ be as close to unity as possible. Here, we refer to the free (unloaded) response of the display, corresponding to components to the left of the dashed lines in Fig. 4.2. When coupled to a user, the acceleration response of the interface will be modified due to the state of contact between the user and plate, and the biomechanical dynamics of the user (measurements are presented in Sec. 4.5). These variations are beneficial in allowing our device to mimic natural variations in the response of a real object that is being simulated. The dependence of the virtual object response on the force exerted by the user is incorporated explicitly, because our haptic rendering models are force driven. This contrasts with the case of impedance based displays, where only position (or velocity) is measured. In order to ensure transparent open-loop playback of haptic events in settings like the latter, the device’s response requires corrections that account for changes in the display admittance due to grip or arm dynamics [145]. Further discussion is provided in Sec. 4.4.5.

4.2.2 Application to normal force texture simulation

An example application motivating the design reported here is the display of normal force textures, in the form of high frequency vibrations simulating the feel of stepping onto natural ground materials [128]. When a shoe steps onto porous materials like soil or snow, it is subjected to interactions that can include: viscoelastic components, describing the recoverable deformation of the volume of the ground surrounding the contact interface; transient shock components, from the impact of toe and heel against the ground; and plastic components from the collapse of air pockets, brittle structures or granular force chains, resulting in unrecoverable deformation [146, 147]. Combinations of such effects give rise to low-frequency forces and high frequency, texture-like vibrations that are characteristic of human walking on different surfaces [143]. Figure 4.3 presents an example of force and vibration data acquired from one footstep on a gravel surface. Because the vibration signature is continuously coupled to the force input over time in such examples, there is no straightforward way to convincingly use recorded footstep vibrations for vibrotactile rendering, although more flexible granular sound-synthesis methods could be used [148, 149]. For the modeling of simpler interactions, involving impulsive contact with solid materials, recorded transient playback techniques could be used [133].

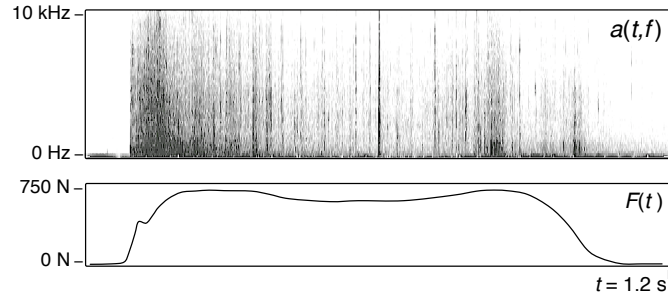


Fig. 4.3 Vibration spectrogram $a(t, f)$ and normal force $F(t)$ measured from one footstep onto rock gravel (Authors' recording). Note the discrete, broad-band impact events evidenced by vertical lines in the spectrogram.

We briefly summarize one approach we have taken to the haptic synthesis of interaction with such surfaces. It is based on fracture mechanics, which has also proved useful for modeling other types of haptic interaction involving damage [150, 151]. Figure 4.4 illustrates the continuum model and a simple mechanical analog used for synthesis. In the stuck state,

the surface has stiffness $K = k_1 + k_2$ and is governed by:

$$F(t) = m\ddot{x} + b\dot{x} + K(x - x_0), \quad x_0 = k_2\xi(t)/K \quad (4.1)$$

where $\xi(t)$ represents the net plastic displacement up to time t . A Mohr-Coulomb yield criterion is applied to determine slip onset: When the force on the plastic unit exceeds a threshold value (which may be constant or noise-dependent), a slip event generates an incremental displacement $\Delta\xi(t)$, along with an energy loss of ΔW representing the inelastic work of fracture growth. Slip displacements are rendered as discrete transients, using an event-based approach [133]. High frequency components of such transient events are known to depend in detail on the materials and forces of interaction, and we model some of these dependencies when synthesizing the transients [152].

A high fidelity vibrotactile display such as that presented here is useful for reproducing such phenomena without artifacts.

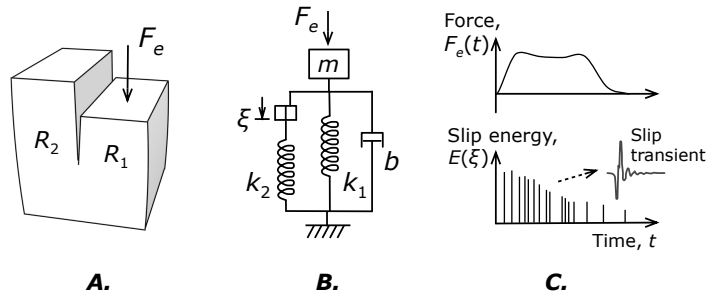


Fig. 4.4 Normal force texture synthesis. *A.* A fracture mechanics approach is adopted. A visco-elasto-plastic body undergoes shear sliding fracture due to applied force F_e . *B.* A simple mechanical analog for the generation of slip events $\xi(t)$ in response to F_e . *C.* For vibrotactile display, each slip event is rendered as an impulsive transient using an event-based approach.

4.3 Components

4.3.1 Mechanical Structure

The mechanical design is broadly similar to that of the original device, but accounts better for both the static and dynamic performance requirements for the display. The top plate provides an interface to the body, which in the case of our device is assumed to consist of a

foot wearing a shoe. Statically, the device must resist bending when loaded vertically by a force of several hundred Newtons. The rigid deflection of the plate under this load must be minimized subject to the constraint that the plate be able to vibrate freely. This trade-off is analyzed in Section 4.4.3.

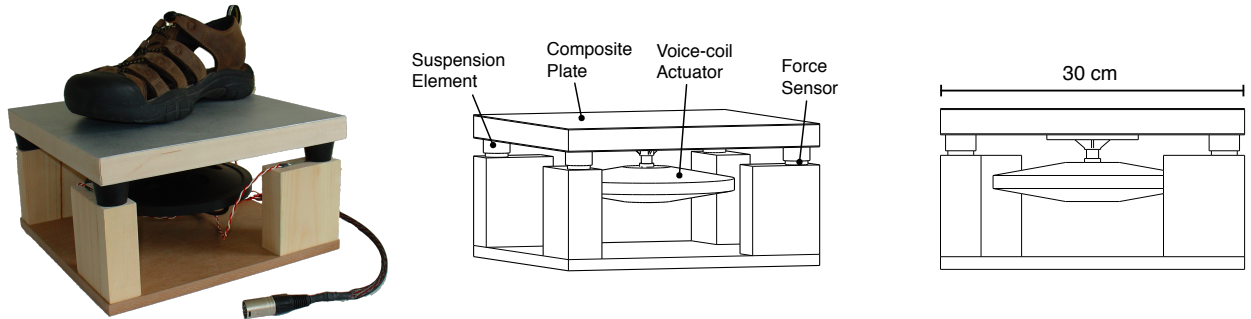


Fig. 4.5 Vibrotactile floor interface hardware for a single tile unit. Left: Photo with large mens' shoe, showing representative size. The model shown is based on the low-cost force sensing resistor option. The cable in the foreground interfaces the sensors with the data acquisition unit. Middle: View showing main components. Right: Side view with top dimension.

The top plate consists of a commercially manufactured aluminum honeycomb sandwich panel component (Museum Services Corp model 0513 SSP) with dimensions $30.4 \times 30.4 \times 2.54$ cm and a weight of 400 g. The panel has aluminum facings with a thickness of 0.08 cm. This material was selected for its high bending stiffness to weight ratio. The panel sides are closed with a basswood frame to eliminate acoustic emissions or deformations that otherwise result from small deflections of the honeycomb at the edges of the panel. The plate is supported by cylindrical SBR rubber elastic elements positioned as shown in Fig. 4.5. In dynamic or multi-tile configurations, a retaining socket surrounding the elastic support (not present in the figure) is used to keep the plate from changing position. The actuator is mounted via an aluminum bracket bonded to the center underside of the plate.

4.3.2 Sensing

In order to render an interactive response from a virtual ground surface using the kinds of models we have developed (Sec. 4.2.2), it is necessary to capture the normal force applied to the tile by the user's foot. Positioning the force sensors beneath the plate is feasible, since the bandwidth of the force applied to the plate by the user is limited. In the design

presented here, the sensors are furthermore positioned beneath the elastic suspension of the device, so as to better isolate them from the actuators.

Force sensing is performed via four load cell force transducers (Measurement Systems model FX19) located below the vibration mount located under each corner of the plate. Although the cost for outfitting a single-plate device with these sensors is not prohibitive, many of the applications we have in mind consist of two dimensional $m \times n$ arrays of tiles, requiring a number $N = 4mn$ of sensors. As a result, in a second configuration, four low-cost resistive force sensors (Interlink model 402 FSR) are used in place of load cells. After conditioning, the response of these sensors to an applied force is nonlinear, and varies up to 25% from part to part (according to manufacturer ratings). Consequently, a measurement and subsequent linearization and force calibration of each is performed, using a calibrated load cell force sensor (details are provided in a separate publication [126]). After such a calibration, a linear response accurate to within 5% can be obtained using low cost parts.

4.3.3 Actuation

The tile is actuated by a single Lorentz force type inertial motor (Clark Synthesis model TST429) with a nominal impedance of 6 Ohms. The actuator is coupled to the tile by a 1.25 cm diameter threaded rod interfacing with an aluminum bracket, as shown in Fig. 4.5. The actuator has a usable bandwidth of about 25 Hz to 20 kHz, and is capable of driving the plate above strongly enough to quickly produce numbness in the region of the foot that is in contact with the tile.

4.3.4 Electronics

Analog data from the force sensors is conditioned, amplified, and digitized via a custom acquisition board, based on an Altera FPGA, with 16-bit analog-to-digital converters. Data from each sensor is sampled at a rate of 1 kHz and transported to a host computer over UDP via the board's 10 Mbps Ethernet interface. Digital to analog conversion of the signal driving the actuator is performed using a low noise 24-bit, 96 kHz audio interface (Edirol model FA-101), and amplification is performed using a compact, class-D audio amplifier based on the Tripath TK2050. The amplifier is rated as capable of providing 100 W to a nominal 4 Ohm actuator impedance.

4.4 Dynamic Response

The main factors affecting the dynamic response of the device are the actuator characteristics, the dynamics of the rigid plate, and that of the elastic suspension. In a suitable regime, one may regard these as lumped linear systems, with respective Laplace transform domain transfer functions $H_a(s)$, $H_p(s)$ and $H_s(s)$. The corresponding model device transfer function can be given by $H_d(s) = H_a(s)H_p(s)H_s(s)$. However, the spatial configuration of these elements relative to each other also contributes to the structural dynamics of the display.

4.4.1 Actuator Response

Fig. 4.6 shows a typical amplitude frequency response for this family of actuators. The data was acquired from an accelerometer attached to the mounting bolt, with the actuator attached to a rigid wooden surface. The shape of this nominal response affects that of our device (Sec. 4.5).

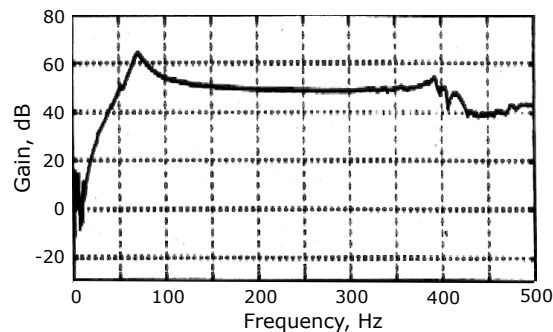


Fig. 4.6 Typical acceleration frequency response of the Clark Synthesis TST family of actuators (manufacturer supplied data, reproduced with permission).

4.4.2 Plate Response

The contribution of the interface plate to the dynamic response of the device can be predicted in terms of the vibrational characteristics of the plate, and the coupling between plate and actuator.

Free response

In the case of a homogeneous, isotropic plate, the free vibrations of interest are governed by a partial differential equation for bending wave displacements. In the thin plate approximation, it is [137]:

$$\rho h \frac{\partial^2 z}{\partial t^2} + D \nabla^4 z = 0, \quad D = \frac{Eh^3}{12(1 - \nu^2)} \quad (4.2)$$

Here, $z = z(\mathbf{r}, t)$ is displacement, $\mathbf{r} = (x, y)$ is a position on the tile surface, t is time, E and ν are the Young's modulus and Poisson's ratio of the plate material, ρ is its mass density, and h is the plate thickness, D is known as the flexural stiffness, and we neglect effects of damping.

Below the first resonant frequency of the plate, f_1 , the vibrational response is well approximated by that of an ideal, rigid mass coupled to an elastic suspension (Sec. 4.4.3 below). Since we seek a usable display bandwidth with an upper limit of 1 kHz, we want to ensure that $f_1 > 1$ kHz. For a rectangular, homogeneous, isotropic plate, the frequencies of the normal modes of bending oscillation are of the form [137]:

$$f(k) = \frac{hk^2}{2\pi} \sqrt{\frac{D}{\rho h}}, \quad k \propto L^{-1} \quad (4.3)$$

Here, k is the magnitude of the wavenumber vector $\mathbf{k} = (k_x, k_y)$ of the oscillation, and L^{-1} is the inverse length of the plate, and x and y are the directions tangent to the plate surface parallel to its edges. For pure simply supported boundary conditions (which are never achieved in practice), $k_x = m\pi/L$ and $k_y = n\pi/L$, where m and n are positive (non-zero) integers [137]. The lowest frequency mode is $f_1 = f(|\mathbf{k}_1|)$, with $\mathbf{k}_1 = (\pi/L, \pi/L)$. The amplitudes of the normal modes are

$$\eta_{mn}(\mathbf{r}) = \sin(k_x x) \sin(k_y y) \quad (4.4)$$

After inserting the form of D from Eq. 4.2 into Eq. 4.3, Poisson's ratio ν contributes a factor $(1 - \nu^2)^{-1/2}$ to $f(k)$. This factor lies in a range from 1.0 to 1.16 for solid materials such as are considered here, so in a first approximation we may ignore it. In order to maximize the frequency $f(k)$ for any given value of the wavenumber magnitude k , and given plate geometric properties L and h , the plate material should be selected to possess a

large Young's modulus E and low mass density ρ . Solid, isotropic materials such as metals can achieve a high stiffness, but their mass density is typically commensurately higher, which is a limitation. In addition, their mass grows linearly with thickness, making them less efficient to actuate. In practice, for a solid plywood plate (light enough to be efficiently actuated) with dimensions $30.4 \text{ cm} \times 30.4 \text{ cm} \times 3.75 \text{ cm}$, one finds $f_1 \approx 400 \text{ Hz}$, which falls short of the design target.

Composite plate

A class of structures that achieves higher stiffness-to-mass ratios than is possible with uniform solids is that of composite sandwiches. Such a panel is formed via the use of thin

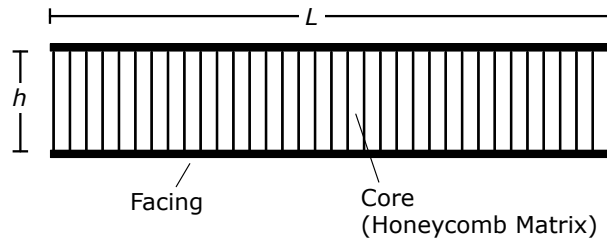


Fig. 4.7 A composite sandwich plate, shown in profile (side view). It consists of a stiff, solid facing material bonded (typically laminated) to a lightweight core, such as a metal or kevlar honeycomb matrix.

layers of stiff solid material bonded to a lightweight core. Fig. 4.7 illustrates a composite sandwich of the type used in our device. The core consists of an aluminum honeycomb matrix, while the facing materials consist of aluminum sheet. An effective model for this material may be developed by replacing the sandwich plate by a homogeneous plate with equivalent rigidity. In this case, the effective elastic modulus for bending deflection is approximately given by $E \approx 2E_f t_f / (\sqrt{3}h)$ [153], where E_f is the Young's modulus of the facing material, t_f is the thickness of the facing material, and h is the core thickness (Fig. 4.7). The corresponding flexural stiffness is approximately $D = E_f t_f h^2 / (6\sqrt{3})$. To a first approximation, the frequencies of the normal modes of bending oscillation of the composite sandwich plate can be obtained from those of the effective homogeneous plate

model, by substituting this expression for E into Eq. 4.3. The resulting frequencies are:¹

$$f(k) = \frac{k^2}{2\pi} \sqrt{\frac{E_f t_f h}{6\sqrt{3}\rho}}, \quad k \propto L^{-1} \quad (4.5)$$

Again, the admissible values of k depend on the boundary conditions. This equation (which is valid only for thin facings $t_f \ll h$) depends on the stiffness E_f of the facing material and the average mass density of the entire panel. For our device, assuming idealized boundary conditions, the minimum value of k is $\pi\sqrt{2}/L$ (see Sec. 4.4.4). The other factors are given by: $h = 2.5$ cm, $t_f = 0.081$ cm, $E_f \approx 68$ GPa, and $\rho \approx 210$ kg / m³. For these values, Eq. (4.5) yields $f_1 \approx 860$ Hz. This overestimates the measured frequency f_1 for our device by approximately 10% (Sec. 4.5).

Actuator coupling

The actuated plate is driven by a surface force (pressure) distribution $F(\mathbf{r}, t)$, and the resulting governing equation possesses a driving term:

$$\rho h \frac{\partial^2 z}{\partial t^2} + D \nabla^4 z = F(\mathbf{r}, t) \quad (4.6)$$

For our device, the latter can be modeled as a $F(\mathbf{r}, t) = F(t)\phi(\mathbf{r})$, where $F(t)$ is the actuator force amplitude, and $\phi(\mathbf{r})$ approximates a spatial Dirac delta function $\delta(\mathbf{r} - \mathbf{r}_0)$ centered at the tile midpoint. Generalizing slightly, one can consider the case of N independent point actuators at locations \mathbf{r}_i , in which case $F(\mathbf{r}) = \sum_{i=1}^N F_i(t)\delta(\mathbf{r} - \mathbf{r}_i)$, where F_i is the force signal from the i th actuator.

An arbitrary displacement $z(\mathbf{r}, t)$ can be expanded in the normal modes $\eta_{mn}(\mathbf{r})$ of vibration, yielding modal coordinates $Z_{mn}(t)$ defined by:

$$z(\mathbf{r}, t) = \sum_{m,n \geq 0} Z_{mn}(t)\eta_{mn}(\mathbf{r}), \quad \text{where} \quad (4.7)$$

$$Z_{mn}(t) = \int z(\mathbf{r}, t)\eta_{mn}(\mathbf{r})d^2\mathbf{r} \quad (4.8)$$

¹The authors did not find this expression for $f(k)$ in the research literature, but approximations like it are presumably well-known.

In these coordinates, the physical equation is [135]:

$$\left(\frac{\partial^2}{\partial t^2} + \omega_{mn}^2\right) Z_{mn}(t) = \sum_i \eta_{mn}(\mathbf{r}_i) F_i(t) \quad (4.9)$$

where ω_{mn} is the angular frequency of mode (m, n) . Modes having nodes at the actuator location, $\eta_{mn}(\mathbf{r}_i) = 0$, satisfy the homogeneous form of Eq. (4.9), so are not excited by the corresponding actuator signal, and instead contribute antiresonances to the device response. As shown in Sec. 4.5, the bandwidth of our device is essentially limited by the antiresonance near 775 Hz for $(m, n) = (1, 1)$.

4.4.3 Elastic Suspension

The actuator is designed to supply a force only along the direction in which it is attached, so we are primarily interested in normal modes of oscillation in the z -direction. To a first approximation, the elastic (SBR rubber) suspension may be treated as a linear, lumped element with stiffness K in the z -direction, coupled to a rigid plate with total mass M (Fig. 4.8). For small displacements, this stiffness is given by $K = EA/h$, where E is the Young's modulus of the suspension element, A is its vertical surface area, and h is its height. When the plate is not subjected to load from a foot, the mass $M = M_0$ is due to the plate and actuator. For the device described here, $M_0 = 2.7$ kg.

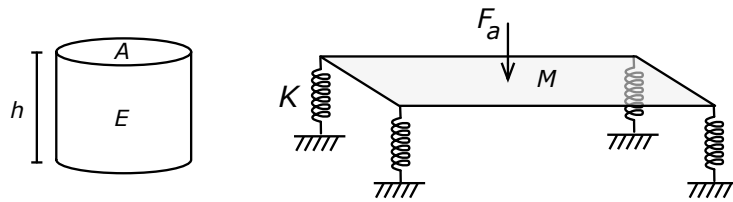


Fig. 4.8 Left: Geometry of one elastic suspension element with height h , cross-sectional area A , and elastic modulus E . Right: Lumped model of the tile-suspension system. F_a is the actuator supplied force, $K = EA/h$ is the stiffness of a suspension element, and M is the combined mass of the actuator and tile.

Due to the symmetric placement of the actuator, there is a single dominant normal mode of oscillation, in which all suspension elements are driven in-phase in the vertical direction. The resonant frequency of this mode in the unloaded condition is given by $f_0 = (2\pi)^{-1} \sqrt{4K/M_0} = (2\pi)^{-1} \sqrt{4EA/(hM_0)}$. Above this frequency, the gain of the

transfer function factor due to the suspension, $H_{susp}(f)$, is expected to be approximately constant.

A softer suspension leads to a larger response bandwidth (i.e., one with a lower frequency extent) but also to a higher static deflection δz under a load F from a foot. The latter two are related by $\delta z = F/K = Fh/(EA)$. As nominal design specifications, we aimed to select E , A and h so that $f_0 \leq 50$ Hz, so that the passband would overlap most of the frequency range of sensitivity of the FA II (Pacinian) tactile mechanoreceptors in the foot. The latter closely resembles the range for those in the hand [18, 101]. In addition, we aimed to achieve a worst-case static deflection $\delta z \leq 5$ mm under a load of $F = 1000$ N, corresponding to a large human balanced at one corner. Both f_0 and δz depend only on the ratio A/h . For convenience, we choose the cross sectional area A of the suspension element to match that of the force sensor. To choose the remaining parameters, we perform a simultaneous grid search on h and E to minimize f_0 and δz . Figure 4.9 illustrates the dependence of f_0 and δz on E for a representative set of selected parameter values, i.e., $A = 8$ cm² and $h = 2.5$ cm. We selected SBR rubber vibration mounts with geometry and Young's modulus $E = 2.0$ MPa consistent with this optimization. As shown in the figure, the resulting system is expected to achieve $f_0 \approx 49$ Hz and $\delta z \approx 4.5$ mm.

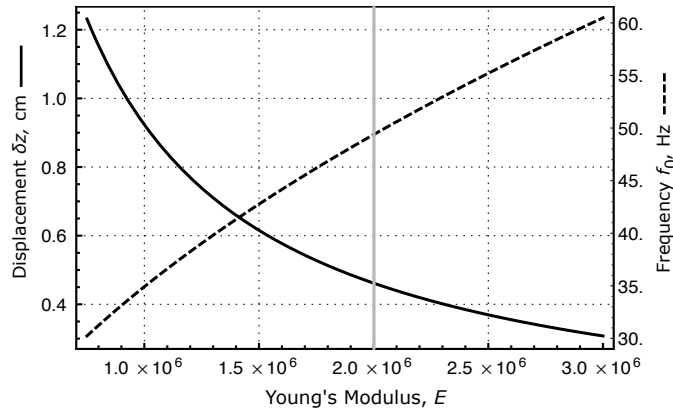


Fig. 4.9 Resonant suspension frequency f_0 and static deflection δz vs. Young's modulus for the system model with $A = 8$ cm² and $h = 2.5$ cm. The value $E = 2$ MPa (grey vertical line) satisfies $f_0 < 50$ Hz and $\delta z < 5$ mm.

4.4.4 Simulation

The vibrational characteristics of the tile-actuator system were simulated using finite element method (FEM) analysis. A three-dimensional geometric model of the device was designed, incorporating the sandwich panel, actuator (modeled as a homogeneous cylindrical mass), actuator bracket and connecting rod, elastic elements, and supporting structure. Material properties were assigned approximating those of the device itself, with the core honeycomb matrix replaced by a homogeneous solid with an equivalent density. Although this model entails a number of approximations, the qualitative results were expected to be correct.

Eigenfrequency analysis

At high frequencies, the resonant modes of the plate itself are observed. The first two are shown in Fig. 4.10. The lowest frequency mode has wavenumber $\mathbf{k} = (1, 1)$, while the next highest resonance shown appears to correspond to a plate-induced mixture of the $(0, 2)$ and $(2, 0)$ modes. Their frequencies, 896 Hz and 1032 Hz, lie at a ratio of about 1.15:1.

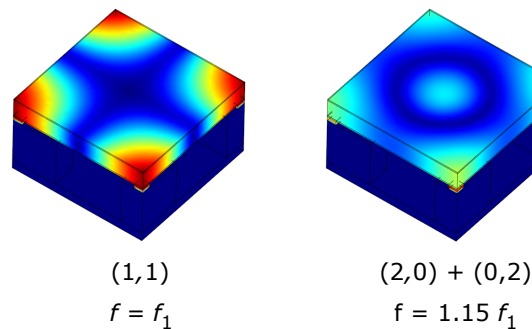


Fig. 4.10 Visualization of the first two resonant modes of the device due to the bending mode vibrations of the plate as identified in the FEM analysis. The ring mode (right side) arises from the mixing of the plate modes indexed by the integers shown [137]. The frequencies are 896 Hz and 1032 Hz.

At low frequencies, a series of six resonances at frequencies of 28, 45, 51, and 77 Hz is observed, corresponding to deformations of the elastic support elements, in agreement with the lumped model of Sec. 4.4.3. The number of resonances exactly matches the six degrees of freedom of perturbation of the rigid tile. The deformation shapes recovered from the FEM analysis show that the 45 Hz resonance corresponds to oscillation in the direction

normal to the plate surface; it is expected to dominate when the display is driven by the actuator.

Frequency response simulation

The FEM simulation of the frequency response was performed with a sinusoidal driving signal originating at the actuator. The z -axis acceleration was measured at several points on the surface of the plate, with the results shown in Fig. 4.11. As determined above, the cross-shaped mode gives rise to an antiresonance, due to the actuator location. The magnitude effect of these resonances, and to a secondary degree their frequency, depends substantially on the measuring point.

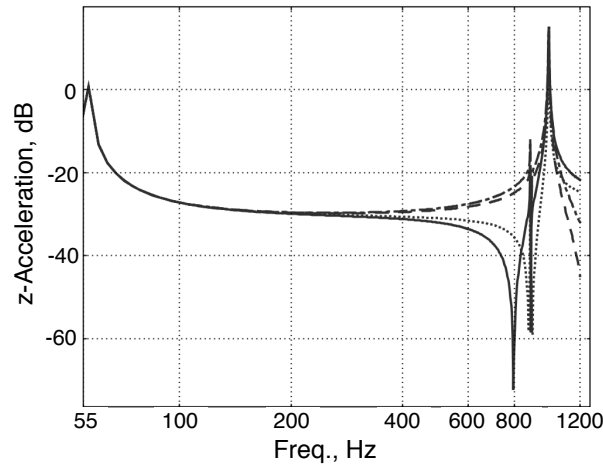


Fig. 4.11 Result of a FEM analysis of the acceleration response of the device as measured at four different points on the plate surface. At frequencies below the first resonant mode of the plate and above the dominant resonant mode of the suspension, the device response is approximately constant and independent of location on the plate.

4.4.5 Modeling user-supplied loads

We have so far discussed the response of the device without accounting for effect of to its user. According to the haptic interaction model adopted here (Sec. 4.2) it is correct to ignore the influence of this load, as transparency requires that the free (unloaded) display transfer function approach unity. However, in other circumstances it may be desirable to compensate for variations in the display response due to user contact. Examples where

this might be the case include passive vibrotactile stimulation for tactile communication or psychophysical experiments, or for use with impedance-based rendering algorithms or simulations that explicitly model user contact conditions in the virtual environment. At

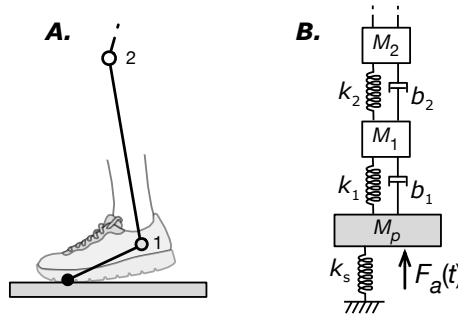


Fig. 4.12 (A.) A simplified model of a user-supplied load can be provided in the form of a link-segment model or (B.) its equivalent mechanical network, coupled to the display device. $F_a(t)$ is force applied by the actuator.

the frequencies of interest, a user may be modeled as a passive viscoelastic mechanical system. Figure 4.12 shows a simple link-segment biomechanical model and equivalent mechanical network coupled to the display. Physiologically, biomechanical properties such as leg joint stiffness cannot be regarded as static or linear during movement, as muscular activation regularly modulates the dynamic properties of the lower limbs during activities on foot [154, 155, 156]. However, as a typical leg stiffness value one may take $k = 30$ kN/m [154]. Upon adopting a simple, single mass-spring-damper model with this value, and assuming an effective mass of 50 kg, one finds that a user-supplied load should most influence frequencies near 150 Hz, in agreement with published measurements [157]. This prediction is also consistent with the load-dependent frequency response measurements we report below (Sec. 4.5.1). Similar grip-dependent effects are observed to affect manually operated haptic [158, 145] and vibrotactile [132] devices.

4.5 Evaluation

As noted in Sec. 4.2.1, our assessment of the transparency of this device is based on the extent to which the unloaded transfer function of the display approximates unity over the range of perceptually salient frequencies. We focus here on the flatness of the magnitude frequency response. The vibrotactile sense is sensitive to phase differences [159], and it

is possible that a vibrotactile display may contribute enough phase distortion to affect perception, particularly where transient signal components are concerned. However knowledge about vibrotactile sensitivity to temporal phase distortion is incomplete, and, as far as we are aware, phase linearity has never been used to evaluate vibrotactile displays. It is nonetheless an important consideration in the related field of loudspeaker design.

4.5.1 Frequency response measurement

The magnitude frequency response of the device was measured by driving the plate with the actuator using the chirp method, with a slow sinusoidal frequency sweep (rate of 100 Hz / s). Measurement was performed using a piezoelectric accelerometer (AKG model CP-411) bonded to the top surface of the plate, as described in the caption of Fig. 4.13. Frequency response measurements were taken for several different foot-plate contact conditions, while the foot was wearing a rubber soled shoe. As noted above, these contact conditions modify the impedance of the display, altering its response. The results are shown in Fig. 4.13.

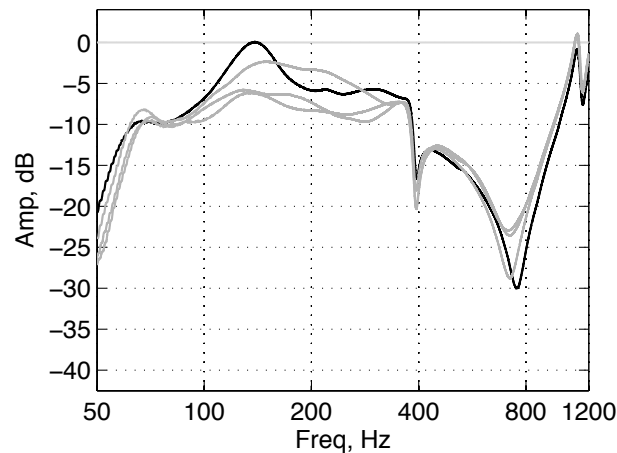


Fig. 4.13 The measured log magnitude frequency response of the display. Measurements were taken at a point equidistant from the plate center and edge, on a line through the center, 15 degrees from the diagonal. The free response is shown with a black line, and other foot-floor contact conditions with varying load applied via the foot are shown in gray.

The variation in the magnitude frequency response below 800 Hz is, following the analysis above, probably attributable to a combination of the resonant modes of the vibration suspension and the actuator response (Fig. 4.6). The antiresonance around 775 Hz and the resonance near 1100 Hz are due to the two lowest frequency normal modes of the plate

(Fig. 4.10) identified above. Variation in the range from 70 Hz to 700 Hz can be attributed in part to the actuator response. The latter (Fig. 4.6) includes a resonance near 70 Hz and additional coloration above 380 Hz, likely accounting for the smaller notch seen in the measurements. Through additional measurements with a calibrated accelerometer (Analog devices model ADXL 320), it was determined that a force of 40 N could be transmitted at all frequencies between 50 and 750 Hz. Another pertinent quantity, nonlinear distortion, was estimated from measurements at 300 Hz to be slightly more than 5% (mean absolute percent error) up to a force of 30 N.

4.5.2 Digital correction

It is possible to improve the nominal frequency response $H_d(f)$ of the display by filtering the actuator signal $F(t)$ via a suitably designed linear, time-invariant corrective filter, H_c . Here, we concentrate on the magnitude only: H_c is designed so that the corrected device frequency response $H_{d'}(f) = H_d(f)H_c(f) \approx g$ in the band of interest, where g is a constant gain factor.

Since such a filter lacks any spatial dependency, correction is most effective below the first resonant frequency of the device, f_1 , because above it the device transfer function varies across the surface of the plate (Fig. 4.11). As a result, correction is primarily useful for compensating factors, such as actuator characteristics, that can be treated as lumped parameter system elements.

We designed the inverse filter H_c to equalize the device response in the frequency range from $f = 50$ Hz to 750 Hz. It was implemented digitally as an IIR filter of order N , which was estimated using the least p -th norm optimization method [160]. Figure 4.14 shows a comparison of the original (free) frequency response of the device with responses corrected by filters of order $N = 10$ and 14. In the latter case, the response is flat in a passband with -10 dB roll off near 50 Hz and 750 Hz.

4.6 Conclusion

We have presented a vibrotactile display device integrated in a rigid surface, consisting of an actuated and instrumented floor tile. The analysis considered factors affecting the bandwidth of the device, including the response of the elastic suspension and rigid plate, the actuator coupling, and the static deflection of the suspension under load by a human

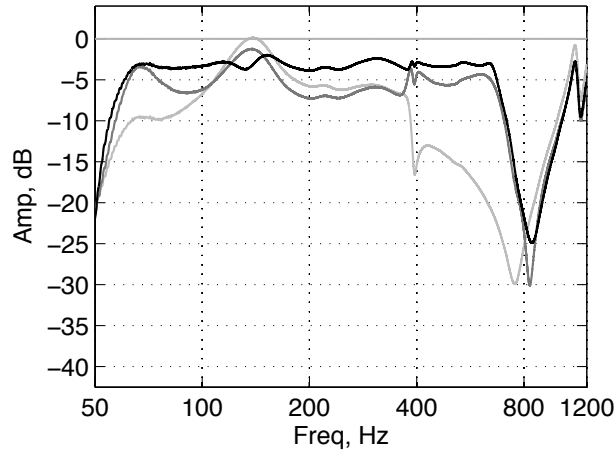


Fig. 4.14 Measured device response without foot contact, uncorrected (lightest gray) and with correction by digital IIR filters of order $N = 10$ (medium gray) and $N = 14$ (black).

foot. The plate was implemented as a lightweight composite sandwich panel constructed from aluminum honeycomb. A digital filter was designed to compensate for artifacts in the measured frequency response. The device allows for accurate reproduction of frequencies between about 50 and 750 Hz.

The device is simple, and designed to be easily reproducible or adaptable to the demands of various applications or research tasks [37, 152]. Formulae such as Eq. (4.5) indicate how the response characteristics of the display can be expected to scale with system dimensions.

Despite these results, a number of areas can be identified in which the device might be improved. They include:

- *Plate material selection:* As presented in the analysis above, a composite panel similar to that used here, but constructed from a honeycomb core with larger core thickness h , and facing thickness t_f would achieve a usable bandwidth that extends to higher frequencies. The first resonant frequency of the plate scales as $\sqrt{t_f h}$ in the thin plate approximation (which will require corrections if the plate or facings are too thick).
- *Actuator design:* The large voice coil actuator used in the present device introduces significant coloration in the frequency response of the device, much of which can be equalized. A better response may be achieved through the use of smaller, more efficient voice coil motors coupled to the structure in a spatial configuration chosen to optimize the device transfer function.

- *Vibration control:* Active structural vibration control strategies exist that could improve the fidelity of such a display using arrays of surface mounted sensors and actuators, together with closed-loop controllers [161, 162, 163]. Such techniques might be used to achieve accurately controlled vibrational responses under a wider array of contact loads.

In ongoing research in our lab, the device is being utilized to study the rendering and display of virtual ground surface properties, related aspects of haptic perception, and the integration of such display components in multimodal virtual and augmented reality environments [126].

Appendix: Erratum to “Design of a Vibrotactile Display via a Rigid Surface”

In the caption to Figure 4.2, the flow variable $v_h(t)$ in a two-port network description of the vibrotactile display is described as a “vibration”. It should, more precisely, be described as the velocity of mechanical vibrations returned to the foot.

Chapter 5

Interaction Techniques

© 2010 IEEE Reprinted, with permission, from

Yon Visell, Severin Smith, Alvin Law, Rishi Rajalingham, and Jeremy Cooperstock, “Contact Sensing and Interaction Techniques for a Distributed, Multimodal Floor Display.” *Proc. of the IEEE Symposium on 3D User Interfaces (3DUI)*, 2010, pp. 75–78.

and from

Yon Visell, Alvin Law, Severin Smith, Jessica Ip, and Jeremy Cooperstock, “Interaction Capture in Immersive Environments via an Intelligent Floor Surface.” *Proc. of IEEE Virtual Reality*, 2010, pp. 313–314.

Copyright notice:

This material is posted here with permission of the IEEE. Such permission of the IEEE does not in any way imply IEEE endorsement of any of McGill University’s products or services. Internal or personal use of this material is permitted. However, permission to reprint/republish this material for advertising or promotional purposes or for creating new collective works for resale or redistribution must be obtained from the IEEE by writing to pubs-permissions@ieee.org.

By choosing to view this material, you agree to all provisions of the copyright laws protecting it.

Preface to Chapter 5:

This chapter presents a distributed, networked version of the floor interface described in the preceding chapters, and introduces new techniques for interacting with it via the feet, based on the identification of contact pressure centroids that can be accurately estimated from intrinsic force measurements acquired from the distributed array of floor tiles. This method makes it possible for users to interact with simulated, multimodal ground material simulations or touch surface interfaces distributed over an extended area. The empirical study included here is one of the first to investigate the usability of floor-based touch surface interfaces.

Contributions of Authors:

Yon Visell designed the apparatus, vibrotactile feedback, and sensing method. He also performed the sensor calibrations and collected sensor data, designed, implemented, and ran the experiments, analyzed the experimental data, prepared the figures and wrote the manuscript. Severin Smith developed the application software layer implementing the sensing method, and implemented the touch surface demonstrations. Alvin Law implemented the hardware interface and contributed to its design, and, together with Jessica Ip, developed the ice demonstration. Rishi Rajalingham contributed to the sensor calibration and data collection. Prof. Cooperstock supervised the research and edited the manuscript.

Abstract This chapter presents an interface and set of techniques for interacting via the feet with computationally augmented floor surfaces. It is based on an array of instrumented floor tiles distributed over an area of several square meters. Intrinsic force sensing is used to capture foot-floor contact at resolutions as fine as 2 cm. The interface was used for user input in a multimodal touch surface paradigm, and for immersive simulation of virtual walking terrains in an augmented reality environment. Auditory and vibrotactile feedback are synthesized in response to movements or control actions of the feet. A preliminary usability evaluation via a target selection task was conducted. It suggests that selectable interface elements should be at least 7.5 cm wide to be reliably selected, and that, when users are stationary, interaction is most efficient within a frontal workspace area extending from 15 to 45 cm from the feet.

5.1 Introduction

To date, there has been limited research on foot-based interaction for computationally augmented environments. Arguably, one reason for this has been a lack of efficient interfaces and interaction techniques capable of capturing touch via the feet over a distributed display. In the present contribution, we describe the design of an interface based on a distributed network of low-cost, rigid floor tile components, with integrated sensing and actuation. Taking advantage of the particular structure of this interface, we draw on contact sensing techniques, through which we capture foot-floor contact loci with finer resolution than would be achieved if a single tile were regarded as the smallest relevant spatial unit, and use these contact points for interaction with virtual ground terrains and touch-surface user interfaces.

5.2 Background

Examples of the use of foot-controlled input in HCI, interactive arts and video gaming date at least to the early 1980s, with Amiga's Joypad (1983) being one widely known example [63]. In the mid 1980s, Pearson and Weiser investigated foot input devices for desktop PCs, and invented a pedal-like device called the Mole [64]. However, despite the high-level of interest in touch screens for the hands, less research and development has targeted touch-sensitive interfaces for the feet. Companies such as Gesturetek and Reactrix

have developed interactive floor-based visual displays using video sensing technology, but such sensors provide no direct information about foot-floor contact forces and positions. This information is arguably important for rendering interactions with virtual objects or controls, or for simulating highly contact-dependent interactions with virtual materials.

Tactile sensing for interaction with floor surfaces has conventionally been accomplished with surface-mounted sensing arrays [74, 164]. It has been applied to problems such as person tracking, activity tracking, or musical performance. Floor-mounted tactile sensing arrays are now commercially available, but costs are high and support for real-time interaction is limited due to their proprietary nature, and orientation toward applications in offline gait and posture measurement.

Sensations accompanying walking on natural ground surfaces in real world environments (sand in the desert, or snow in winter) are rich, multimodal and highly evocative of the settings in which they occur [37]. However, floor-based multimodal (visual, auditory, tactile) information displays have only recently begun to be investigated [152]. Related research on virtual and augmented reality environments has focused on the problem of natural navigation in virtual reality environments. Solutions such as walking in place [55] and redirected walking techniques [56] map body movements sensed through kinematic tracking onto a user's coordinates in a virtual environment (VE). The shoe-based Step WIM interface of LaViola et al. [66] introduced additional foot gestures for controlling navigation in a larger VE via a floor map, but required special shoes and did not provide auditory or haptic feedback. A number of haptic interfaces for enabling omnidirectional in-place locomotion in VEs have been developed [53], but known solutions either limit freedom in walking, or are highly complex and costly.

5.2.1 Floor Touch User Interfaces: Potential application space

Virtual floor controls could be advantageous in areas of man-machine interaction in which foot operated controls or interfaces are already commonplace, such as manufacturing assembly and repair, mass transportation, vehicle operation, or dentistry. A virtualized display can be used to provide access to instrumentation or machine controls in a way that is flexible to different contexts of use (e.g., different dental procedures). Such an approach may overcome acknowledged problems with the proliferation of physical foot pedals and other controllers in medical interactions [165]. Applications to pedestrian navigation or map-

based visualization could emerge as particularly salient, insofar as they may integrate the role of the foot in self-motion. Previously investigated applications of immersive virtual reality, such as architectural walkthroughs or training simulation, may benefit from the addition of context-based interactive maps or menus, as in the investigation of LaViola et al. [66]. Other relevant application fields could include entertainment, music performance, gaming, or advertising, where companies such as Gesturetek and Reactrix have successfully commercialized interactive, floor-based visual displays for marketing purposes.

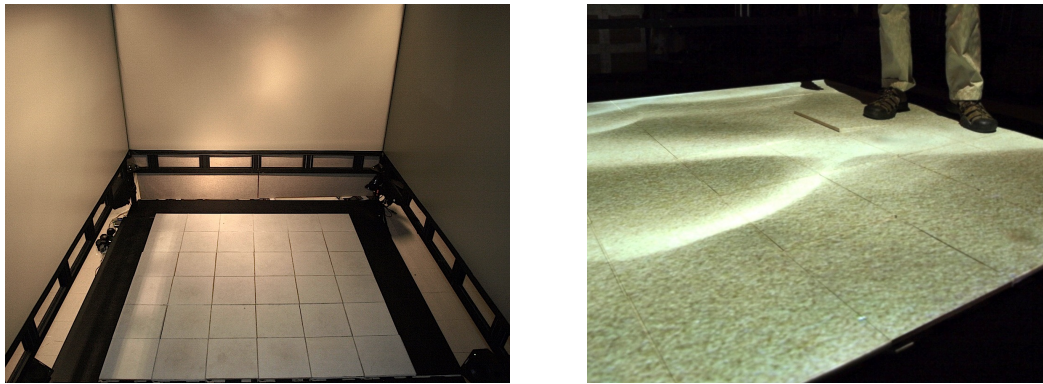


Fig. 5.1 Left: The floor interface is situated within an immersive, rear projected virtual environment simulator. Right: Visual feedback is provided by top-down video projection.

5.3 System

The interface (Fig. 5.2) consists of a square array of 36 rigid tiles, each of which is instrumented with force sensors (four per tile) and a vibrotactile actuator. The floor is coated in reflective projection paint. A pair of overhead video projectors is available for visual display, reducing the effects of shadows cast by users. The individual tile interfaces are rigid, plywood plates with dimensions $30.5 \times 30.5 \times 2$ cm, supported by elastic vibration mounts, and coupled to a vibrotactile actuator (Clark Synthesis, model TST229) beneath each plate [166]. Actuator signals are generated on personal computers, output via digital audio interfaces, and amplified.

Normal forces are sensed at locations below the corner vibration supports of each tile using a total of four resistive force sensors (Interlink model 402 FSR). Analog data from the force sensors is conditioned, amplified, and digitized via a 32-channel, 16-bit data

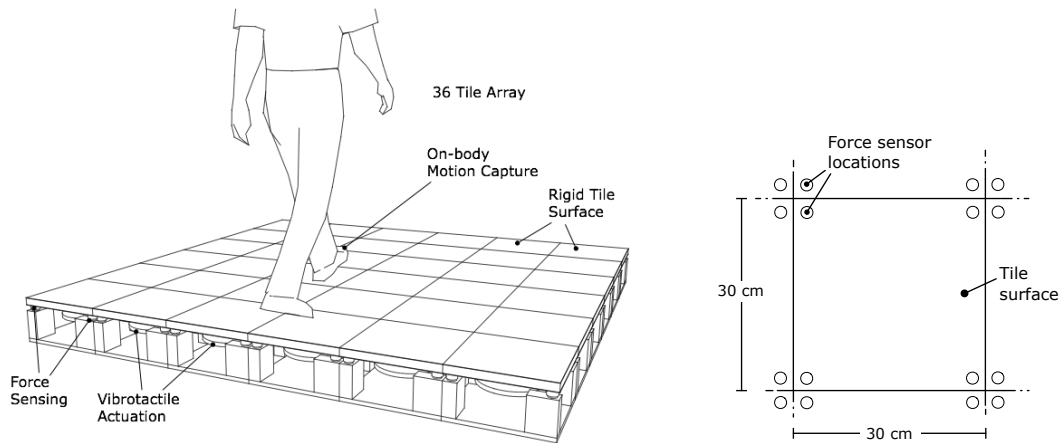


Fig. 5.2 Left: Diagrammatic view of the interface. Sensing and actuating components are integrated beneath the floor. Right: View from above showing sensor locations.

acquisition board based on an Altera FPGA. Each sensor is sampled at a rate of up to 1 kHz transmitted over a low-latency Ethernet link. An array of six small form factor computers is used for force data processing and audio and vibrotactile rendering. A separate, networked server is responsible for rendering visual feedback and managing user input.

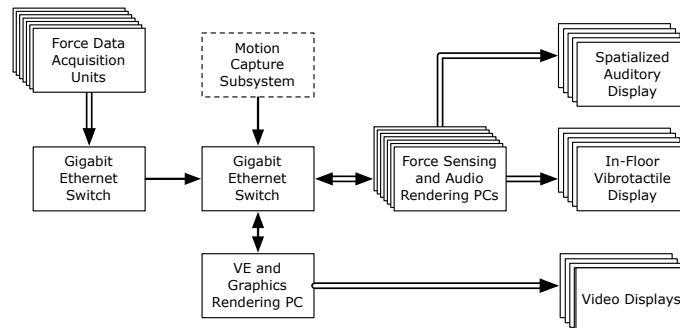


Fig. 5.3 Overview of system components and logical connections between them.

5.4 Contact sensing

For processing sensor data, we draw on intrinsic contact sensing, which aim to resolve the locations of contact, the forces at the interface, and the moment about the contact normals using internal force and torque measurements [167]. It is assumed to involve

contact between a rigid object and a soft body (here, a foot), and has been previously used for robotic manipulation. Here we use it for capturing foot-ground interactions via in-floor force sensors. It requires a number of sensors on the order of the number of rigid degrees of freedom of the structure, far fewer than are needed for tactile sensing via surface mounted arrays. Since a tile has fewer sensors than rigid body degrees of freedom, we make the simplifying assumption of frictionless contact via a normally directed pressure distribution, and further assume that the relative displacement of the suspension elements in the tile is negligible. The problem is then to resolve the location of a contact centroid \mathbf{x}_c associated with a normal force distribution $p_R(\mathbf{x})$ within an area R . In our context, \mathbf{x}_c is a contact point such that a normal force F_c at \mathbf{x}_c gives rise to the same measurements as $p_R(\mathbf{x})$ does [167]. For a floor tile with sensor locations \mathbf{x}_j where measurements f_j are taken (j indexes the tile sensors), \mathbf{x}_c and the normal force $\mathcal{F}_c = (0, 0, F_c)$ can be recovered from scalar measurements $\mathcal{F}_j = (0, 0, f_j)$ via the force and torque equilibrium equations,

$$\sum_{j=1}^4 f_j + F_c + f_p = 0 \quad (5.1)$$

$$\sum_{j=1}^4 \mathbf{x}_j \times \mathcal{F}_j + \mathbf{x}_c \times \mathcal{F}_c + \mathbf{x}_p \times \mathcal{F}_p = 0. \quad (5.2)$$

$\mathcal{F}_p = (0, 0, f_p)$ is the weight of the the plate and actuator at the tile's center \mathbf{x}_p . The three nontrivial scalar equalities (5.1, 5.2) yield:

$$F_c = \sum_{i=1}^4 f_i - f_p, \quad \mathbf{x}_c = \frac{1}{F_c} \left(\sum_{i=1}^4 (\mathbf{x}_i - \mathbf{x}_p) f_i + f_c \mathbf{x}_p \right) \quad (5.3)$$

The contact centroid lies within the convex hull of the contact area (dashed line, Fig. 5.4) at the centroid of the pressure distribution [167], and thus provides a concise summary of the foot-floor contact locus, but not about shape or orientation. When the foot-floor contact area R overlaps multiple tiles, a pressure centroid \mathbf{x}_c for the entire area can be computed from those \mathbf{x}_{ck} for each tile (computed from Eq. (5.3)), via $\mathbf{x}_c = w_1 \mathbf{x}_{c1} + w_2 \mathbf{x}_{c2}$, where $w_k = F_i/F$. The domain-independence of this result makes it possible to continuously track contact across tile boundaries. The difference vector $\delta \mathbf{x} = \mathbf{x}_{c1} - \mathbf{x}_{c2}$ provides additional shape information about the orientation of the contact distribution at the boundary. For

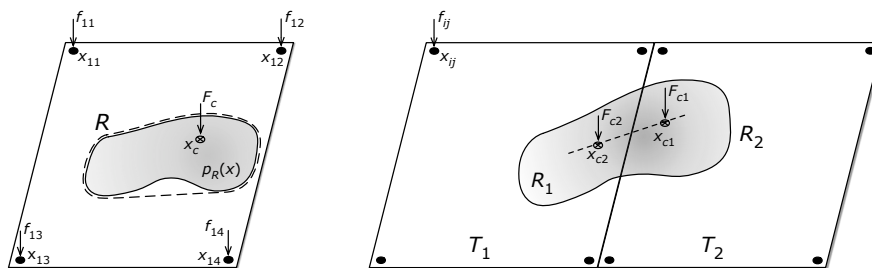


Fig. 5.4 Left: A normal force distribution $p_R(\mathbf{x})$ and associated contact centroid position \mathbf{x}_c . Right: A pressure distribution $p_R(\mathbf{x})$ on a region R spanning adjacent tiles. The weighted sum of centroids \mathbf{x}_c is the centroid location for the distribution with support $R = R_1 \cup R_2$. It lies on the line segment connecting \mathbf{x}_{c1} and \mathbf{x}_{c2} . The difference $\delta\mathbf{x} = \mathbf{x}_{c1} - \mathbf{x}_{c2}$ provides information about contact shape

a linear pressure distribution spanning the two tiles, the direction vector $\mathbf{n} = \delta\mathbf{x}/|\delta\mathbf{x}|$ is the orientation, and $|\delta\mathbf{x}|$ is half of the length of R . For convex contact shapes that are less sharply oriented (such as those of a foot), the range of angles is compressed around the edge normal direction.

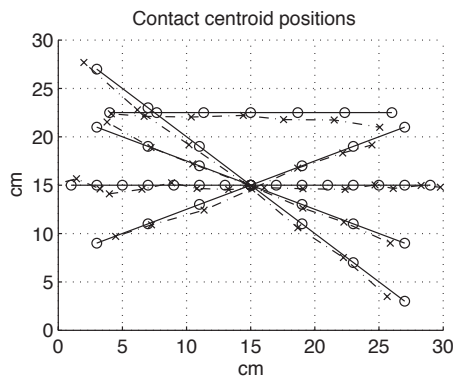


Fig. 5.5 Results of 50 measurements comparing true normal force positions (circles) with contact centroid estimates (Xs).

Figure 5.6 shows the sequence of contact centroid locations produced by an individual walking across the floor. When there is multi-tile foot-floor contact, as illustrated here, we use a simple clustering algorithm to associate nearby contact centroids that are assumed to belong to the same foot.

Figure 5.5 presents measurements of 50 estimated contact positions determined by the method of Eq. (5.3), using a single calibrated floor tile. Despite distortion near tile edges,

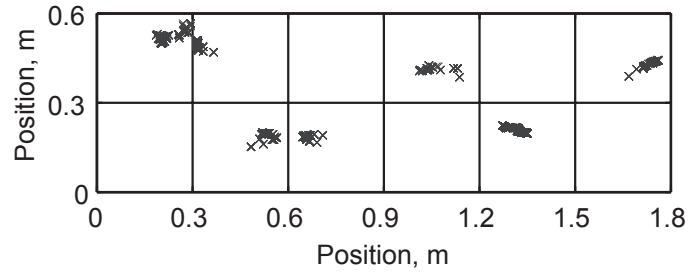


Fig. 5.6 A recorded sequence of contact centroids produced by an individual walking across the floor. Each square corresponds to one floor tile. When the foot lies on a single tile, as weight shifts from heel to toe, an array of centroids is produced, moving in the direction of travel. At inter-tile boundaries, at each instant one centroid is produced on each tile that there is contact with.

contacts were localized with a typical accuracy of 2 cm, and worst-case values of ≈ 3 cm, smaller than the linear dimensions of the tile (30 cm) or the typical width of an adult shoe.

5.5 Channeling material interactions

To demonstrate this interface and interaction techniques, we designed a virtual frozen pond demonstration that users may walk on, producing patterns of surface cracks that are rendered and displayed via audio, visual, and vibrotactile channels (Fig. 5.7).

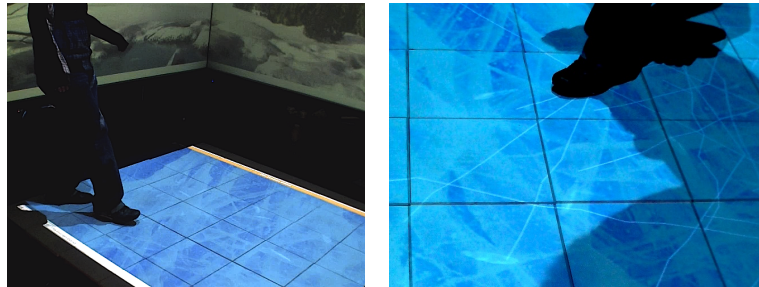


Fig. 5.7 Still images of users interacting with the simulated frozen pond.

5.5.1 Non-visual rendering

In the demonstration, audio and vibrotactile feedback accompany the fracture of the virtual ice sheet underfoot. The two are derived from a simplified mechanical model. Fracture events are characterized via an event time t_i and energy loss E_i . Figure 5.8 illustrates the

local continuum description and a simple mechanical analog used for synthesis. In this model, in the stuck state, the surface has stiffness $K = k_1 + k_2$ and is governed by:

$$F(t) = m\ddot{x} + b\dot{x} + K(x - x_0), \quad x_0 = k_2\xi(t)/K \quad (5.4)$$

where $\xi(t)$ represents the net plastic displacement up to time t . A Mohr-Coulomb yield criterion determines slip onset: When the force F_ξ on the plastic unit exceeds a threshold F_0 (either a constant value or one sampled from a random process), a slip event is generated with energy loss E_i , representing the inelastic work of fracture growth. E_i is sampled from an exponential distribution $p(E) \propto E^{-\gamma}$ with a scale parameter γ that is, for many fracture processes, an approximate invariant of the material medium [37]. Slip displacements are rendered as transients given by a coupled model consisting of a nonlinear impulse coupled with a bank of modal oscillators with impulse response $s(t) = \sum_i a_i e^{-b_i t} \sin(2\pi f_i t)$, determined by amplitudes a_i , decay rates b_i , and frequencies f_i [99, 121]. A transient impulse at time t_0 is modeled phenomenologically as a nonlinear viscoelastic impact with effective force $f(t) \propto \Delta W$, simulated via the Hunt-Crossley impact model [168]

$$f(t) = kx(t)^\alpha - \lambda x(t)^\alpha \dot{x}(t). \quad (5.5)$$

$x(t)$ is the compression displacement and $\dot{x}(t)$ is the compression velocity. The impact has effective parameters governing stiffness k , dissipation λ , and contact shape α .

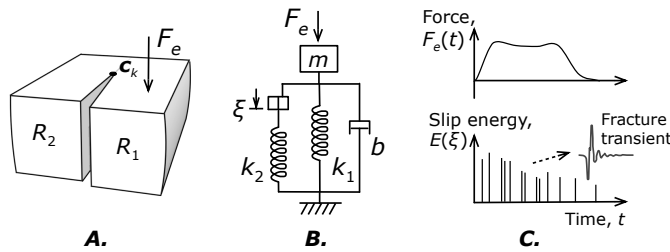


Fig. 5.8 A. Behavior at the crack front \mathbf{c}_k is modeled using a simplified fracture mechanics treatment. A visco-elasto-plastic body undergoes shear sliding fracture. B. A simple mechanical analog. C. Each slip event is rendered as an impulsive transient.

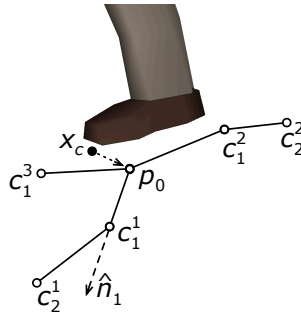


Fig. 5.9 A crack pattern, modeled as a graph of lines between nodes \mathbf{c}_i extending from the seed location p_0 .

5.5.2 Visual animation and control

Brittle fracture in computer graphics is often animated by simulating the inelastic evolution of a distributed stress state [92, 91]. Here, we adopted a simplified simulation to fuse the local temporal crack-growth model given above with a heuristic for spatial crack pattern growth. The contact centroid \mathbf{x}_c summarizes the local stress due to the load from a foot. A fracture pattern consists of a collection of crack fronts, defined by linear sequences of node positions, $\mathbf{c}_0, \mathbf{c}_1, \dots, \mathbf{c}_n$. Fronts originate at seed locations $\mathbf{p} = \mathbf{c}_0$. The fracture is rendered as line primitives $\ell_k = (\mathbf{c}_k - \mathbf{c}_{k-1})$ on the ice sheet (Fig. 5.9). Seed locations \mathbf{p} are determined by foot-floor contact. A crack event initiated by the audio-tactile process at time t_i with energy $E(t_i)$ results in the creation of a new seed or the growth of fractures from an existing one. In the former case, a new seed \mathbf{p} is formed at the location of the dominant contact centroid \mathbf{x}_c if no existing seed lies within distance Δp . The seed \mathbf{p} is created with a random number N_c of latent crack fronts, $\mathbf{c}_0^1, \mathbf{c}_0^2, \dots, \mathbf{c}_0^{N_c}$. We sample N_c uniformly in $2, 3, \dots, 6$. A crack front propagates from a seed \mathbf{p} nearest to \mathbf{x}_c . With probability $1/N_c$ the j th crack front of \mathbf{p} is extended. Its growth is determined by a propagation vector \mathbf{d}_m^j such that $\mathbf{c}_m^j = \mathbf{c}_{m-1}^j + \mathbf{d}_m^j$. We take $\mathbf{d}_m^j = \alpha E \hat{\mathbf{n}}_m^j$, where E is the crack energy, α is a global growth rate parameter, and $\hat{\mathbf{n}}_m^j$ is the direction. Since we lack information about the principal stress directions at the front, we propagate in a random direction given by $\hat{\mathbf{n}}_m^j = \hat{\mathbf{n}}_{m-1}^j + \beta \hat{\mathbf{t}}$, where $\beta \sim N(\beta; 0, \sigma)$ is a Gaussian random variable and $\hat{\mathbf{t}} = \hat{\mathbf{n}}^j \times \hat{\mathbf{u}}$, where $\hat{\mathbf{u}}$ is the upward surface normal (i.e., $\hat{\mathbf{t}}$ is a unit vector tangent to $\hat{\mathbf{n}}^j$). The initial directions at \mathbf{p} are spaced equally on the circle.

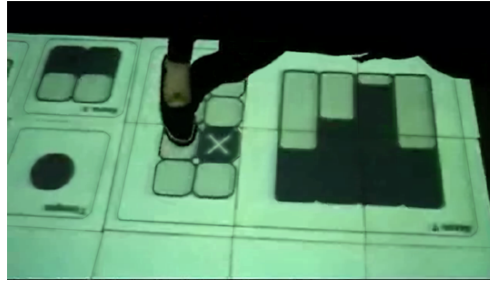


Fig. 5.10 Still image from video of a user interacting with floor-based interface widgets.

5.6 Floor Touch Surface Interfaces

These sensing methods can be employed to implement virtual floor-based touch interfaces. One set of examples we have created consist of array of standard UI widgets to be controlled with the feet (Fig. 5.10). Input is based on a multi-touch screen metaphor mediated by a set of interaction points (cursor locations), which are defined as the contact centroids \mathbf{x}_c with the largest forces. Force thresholds associated with a control are used to determine selection. The controls provide positive tactile feedback supplied by the actuators, in the form of synthesized click-like transient vibrations or sliding (friction) vibrations.

Interface design toolkit We developed a software layer and network protocol to facilitate the design of interactive applications using the floor surface. It abstracts the hardware systems, which are accessed over a local Ethernet network, and connects them to the user interface. The software layer also processes the sensor data to extract foot-floor contact points that are used for interaction, and provides them with unique IDs that persist while contact is sustained. Additionally, it allows to remotely cue and present localized vibrotactile feedback in response to activation or control of user interface objects on the floor. The protocol design is based, in part, on the TUIO protocol for table-top touch interfaces [169]. Figure 5.10 illustrates a virtual floor-based touch interface, consisting of sliders, buttons, toggle switches, and similar elements. The controls can be operated without consideration for the location of the tile boundaries, since we track interaction points continuously across tile boundaries. Normal force thresholds are used to determine when buttons or other controls are being engaged.

5.6.1 Preliminary User Evaluation

A question we encountered when beginning to design applications concerned the appropriate size and layout of virtual controls. The required size depends on factors including sensing limitations, users' motor abilities, target parameters, and feedback modalities, as has been extensively studied and modeled in the HCI literature [170, 171]. The size appropriate for touch screen controls has been shown to depend on the interaction technique adopted. Precision control strategies can enable single pixel accuracy in finger-based touch screen interaction [172, 173], and related techniques may prove effective for use with the feet. Limited research has addressed floor interfaces (Sec. 5.6), so we focused here on a basic task requiring the selection of controls presented at various locations and sizes to a stationary user.

Human movement research has investigated foot movement control in diverse settings. Visually guided targeting with the foot has been found to be effectively modeled by a similar version of Fitts' law as is employed for modeling hand movements, with an execution time about twice as long for a similar hand movement [174]. However, the present, preliminary, investigation addresses a situation in which usability is manifestly co-determined by both operator and device limitations, providing a window on both.

Apparatus The apparatus is the floor interface presented above. Due to the floor size, the sensor calibration was less accurate by a factor of two than that which yielded the position estimates noted above, but was sufficient for interaction points to be effectively tracked over extended distances on the floor.

Stimuli and method The stimuli consist of round virtual buttons to be selected by users, who began each trial with their feet in locations marked by white rectangles. Users could activate a button by pressing it in a way that resulted in a contact centroid within the area of the button exceeding a force threshold of about 35 N. The buttons ranged in diameter from 4.5 to 16.5 cm, and were presented at four distances, on lines radiating from between their feet, oriented at one of two angles, as shown in Fig. 5.11. Upon selection, the buttons provided visual feedback in the form of a 20 cm white disc centered in place of the original appearance. All buttons provided the same feedback. Only the buttons and foot locations were displayed. No audio or vibrotactile feedback was provided.

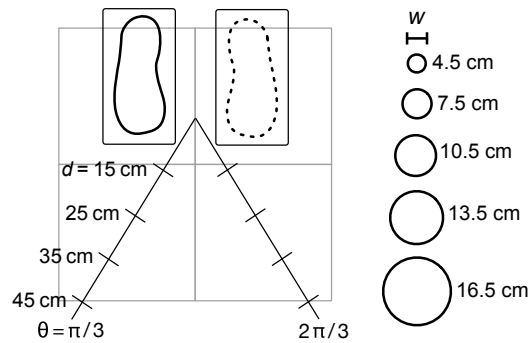


Fig. 5.11 Configuration and stimuli from the experiment. Participants selected targets of width w with their dominant foot (shown here as the right foot), at distances d and bearing angles θ .

Hypothesis We expected user performance to improve with target size and degrade with target distance. Interaction between target distance and width might be anticipated, but we do not attempt to validate a model. We expected good performance for targets that are at least as wide as the foot.

Participants Eight participants, ranging in age between 21 and 38, volunteered for this study. All of them were research staff or students in the Faculty of Engineering at McGill University.

Procedure Participants wore their own shoes during the experiment, and selected targets with their preferred, dominant foot. They were instructed to activate the buttons precisely and quickly. The non-preferred foot was not constrained, but participants were required to return both feet to the two rectangular regions shown in Fig. 5.11 between stimuli. Most chose to leave their non-preferred foot in place throughout each session.

The experiment began with a practice period lasting three minutes, followed by the main experiment. The latter consisted of two sessions of 12 minutes, with a short pause in between. A total of 240 stimuli were presented to each participant. Stimuli were presented in sequential, randomized order. Each button appeared and remained visible and active for two seconds during which users were able to select it. A three second pause followed, after which the next button appeared. The success of selection and time required were recorded. Participants completed a response questionnaire and provided verbal comments afterward.

Analysis Summaries of the success frequencies are presented in Figure 5.12. Using a logistic regression analysis, we determined that the main factors of width w , distance d , and bearing angle θ significantly affected success of selection ($p < 0.001$). The fitted logit is $z = 1.4 + 0.071w - 0.062d - 0.6\theta$ (with t -values > 7.8). θ is in radians, increasing away from the preferred foot; d and w are measured in cm. The model correctly predicts 86% of the responses.

Discussion Users selected larger targets within the allotted two-second interval at a higher rate of success than smaller ones. Performance with the largest was very high (98%), and that for the smallest was low (44%). Small targets pose two potential problems. First, they can be occluded by the foot during selection. This problem was somewhat mitigated because when this occurred, they were often visible projected on top of the foot. Second, limitations on precise control can arise from factors such as shoe width, human motor abilities, and sensor positioning errors. Six out of eight participants reported finding a strategy to activate the small buttons by using a feature of the shoe or changing the applied force. Software interaction techniques for improving precise touch screen control are known [172, 173], and we intend to investigate them in future work.

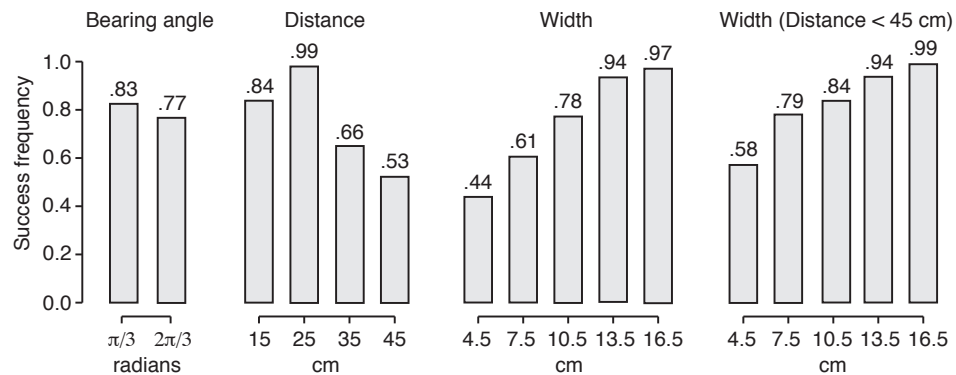


Fig. 5.12 Successful target selection rate vs. distance, angle of presentation (measured away from preferred foot), and button width, inclusive and exclusive of the farthest targets.

Nearby targets (distances of $D = 15$ to 25 cm) were selected at a higher rate. However, performance was better at 25 cm than at the nearest distance of 15 cm (98.5% vs. 84%, with $p < 0.001$ using Fisher's exact test, two-tailed). One apparent reason was that when an interface element was too close, it could be occluded from view by the body, or could

present a difficult viewing angle. Due to such effects we would not expect selection time T to follow a Fitts' Law relation, $T = a + b \log_2(D/W)$, but this was not tested here. Although a mobile user might be able to avoid visibility problems, they seem to be an important consideration. For our device, position sensing is most accurate near the centers of the tiles, as indicated in the preceding section. This was noticed by users of the system, two of whom volunteered that they had learned to better activate small buttons that were close to edges by pressing them off-center. In ongoing work, we are developing algorithms for correcting such positioning distortions. Participants consistently reported difficulty in selecting targets that were oriented away from their active, selecting foot, however the effect of bearing angle on performance was small (Fig. 5.12). It is possible that these responses were indicative of a larger motor effort. Neck fatigue was the most frequently cited source of discomfort.

Future work Although these results are suggestive, further work is needed in order to characterize the usability aspects of this display, and others like it. A greater understanding of factors such as control element size, display scale, motor abilities, modalities, and other aspects salient to the use of such a device will certainly be needed. In addition, we intend to investigate aspects of the usability of vibrotactile display to the feet in similar contexts, since it is, arguably, the most unique aspect of this interface.

Another notable question not addressed by this study concerns the interplay between users' movements on foot and their interactions with the touch surface. A novel aspect is that, implicitly, both feet are involved, due to requirements of movement and of maintaining balance. In everyday actions, like striking a soccer ball, weight is often shifted onto one foot, which specifies an anchored location, while the opposite is used to perform an action. Thus, floor interfaces that involve movement may share similarities to bimanual interaction in HCI, a connection we intend to explore in future work.

5.7 Conclusions

We described techniques for interaction with virtual ground material simulations and user interfaces via a distributed, multimodal floor interface. Such foot-floor contact information is not usually available through optical sensing channels such as motion capture. The methods are low in cost and complexity, and accessible to multiple users without body-

worn markers or equipment. In addition, this paper demonstrates the integration of these interaction techniques within multimodal displays implementing virtual ground surface simulations or floor-based control interfaces. Despite the promising nature of these results, there are several respects in which the present system might be improved or extended:

- Our system senses three DOF per tile (the normal force f_c and position \mathbf{x}_c). To solve the sensing problem required assuming frictionless contact (Sec. 5.4). A future interface for sensing the full six rigid DOF per tile (via additional sensors) would remove this assumption.
- A floor interface with a denser array of tiles would be capable of capturing more information about foot-ground contact shape.
- During multi-tile foot-floor contact, a contact-based sensing approach results in clusters of contact centroids. New techniques would be needed in order to extract more information related to the shape of a pressure or traction distribution from them.
- Interaction points can be followed only as long as foot-floor contact is sustained. It would be beneficial to be able to coherently track users' feet between gestures or actions.
- As noted more extensively in Sec. 5.6.1, above, further work is needed in many areas of usability in order to develop design guidelines and strategies for floor-based interfaces.

It is nonetheless hoped that this contribution succeeds in demonstrating some potential uses and design considerations for floor-based touch surfaces in virtual reality and human-computer interaction.

Chapter 6

Vibration Increases Haptic Perception of Surface Compliance

At the time of writing, this paper is accepted for publication in the journal *PLoS One*, with the title:

“Vibration Influences Haptic Perception of Surface Compliance During Walking”

Authors:

Yon Visell, Bruno Giordano, Guillaume Millet, and Jeremy Cooperstock

Copyright notice:

This material is reproduced here under a Creative Commons Attribution License. The authors retain ownership of the copyright of this article, and no permission of the authors or the publishers is required to reproduce, reprint, modify, distribute and/or copy this content, provided the original authors and source are cited.

Preface to Chapter 6:

This paper investigated the ability of a vibrotactile floor interface to simulate an important perceptual dimension of natural walking surfaces: their compliance. Although this is a mechanical attribute that is highly salient to the control of locomotion and to the feel of different ground surfaces, it would not seem to be appropriate for presentation via a vibrotactile display, which cannot directly reproduce kinesthetic force-displacement information. However, this study demonstrated a robust perceptual illusion in which plantar vibrotactile feedback increased the perceived compliance of a rigid floor surface. The effect size was primarily parametrized by vibration amplitude. The influence observed here appears to be distinct from known effects of plantar vibration feedback on posture. Instead, our findings appear to be consistent with the notion that vibration feedback provided a cue that tended to increase perceived displacement of the ground surface during stepping, similar, perhaps, to the way that vibrations are felt during compression of natural materials such as gravel or snow underfoot.

The results indicate that vibrotactile feedback supplied to the foot can be unexpectedly effective at reproducing the compliant feel of soft ground surfaces, and appear to indicate that vibrotactile sensory information plays a larger role than previously acknowledged in the sensorimotor loop associated with locomotion.

Contributions of Authors:

Yon Visell conceived and designed the experimental study, designed and calibrated the apparatus, and implemented and ran the experiments. He also contributed to the data analysis, prepared the figures, and wrote the manuscript. Bruno Giordano designed the experimental study, analyzed the data, and edited the manuscript. Guillaume Millet contributed to the design and implementation of the apparatus, ran the experiments, and edited the manuscript. Prof. Cooperstock supervised the research and edited the manuscript.

6.1 Abstract

Background: The haptic perception of ground compliance is used for stable regulation of dynamic posture and the control of locomotion in diverse natural environments. Although rarely investigated in relation to walking, vibrotactile sensory channels are known to be active in the discrimination of material properties of objects and surfaces through touch. This study investigated how the perception of ground surface compliance is altered by plantar vibration feedback.

Methodology/Principal findings: Subjects walked in shoes over a rigid floor plate that provided plantar vibration feedback, and responded indicating how compliant it felt, either in subjective magnitude or via pairwise comparisons. In one experiment, the compliance of the floor plate was also varied. Results showed that perceived compliance of the plate increased monotonically with vibration feedback intensity, and depended to a lesser extent on the temporal or frequency distribution of the feedback. When both plate stiffness (inverse compliance) and vibration amplitude were manipulated, the effect persisted, with both factors contributing to compliance perception. A significant influence of vibration was observed even for amplitudes close to psychophysical detection thresholds.

Conclusions/Significance: These findings reveal that vibrotactile sensory channels are highly salient to the perception of surface compliance, and suggest that correlations between vibrotactile sensory information and motor activity may be of broader significance for the control of human locomotion than has been previously acknowledged.

6.2 Introduction

The goal of this study is to measure empirically the role played by vibrotactile sensory information in the perception of ground surfaces during walking. To this end, we focused on a basic property of walking surfaces that is highly salient to locomotion—their mechanical compliance [27, 32]. We investigated what influence, if any, vibration feedback to the plantar soles may have on the perception of ground surface compliance during walking.

The perception of ground surfaces is instrumental to enabling us to move easily on foot in diverse natural environments. Human locomotor movements are adapted when stepping onto, off of, or moving over soft, irregular, or slippery surfaces in ways that minimize metabolic costs, reduce impact forces, or stabilize vertical center of mass [26, 27, 28, 29, 30, 31, 32]. Compliant ground surfaces, such as sand or soggy grass, perturb locomotion by degrading proprioceptive cues that are acquired via ground contact and by mechanical perturbations due to the compression of material underfoot. Walkers automatically modulate their gait pattern and biomechanics to compensate for such changes in compliance [32].

When haptic sensation in the feet is impaired, as a result of a disease such as diabetes, or through local anesthesia, it can have detrimental effects on locomotion [175, 176, 177, 178]. However, knowledge about the influence of different sources of haptic sensory information, such as plantar force or vibromechanical stimuli, on the control of walking is incomplete.

Haptic compliance perception involves discerning the deformability of objects touched with the hand, or of surfaces felt underfoot. Compliance, the inverse of stiffness, is the ratio between displacement and applied force, $C = \Delta x / \Delta F$, and is related to the intrinsic material property of elasticity. Most prior research has investigated compliance perception via manual touch [179, 180, 181, 182, 183, 184, 185, 186], but the haptic perceptual system is also able to discriminate walking surfaces of different elasticity [38, 33]. Sensitivity is highest when there is direct contact between the surface of the skin and a deformable object. In this setting, cutaneous tactile cues predominate [184]. Conversely, when touch is mediated by a rigid link, such as a stick or a stiff shoe sole, cutaneous force cues are combined with proprioceptive information to form compliance estimates [183, 182, 186, 187]. If cutaneous information is blocked entirely, performance is greatly degraded [183].

While we are not aware of any prior investigation of effects of vibrotactile sensory information on compliance perception, it is well established that high-frequency mechanical vibrations generated during interaction with surfaces via manually tapping or scraping with a probe, or scanning with a finger, can influence the perception of properties such as hardness and texture [42, 43, 44, 45, 46, 47]. For example, amplifying vibrations generated during manual surface scanning, or imposing sinusoidal vibrations, increases perceived surface roughness [50]. Vibrations produced during frictional sliding are indicative of movement [188], and could contribute to compliance perception. On this basis, it could be hypothesized that an amplification of plantar vibration intensity would lead to an increase in the

magnitude of compliance estimates, because displacement and compliance are proportional.

Mechanical signals generated during walking on natural ground surfaces constitute a rich source of haptic sensory information [4, 2, 37]. The compression of many heterogeneous materials (e.g., wood, snow, gravel) results in inelastic, unrecoverable deformations with energy distributed over a broad frequency band [4]. The pattern of these vibrations is highly correlated with material displacement [10, 11], so it is natural to consider them as potential displacement cues. Giordano et al. found that walkers are able to distinguish between the feel of porous and solid ground surfaces, or rock gravel surfaces of different grades, when walking in shoes [189]. When plantar cutaneous input was masked by mechanical vibrations, in the form of synthesized pseudo-random noise (frequency distribution: 50 Hz to 1 kHz), performance was impaired, suggesting that vibrotaction played a significant role.¹

Relatively few studies have investigated haptic perception with the feet. However, the foot is serially homologous to the hand, and is highly evolved as a sensory instrument. Its perceptual-motor abilities are involved in the regulation of posture and locomotion [190], and in the estimation of ground slipperiness and slant [25, 191, 192]. The sensory physiology of the plantar sole is highly developed, with the same type of mechanoreceptor populations as are present in the hand: the fast-adapting (FA) type I and II and slow-adapting (SA) type I and II receptors [17, 18]. The sole is highly sensitive to vibration, with FA receptors comprising about 70% of the cutaneous population. Low-frequency forces are sensed by SA receptors [17], and by Golgi organs, muscle spindles, and joint capsule receptors in the muscles, tendons, and joints.

Vibromechanical stimulation of the plantar sole affects both cutaneous receptors and deeper foot and ankle proprioceptors. Such stimuli can result in real or illusory postural effects resembling those due to an increase in local pressure at the same location of the foot sole [193, 194, 195, 196]. This could be taken to suggest that amplifying plantar vibration may, by increasing perceived forces, decrease ground compliance estimates—contrary to what is suggested by foot-ground mechanical considerations. However, studies of this type have generally been conducted while subjects stood in place, whereas haptic compliance perception always requires movement. In other experiments on vibration stimulation of the leg muscles or tendons, different effects have been observed to accompany stimulation

¹Further analysis is provided in: Giordano B, Visell Y, Cooperstock JR, Yao HY, Hayward V, and McAdams S (2010) Audiohaptic identification of ground materials during walking (Submitted).

provided during stance than those induced when it is provided during locomotion. In the former case, it induces whole-body postural tilts (attributed to illusory lengthening of the stimulated muscles), whereas during locomotion it results in modified stepping movements with little overall change in muscle coordination [197, 198, 199]. Courtine et al. argued that this reflects the fact that sensory inflow is processed depending on both the body segment where it arises and the performed task [198]. As a result, we questioned whether prior results on postural effects of plantar vibration would apply in our study, in which subjects were actively moving.

Our experiments evaluated the influence of vibrotactile information felt during stepping onto a floor surface on the perceived compliance of the latter. The above-referenced studies involved a diverse range of signal types (noise-like or natural textures, and sinusoidal stimuli), amplitudes, and temporal dependencies. Experiment 1 was designed to investigate effects of vibration feedback on perceived compliance, and to clarify their dependency on time- and frequency-domain stimulus properties. To further determine the extent to which vibrotactile sensory information is combined with cutaneous force and proprioceptive information in the perception of ground compliance, Experiment 2 measured the effect of plantar vibration on compliance perception via a novel apparatus that allowed both the mechanical stiffness of a floor plate and vibration feedback presented through it to be manipulated. Psychophysical amplitude detection thresholds for the stimuli were also measured in order to provide an indication of the relative intensity of the stimuli.

6.3 Materials and Methods

6.3.1 Ethics Statement

The experiments were conducted in accordance with McGill University ethics guidelines, and was reviewed and approved by the McGill Research Ethics Board in accordance with the requirements of the McGill University Policy on Ethical Conduct of Research involving Human Subjects and with the Tri-Council Policy Statement: Ethical Conduct For Research Involving Humans.

6.3.2 General Methods

During the experiments, subjects crossed a short walkway incorporating an actuated floor plate that provided vibration feedback in response to forces exerted by the foot. The mechanical stiffness of the plate was manipulated in Experiment 2.

6.3.3 Apparatus

The apparatus consisted of a short walking platform (Fig. 6.1) permitting subjects to take a single step onto a vibration-actuated floor plate. The plate was actuated by a Lorentz force inertial motor (Clark Synthesis model TST429) rigidly coupled to it from beneath. This plate was used to present walkers with vibration feedback and to present a specified mechanical stiffness to the walker, via a servo controlled mechanism (see Experiment 2).

To ensure that vibromechanical stimuli could be reproduced accurately across a wide range of frequencies, while assuring the stability of the plate under a human walker, we undertook an extensive redesign of our earlier apparatus [152], as fully described in reference [200]. Through measurements, we determined that the device was able to reproduce arbitrary vibrations accurately at forces of more than 40 N within a flat frequency band from 50 to 750 Hz. Within the range of amplitudes used here, vibrations could be presented with a nonlinear waveform distortion of less than 3% (mean absolute percent error, measured at 300 Hz). The device could sense static or transient loads of more than 1000 N supplied by a human foot. Analog data from the force sensors were conditioned, amplified, and digitized via a 16-bit acquisition card (National Instruments model USB-6218). Digital-to-analog conversion of the vibration signal was performed using a 24-bit, 48 kHz audio interface (Edirol model FA-101). The analog signal was then passed through a power amplifier driving the actuator. In order to assess the accurate reproduction of the vibration stimuli, they were independently recorded with a miniature accelerometer permanently attached to the underside of the plate.

6.3.4 General Procedure

During the experiments, stimuli were presented via the plate as subjects stepped on it. They began on one side of the walkway (see Fig. 6.1), stepped onto the plate with their dominant foot, and proceeded to the opposite side, turned, stepped on the plate again using their dominant foot, returned to the first side, and entered their responses via a computer

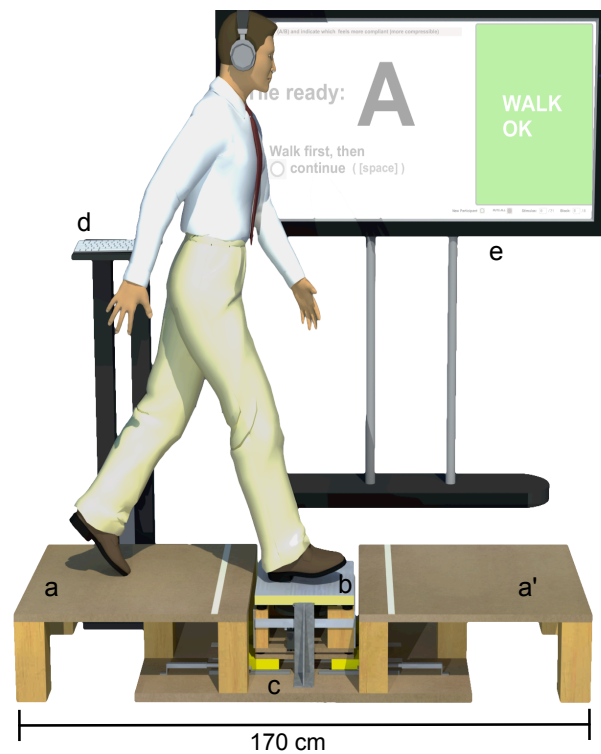


Fig. 6.1 Apparatus for producing compliance and vibration stimuli.

Subjects stepped from one side of the platform *a* onto the vibrating plate *b*, and onto the opposite platform *a'*. They then turned, stepped on *b* again, and returned to *a*. In Experiment 2, the plate also displaced up to 2 cm in the vertical direction, compressing a volume of EVA foam that was controlled by the linear servomechanism *c*, to produce the commanded compliance (see Fig. 6.3). Subjects entered their responses after each trial at the keyboard *d* and received instructions from the large-screen video monitor *e*.

terminal. Before each experiment, subjects were instructed in the use of the apparatus and interface.

Both experiments took place in a structurally isolated, soundproofed room with a noise-floor rating of PNC20. Subjects wore foam earplugs with an NRR attenuation rating of 33 dB and wireless headphones playing pink noise at a volume sufficient to mask any sounds produced by the vibrating plate and the motors. The non-vibrating walking platforms were isolated from the actuators via cushioning material, eliminating the transmission of vibrations to users before stimulus presentation.

A steady walking pace was enforced via a 1 Hz metronome sound audible above the

pink noise. The experiments were conducted at low light levels to allow subjects to focus on what they felt, but sufficient for the walkway to remain visible. However, subjects were asked to avoid looking down at the plate while walking on it, unless necessary to maintain equilibrium, and instead, were instructed to attend to one of the two static visual markers that were positioned at a height of 1.3 m (above foot level), and a distance 1 m from either end of the walkway.

Subjects were required to wear shoes in the experiment in order to avoid directing their attention to the surface properties of the plate. In order to standardize footwear in all experiments, only male subjects were recruited, with North American shoe size between 7 and 12. Each was given an identical model men’s hard soled dress shoe in the appropriate size to wear. All subjects reported normal tactile sensation in the feet, with normal walking ability, and were naive with respect to the purpose of the study. They were presented with and signed informed consent forms at the beginning of the experiment and were paid ten dollars (CAD) per hour for their participation upon completion.

6.3.5 Experiment 1

Experiment 1 was based on ratings of subjective compliance. We investigated the perceived compliance of a rigid plate augmented with nine different types of vibration feedback at two amplitude levels, as well as one condition in which no vibration feedback was provided. Subjects walked across each configuration of the plate, and rated its compliance on a continuous scale.

Recruitment Twenty people participated in the experiment (mean age 24.5 years, STD = 6.9 years, average mass 70.9 kg, STD = 11.2 kg). None participated in any other study on compliance or vibration perception. Other details were as described under “General Methods”.

Stimuli The stimuli consisted of several different types of vibration feedback and one no-vibration reference condition. The stiffness of the plate was held constant, and was set equal to 90 N/mm, the median stiffness value used in Experiment 2. The 18 vibration stimuli were generated by factorial combination of three parameters: amplitude scale A (0.5, 1.0), temporal waveform type $w(t)$ (Sinusoidal, White Noise, Textured Noise), and amplitude envelope $e(t)$ (Constant, Force-Proportional, Dynamic). Each stimulus can be described as

an acceleration signal delivered from the plate, having the form $s(t) = GAe(t)w(t)$, where G were stimulus-dependent peak gain factors.

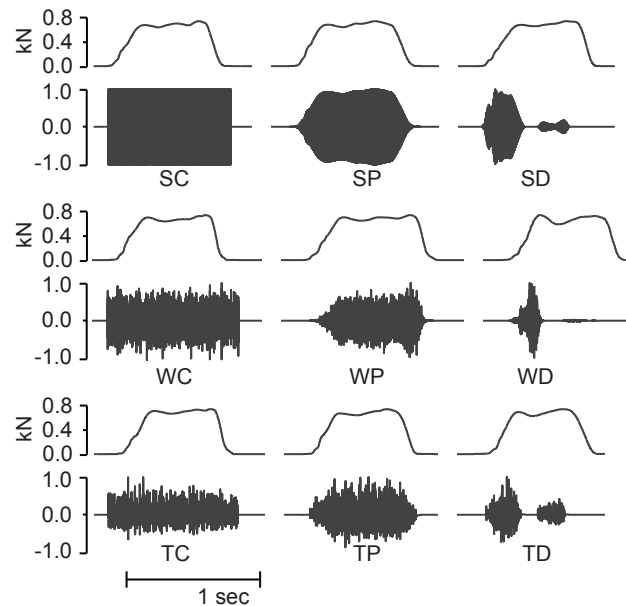


Fig. 6.2 Vibration feedback stimuli. The thin lines (rows 1, 3, and 5) show force profiles from footsteps of one participant onto the plate, and the darker waveforms are the corresponding vibration feedback stimuli. Vibrations could be felt only during foot-plate contact. Stimuli are labeled with a 2-letter string, with the first encoding waveform type (S, W, T = Sinusoidal, White noise, Textured noise), and the second encoding envelope type (C, P, D = Constant, Proportional, Dynamic). The vibration amplitude range was normalized for display purposes.

The vibration signals for the nine stimuli resulting from combining the factors “amplitude envelope” and “waveform type” are shown in Fig. 6.2. Three different waveforms $w(t)$ were used. The first was a sinusoid $w(t) = \sin(2\pi ft)$ with frequency $f = 300$ Hz. The second was a white noise that was band-limited by filtering to remove frequencies above 700 Hz and below 50 Hz. The third was a noise signal intended to resemble the texture felt when a porous material, such as gravel, is compressed. It was obtained by passing an impulsive noise source, consisting of a random impulse train, through a resonant filter. The impulses were identical in amplitude scale, and occurred at times t_i whose time intervals $\Delta t_i = t_i - t_{i-1}$ were sampled from a Poisson stochastic process; the intervals were distributed as $P(\Delta t_i) = \lambda \Delta t_i \exp(-\lambda \Delta t_i)$. The mean event frequency was $\lambda = 0.05$ events/ms. Each impulse was rendered as a 1 ms white noise burst beginning at

t_i . The impulse train was passed through a second-order infinite impulse response (IIR) bandpass filter with center frequency $f_c = 300$ Hz and bandwidth 15 Hz. The resulting noise had a rough texture with most energy concentrated in a narrow frequency band at which FA type II mechanoreceptors in the foot sole are most sensitive.

The three different envelopes $e(t)$ specified the amplitude profile of the vibration feedback in response to a footstep with normal force profile $F(t)$. The first was a constant function $e(t) = 1$, and the second was a linear force-proportional envelope $e(t) = F(t)/F_0$, with inverse slope $F_0 = 750$ N. The third was a dynamic envelope $e(t) = \dot{x}(t)$ derived from an admittance-based simulation of a linear, compressible material, where $\dot{x}(t)$ is the time-derivative of the virtual strain $x(t)$ response to $F(t)$, described by

$$\frac{1}{M}F(t) = \ddot{x}(t) + 2\zeta\omega_0\dot{x}(t) + \omega_0^2(x(t) - x_0) \quad (6.1)$$

The envelope $e(t) = \dot{x}(t)$ is obtained in real time as the output of a second-order digital IIR bandpass filter computed by solving (6.1) using the Laplace transform method and the bilinear transform [85, 201]. The filter input was $F(t)/M$ and the output was $\dot{x}(t)$. M could be taken as the mass of a representative volume element, but here it is an arbitrary gain factor. We used frequency $f_0 = \omega_0/(2\pi) = 12.5$ Hz, and set $\zeta = 1$ for critical damping. This yielded a characteristic envelope response time of $\tau = 80$ ms.

As explained in reference [200], the combination of the dynamic envelope type with the textured noise waveform (i.e., stimulus TD) can be regarded as a simplified micromechanical model for the production of textured vibrations during the compression of a natural, heterogeneous material such as gravel, sand, or snow.

Stimulus intensity equalization In a pilot study, we observed that the vibration feedback stimuli could significantly increase subjective compliance ratings, and that the effect depended primarily on the stimulus amplitude parameter. However, RMS signal energy and subjective stimulus intensity depended on amplitude, waveform, and envelope type parameters. To ensure that the latter two could be manipulated independently of amplitude, a separate procedure was used, prior to the main part of Experiment 1, to equalize the stimuli with respect to the subjective intensity of vibration. Ten subjects that did not participate in the main experiment were recruited for this equalization experiment (mean age 23.1 years, STD = 6.1 years, average mass 71.1 kg, STD = 10.4 kg), which was based on a two

interval forced choice adaptive staircase method. On each trial, subjects walked across two configurations of the plate differing in vibration feedback type and amplitude and reported whether the first or second vibration felt stronger. The order of the two stimuli was random from trial to trial. One of the two, the standard, was always the high-amplitude white noise stimulus (WC1). The other, the comparison, was one of the remaining eight stimulus types parametrized by waveform and envelope (type SC, SP, SD, WP, WD, TC, TP, or TD). The amplitude of the comparison was controlled by a staircase method that tracked the point of subjective equality, i.e., the amplification factor for the comparison stimulus that rendered it as intense as the standard. If the subject indicated that the comparison felt stronger (respectively weaker), then its amplitude was reduced (respectively increased) by one step unit. The step size was initially large (10 dB) and became smaller (3 dB) after two reversals in the direction of the threshold-tracking sequence. Each staircase was run for 12 reversals, and the point of subjective intensity equivalence was calculated as the average between the last 8 reversals. A total of 16 staircases (8 interleaved pairs) were completed by each subject. Other details were as described under “General Procedure”.

The results of this procedure were used to assign the values of the gain G of the Experiment 1 stimuli. The stimuli were regarded as equal in subjective intensity, within limitations determined by experiment duration and inter-subject variability. Table 6.1 reports the measured peak and RMS gain values for the equalized stimuli, which are labeled with a two-letter string, with the first encoding waveform (S, W, T = Sinusoidal, White noise, Textured noise), the second encoding envelope (C, P, D = Constant, Proportional, Dynamic). Values are reported for the high-amplitude ($A = 1.0$) stimuli. Both experiments also included stimuli with $A = 0.5$. Amplitudes were verified by accelerometer measurement while the plate was loaded by a footstep. For the noise stimuli (W and T), since the absolute peak could vary between presentations, a stable measure was obtained as the median of peak amplitudes on a set of 10 ms windows spanning the highest amplitude interval.

Procedure For each stimulus presentation during the experiment, subjects walked across the plate and rated its compliance using a slider labeled “most compliant” and “least compliant” at the two extremes. Subjects were informed that they might, at times, feel vibrations via their feet, but no further elaboration was given. The first experimental block was a warm-up period in which subjects tried all configurations of the plate that would be

Table 6.1 Experiments 1 and 2: Peak and RMS amplitudes of plate acceleration, G for the high amplitude $A = 1.0$ vibration stimuli.
Stimulus labels: S, W, T = Sinusoidal, White noise, Textured noise waveform;
C, P, D = Constant, Proportional, Dynamic envelope.

		SC	SP	SD	WC	WP	WD	TC	TP	TD
Exp. 1	Peak (m/s^2)	2.9	3.7	6.8	17.4	18.4	18.2	3.3	4.6	6.8
	RMS (m/s^2)	1.74	2.4	4.4	10.9	8.5	10.9	1.2	1.75	2.4
Exp. 2	Peak (m/s^2)									0.86
	RMS (m/s^2)									0.29

presented. In this period, they were instructed to focus on the maximum and minimum compliance within the stimulus set. During the remainder of the experiment, subjects were asked to use the entire range of the slider when rating the stimuli. The 18 equalized stimuli were presented in blocked randomized order, each stimulus being presented once on each of 12 blocks, for a total of 216 trials. The resulting data consisted of twelve compliance ratings per stimulus from each subject. The entire experiment lasted 90 minutes. There was a pause of two minutes between blocks, and a pause of five minutes after the sixth block. Additionally, there was a pause of at least five seconds between stimuli, as subjects entered their responses. Other details were as described under “General Procedure”.

6.3.6 Experiment 2

The experiment investigated the extent to which vibration feedback modified perception of the compliance of the floor plate when both vibration amplitude and plate stiffness were manipulated. The resulting data consisted of the proportion of responses in which the comparison was judged more compliant, for each stiffness and amplitude level.

Recruitment Twenty new subjects participated in the experiment (mean age 23.1 years, $\text{STD} = 4.1$ years, average mass 69.8 kg, $\text{STD} = 11.2$ kg). Other details were as described under “General Methods”.

Apparatus The plate was integrated with a novel mechanism that allowed it to displace vertically with low friction, and that allowed us to vary the mechanical stiffness of the plate

precisely for each stimulus within a range from 40 to 160 N/mm. An automated servomechanism was used to change the amount of surface area of a pair of highly recoverable, 3 cm thick foam pads inserted beneath the plate (Fig. 6.3).

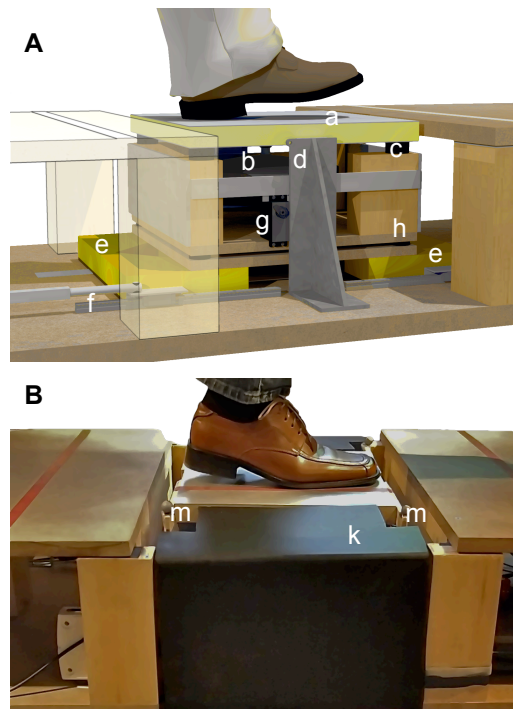


Fig. 6.3 View of the variable compliance mechanism. A. Users stepped onto vibrating plate *a*, which was driven by vibration actuator *b* and mounted on suspension *c*. The plate displaced in the vertical direction, guided by low-noise ball bearing slides *d*, and compressing a pair of foam inserts *e*. To produce the commanded compliance, the foam inserts *e* were positioned by the linear servomechanisms *f* before each stimulus presentation, while the plate assembly was lifted by servos *g*. Participant-applied forces were measured by load cells *h* under four corners of the plate assembly. B. Image of the apparatus and shoe as used in the experiment. Opaque panels *k* and fabric (not shown) hid the device configuration from subjects' view. Four optical motion capture markers *m* tracked the displacement of the plate with high precision.

A calibration procedure made it possible to specify plate stiffness, in values of N/mm, via computer control of foam position, with a mean accuracy of about 1%. Force measurements from the load cells in the apparatus were combined with position measurements from a precise motion capture system (OptiTrack, Model FLEX:V100R2). Calibration was per-

formed using least squares regression fit of force to 60 force-displacement profiles consisting of more than 3000 measurements each (Fig. 6.4). As illustrated, the force-displacement relationship was approximately linear. Measurements from each force-displacement profile were acquired by loading the plate with a typical footstep, since, due to the finite recovery time of the foam pad, the measured stiffness could depend on the temporal profile of the load.

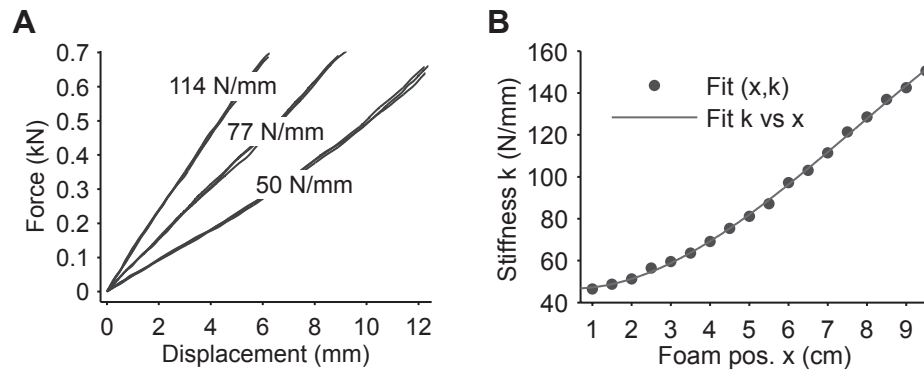


Fig. 6.4 Force-displacement profiles and fits of stiffness vs. foam position used to calibrate the apparatus. A. Examples of three compression profiles are shown (overlaid) for each of three stiffness values. Each calibration was based on sixty such profiles, with more than 3000 data points each. B. Calibration curve fit of stiffness vs. foam position based on measurements at each position and stiffness.

To ensure that the presented stiffness remained accurate, the calibration process was repeated four times in the course of the experiment, between experimental sessions. The minimum stiffness was 52 N/mm, corresponding to an absolute maximum displacement of approximately 2 cm when a subject walked across it with a maximum downward force of about 1000 N. We avoided using softer settings, as we found that it could otherwise become difficult for subjects to step normally and stably across the plate without the need to look down, which was discouraged (see “General Procedure”). The maximum stiffness was 146 N/mm, which was close to the highest level that could be well controlled. At stiffer settings, the intrinsic compliance of the vibration mounts (location b in Fig. 6.3) would have a non-negligible influence on the plate compliance in ways that depended on foot location and orientation. In addition, stiffness discrimination underfoot would likely have become less reliable [33].

All motorized movements resulting from compliance changes were performed smoothly

to minimize any vibrations due to the mechanism that might otherwise provide information about the foam configuration. For the same reason, the duration of any mechanical reconfiguration was kept constant ($t = 4$ s).

Stimuli Stimuli were configurations of the floor plate with one of seven different stiffness levels (52, 64, 76, 90, 106, 124 or 146 N/mm) and one of three vibration feedback conditions. The vibrations were the textured, dynamic type (TD). Two different non-zero vibration amplitudes were used, respectively 18 dB and 24 dB lower than the high amplitude ($A = 1.0$) TD stimuli from Experiment 1, as well as a no-vibration condition. These lower amplitudes were selected through pre-testing to ensure that the resulting psychophysical data would be useful. Higher amplitudes tended to saturate the psychometric curves, dominating the effect of mechanical stiffness. Although Experiment 1 demonstrated that all vibration stimuli could increase perceived compliance, the TD type was selected for further testing because, among those with the highest mean compliance ratings (within one standard error of the mean), they had the shortest duration and one of the lowest RMS amplitudes, limiting the possibility of sensory adaptation during vibration stimulus presentation. The seven stiffnesses and three vibration levels resulted in 21 different comparison stimuli.

Procedure The experiment was based on the psychophysical method of constant stimuli, using a two interval forced choice paradigm. Subjects walked across pairs of configurations, one after the other, and responded to the question “Which one was more compliant (softer, more compressible)?”. Vibration was added to the comparison stimulus, except in the “no-vibration” condition, and was never added to the standard. The resulting data consisted of the proportion of responses in which each comparison configuration (that is, stiffness and vibration level) was judged more compliant.

The standard and comparison were presented, as in Experiment 1, in sequential randomized order. Because stiffness was manipulated in the experiment, subjects were required to pause for five seconds between each half of a stimulus pair, in order to provide enough time for the stiffness modification to complete. They were automatically cued to pause and to continue by the software graphical user interface. The timing of this pause was always the same, to avoid giving any indication of the amount of change in compliance. Other details were as described under “General Procedure”.

Subjects were told that during the main experiment they would be asked to respond indicating which of the two configurations felt more compliant. They were told that they might, at times, feel vibrations via their feet, but no further elaboration was given. The first experimental block was a warm-up period in which subjects tried six randomly generated stimulus pairs, consisting of random stiffnesses in the range used in the experiment, and vibration feedback of type WC, with a similar intensity to that used in the main experiment, although the type was different.

During the main experiment, all stimulus pairs were presented in each block, in randomized, balanced order. Randomization of stimulus order was independent for each session and each subject, and no blocks were repeated. Subjects were required to leave the apparatus and pause for one minute between blocks, and for four minutes after each third block. They each completed three experimental sessions, comprising a total of twenty blocks. The duration of the first two sessions was 90 minutes and that of the last session was 1 hour. No more than two experimental sessions, separated by at least two hours, were permitted for any subject on a single day. Each subject was presented with each of the 21 pairs a total of 20 times.

Subjects completed a post-experiment questionnaire and interview, which asked whether the vibrations were felt, and what decision strategy was used (see Results).

Psychophysical detection thresholds for the stimuli Immediately after subjects completed the questionnaire, they participated in a final stage of this experiment, which measured their psychophysical detection thresholds for amplitude. The stimuli consisted of individual configurations of plates, set to the median stiffness level of 90 N/mm, accompanied by vibration feedback of type TD, as used in the main experiment. Amplitude was manipulated independently during the procedure.

The threshold-measurement procedure was based on a single-interval adaptive yes/no staircase method developed by Lecluyse and Meddis for auditory threshold testing [202]. They found, through experiments and simulations, that this procedure yielded similar thresholds to those obtained with two-interval forced choice or maximum likelihood methods, resulted in less variation, and required fewer trials. The latter was a consideration in our experiment, because of the required level of activity and duration, which could lead to fatigue.

Stimuli were presented one at a time, and amplitude was controlled by the staircase pro-

cedure. Subjects responded after each presentation indicating whether they felt a vibration from the plate or not. They were instructed to be as sensitive as possible without guessing. When they responded “yes” (resp. “no”), then the amplitude was reduced (resp. increased) by one step unit. The step size was initially large (10 dB) and was reduced to a smaller level (3 dB) after two reversals in direction of the threshold-tracking sequence. For each comparison, one staircase was started at a high amplitude randomly chosen between +8 dB and +15 dB (referenced to the Experiment 2 stimulus amplitude of 0.43 m/s^2) and one at a low amplitude between -8 dB and -15 dB. The two staircases were interleaved, with one of the two randomly selected for presentation on each trial. In order to prevent guessing, 13% of the trials were randomly selected as catch trials, in which no vibration was present. Subjects were warned that if they answered “yes” on a catch trial, both staircases would be re-started. The median number of times that subjects were caught guessing in the experiment was 1.5 (minimum zero, maximum three). In addition, on every 10th trial, subjects were presented with a no-vibration stimulus and were told that no vibration was present, to remind them how that condition felt.

Each staircase was continued until 12 reversals were reached. A total of six staircases (three interleaved pairs) were completed by each subject, and the threshold was calculated as the average between the last eight reversals from all six staircases. Subjects were required to pause for 2 minutes between staircase pairs. The total duration for each subject was approximately 30 minutes.

6.4 Results

6.4.1 Vibration Stimulus Factors Influencing Subjective Compliance

Judgements

Data from Experiment 1 were analyzed to determine the effect of vibration feedback type on compliance ratings. Mean ratings for all the 19 stimuli are shown in Figure 6.5. Paired t-tests showed that all 18 vibrating stimuli were perceived as significantly more compliant than the non-vibrating one ($t(19) \geq 7.04$, $p < 0.001$).

We further analyzed compliance ratings in Experiment 1 with a within-subject repeated measures ANOVA, with amplitude, envelope, and waveform as factors. Mean compliance ratings for the values of each factor are shown in Fig. 6.6. The one-way effect of amplitude

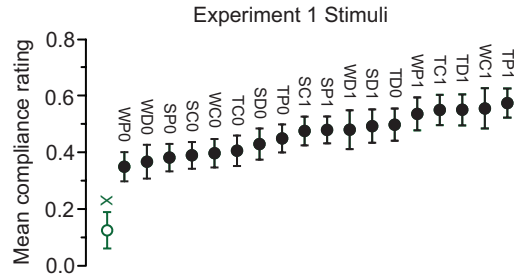


Fig. 6.5 Experiment 1: Subjective compliance ratings for all 19 stimuli, averaged across subjects. A higher value means more compliant (less stiff). “X” labels the no-vibration stimulus. Others are labeled with a 3-letter string encoding waveform, envelope, and amplitude level (0, 1 = Linear amplitude 0.5, 1.0). Error bars = ± 1 standard error of the mean (SEM). All vibrating stimuli were significantly more compliant than the no-vibration stimulus.

was significant ($p < 0.001$, $F(2, 19) > 33.0$, $\eta_p^2 \geq 0.635$), as was that of waveform ($p \leq 0.01$, $F(2, 19) > 5.24$, $\eta_p^2 \geq 0.216$), but the effect of envelope type was not significant ($F(2, 19) \leq 0.057$, $p \leq 0.02$, $\eta_p^2 \leq 0.003$). There were significant effects of all two-way interactions, amplitude \times waveform ($p < 0.001$, $F > 11.5$, $\eta_p^2 \geq 0.378$), amplitude \times envelope ($p \leq 0.013$, $F > 5.8$, $\eta_p^2 \geq 0.235$), and waveform \times envelope ($p < 0.001$, $F > 9.273$, $\eta_p^2 \geq 0.328$). There was no significant three-way effect ($p > 0.07$, $F < 2.3$, $\eta_p^2 \leq 0.106$). Based on this analysis, amplitude had the largest influence on compliance judgments, while the effects of waveform and of all two-way interactions were smaller.

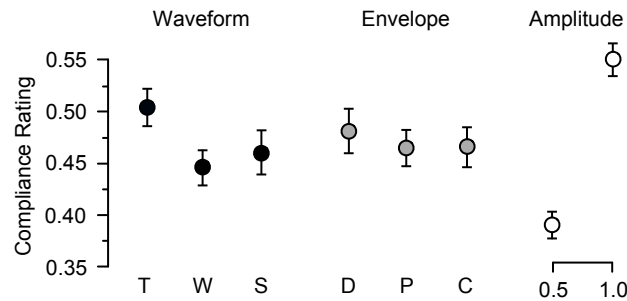


Fig. 6.6 Experiment 1: Average compliance ratings for the three stimulus factors “waveform type”, “envelope type”, and “amplitude”. Stimulus labels are as given in Fig. 6.5. Error bars: ± 1 SEM.

6.4.2 Effect of Vibration Feedback on Compliance Perception

The results of Experiment 2 consisted of proportions of responses at which the standard stimulus, a non-vibrating plate with stiffness 90 N/mm, was judged less stiff than a comparison that varied in stiffness and in vibration amplitude. Figure 6.7 presents the average response proportions. A one-way ANOVA of the response proportions for the factor *amplitude* indicated that vibration significantly decreased stiffness at each stiffness level (see Table 6.2). Although the variation in responses was larger at higher stiffnesses, the effect of amplitude on subjective compliance was proportionally larger, yielding a higher level of significance. For all subjects, average response proportions at the largest amplitude level (0.86 m/s²) were higher than in the no-vibration case.

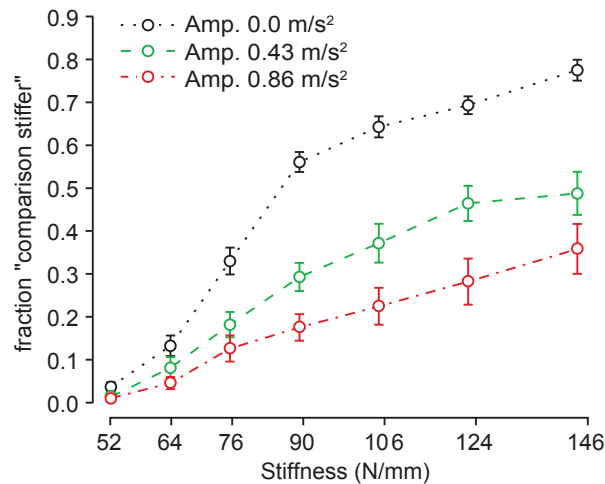


Fig. 6.7 Experiment 2: Mean proportion of comparison stimuli judged stiffer than the standard for each stiffness (units: N/mm) and amplitude level (units: m/s²). A higher proportion implies a judgment of “stiffer”. The standard had a stiffness of 90 N/mm, as indicated by the dashed line, and did not present any vibration feedback. Results shown are averaged between all 20 subjects. Error bars: ± 1 SEM.

Binary response data at each vibration amplitude level from each of the 20 subjects were fitted to a cumulative normal distribution using a probit regression model. A total of 60 fits were performed (three fits per subject, one at each vibration amplitude level). The models explain 86.5% of the variance in the data with Pearson correlation $\rho = 0.93$. The slope, intercept, and point of subjective equivalence (PSE) in stiffness were computed from each fit. Median values in each condition are shown in Figure 6.8 and given in Table 6.3. We

Table 6.2 Experiment 2: Mean proportions of comparison stimuli that were judged to be stiffer than the standard, as a function of stiffness, with different levels of vibration.

Stiffness	Response Proportion at Amp. A			one-way ANOVA	
	0.0 m/s ²	0.43 m/s ²	0.86 m/s ²	$F(2, 57)$	p
52 N/mm	0.034	0.010	0.0068	4.3	0.018
64 —	0.13	0.078	0.042	4.24	0.019
76 —	0.33	0.18	0.13	12.5	$< 10^{-4}$
90 —	0.557	0.29	0.17	50.3	$< 10^{-12}$
106 —	0.64	0.37	0.22	31.6	$< 10^{-9}$
124 —	0.69	0.46	0.28	26.9	$< 10^{-8}$
146 —	0.77	0.49	0.36	22.0	$< 10^{-7}$

investigated influences of vibration amplitude on the fit parameters using a nonparametric Friedman test, in order to ensure that the analysis would remain robust to outliers in the data. The latter resulted from a few subjects whose response proportions increased slowly with stiffness in the high-amplitude condition, leading to unusually small slope values, and large PSEs. Vibration amplitude did not significantly affect intercept ($\chi^2(2) = 3.9$, $p > 0.14$), indicating that subjects were not biased to indiscriminately answer “softer” when vibration amplitude was higher. PSE increased significantly with amplitude ($\chi^2(2) = 34.9$, $p < 10^{-7}$), indicating that the stimulus was perceived as softer when vibration was present, and slope also increased ($\chi^2(2) = 17.2$, $p < 0.0002$), indicating that stiffness discrimination performance was impaired in the presence of vibration. Nonparametric repeated-measures tests contrasting all three amplitude levels indicated no significant effect on intercept ($p > 0.3$, Bonferroni corrected, BC), but did reveal an effect of amplitude on PSE for all pairings ($p < 0.01$, BC). There was a significant effect on slope between the no-vibration and either high- or low-amplitude conditions ($p < 0.035$, BC), but not between the low- and high-amplitude vibration conditions ($p > 0.34$, BC). Increasing the vibration amplitude level from low to high thus increased the bias in the PSE for stiffness estimation without further decreasing discriminability.

Experiment 2 also measured psychophysical amplitude thresholds for detection of the vibration stimuli, for the same subject pool used in the main part of the experiment, with the plate stiffness set to the median value of 90 N/mm. These thresholds were measured

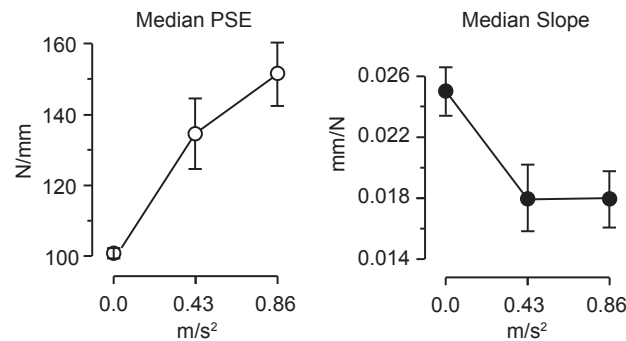


Fig. 6.8 Experiment 2: Median values of the PSE and slope from per-subject psychometric fits at each vibration amplitude level. Error bars: ± 1 SEM (outliers excluded).

in shoes, and would likely be lower if direct skin contact were involved. The measurements were based on a fast, single interval yes-no procedure with catch trials [202]. Although Lecluyse and Meddis found this method to yield similar thresholds to those obtained using a two interval forced choice task, it could be argued to have led some subjects in our experiment to adopt conservative criteria for responding during the detection staircase, which would yield an overestimate of the thresholds. Figure 6.9 presents the results of the measurements. The mean threshold was 0.46 m/s^2 , with standard deviation 0.18 m/s^2 . Measured thresholds for 10 of the 20 subjects were higher than the low-amplitude (0.43 m/s^2) stimulus by more than two standard errors of the mean. For the subgroup of 10 participants with the highest thresholds, we analyzed proportions of responses “more compliant” from the no-vibration (0.0 m/s^2) to the low-amplitude (0.43 m/s^2) vibration condition at the same stiffness value (90 N/mm) as was used in the threshold measurement. A paired

Table 6.3 Experiment 2: Median values of the PSE, slope, and intercept from per-subject psychometric curve fits at each vibration amplitude level.

	Median Value at Peak Amplitude A			Friedman Test	
	0.0 m/s ²	0.43 m/s ²	0.86 m/s ²	$\chi^2(2)$	p
PSE (N/mm)	100.8	134.5	151.6	34.9	$< 10^{-7}$
Slope (mm/N)	0.025	0.018	0.018	17.2	< 0.0002
Intercept	-2.50	-2.70	-2.77	3.9	> 0.14

two-tailed t-test revealed a significant effect of amplitude on these response proportions (mean 0.41 vs. 0.71 with $p < 10^{-4}$, $t(18) > 5.2$); see Figure 6.9. The median PSEs of the psychometric fits for the same subgroup of 10 participants were also significantly higher in the low-amplitude condition than in the no-vibration condition (median 135.2 N/m vs. 99.2 N/m, Friedman $p \leq 0.0005$, $\chi^2 = 12$), and were close in value to the median PSEs for the complete subject pool. However, the threshold values for the entire subject pool ($n = 20$) were not significantly correlated with PSE values in either the low or high vibration amplitude condition, with differences in PSE values between vibration and no-vibration cases, or with mean response proportions at stiffness 90 N/mm (Spearman $|\rho| < 0.21$, $p > 0.37$ in all cases).

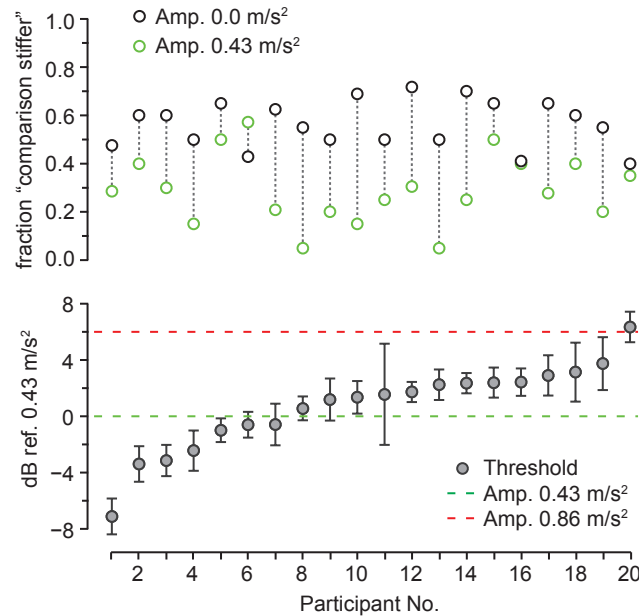


Fig. 6.9 Experiment 2: Psychophysical amplitude detection thresholds and response proportions at stiffness level 90 N/mm. Top: Response proportions for all 20 subjects at two lowest vibration levels, and stiffness level 90 N/mm. Bottom: Amplitude threshold levels, displayed in dB referenced to 0.43 m/s². Subjects are sorted in order of increasing threshold (same ordering top and bottom). The dashed lines indicate the amplitudes of the vibrating stimuli used in Experiment 2. Error bars: ± 2 SEM.

The post-experiment questionnaire that was completed by Experiment 2 subjects prior to the threshold measurement included the question: “Did you feel any vibration produced by the tile?” Five out of twenty subjects responded “No”. A sixth noted that he felt

vibration on just 5% of trials, and a seventh reported feeling no vibrations, but did report feeling “a creaking”, “like stepping on an old hardwood floor” on some trials. The remaining 13 subjects answered “Yes”.

6.5 Discussion

These experiments demonstrate that the perceived haptic compliance of a walking surface is increased in the presence of plantar cutaneous vibration feedback. In Experiment 1, we found that the largest effect on perceived compliance was due to vibration amplitude, and that other stimulus factors had a weaker influence. We also found that an increase in perceived compliance could be achieved with types of vibration feedback that differed in waveform, amplitude envelope, or the frequency distribution of their energy.

In Experiment 2, we found that vibromechanical stimuli with peak amplitudes of only 0.43 and 0.86 m/s² could elicit an increase in perceived compliance. These levels were 18 dB smaller than those used in Experiment 1. This held at all tested levels of stiffness. A substantial increase in the stiffness of the vibration-augmented plate was required for it to be perceived as having the same stiffness as the non-augmented one, as the vibration feedback produced positive relative shifts in the median PSE values for stiffness of 34% and 50% at the two amplitude levels.

The amplitudes used in Experiment 2 were considerably smaller than what are experienced during normal walking on natural granular materials such as gravel.² Through pre-testing for Experiment 2, we determined that higher amplitudes tended to dominate the influence of mechanical stiffness over the range explored. The upper limit of the stiffness range used approached a level at which stiffness perception underfoot is less reliable [33], while the smallest stiffness was near the limit of what we determined subjects could comfortably and safely walk on with this apparatus.

None of the experiments involved training, and the effects observed did not require awareness that vibration feedback was being provided. We can conclude that vibration felt during stepping on a rigid surface is combined with the mechanical stiffness of the surface in the haptic perception of compliance. In addition, the results show that the variation of

²Mechanical vibrations measured at the shoe sole during walking on medium rock gravel are broadly distributed in frequency with RMS acceleration amplitudes as high as 10 m/s² [38], comparable to those used in Experiment 1 and significantly larger than those used in Experiment 2.

vibration feedback alone is sufficient to elicit a percept of compliance.

The compliance estimation task adopted in this study resembled prior experiments in which subjects used their hands or arms to estimate the haptic compliance of spring-loaded mechanisms or other objects with non-deformable surfaces [184, 186, 187]. Based on those results, and on considerations of contact mechanics, it was expected that subjects in our experiments required both force and displacement information (from kinesthetic and tactile channels) in order to judge compliance. In this light, it appears that added vibration feedback results in a modification of force and/or displacement information that increases compliance estimates. As noted earlier, localized vibration stimulation of the foot sole has been shown to have a similar effect on postural control to an increase in force sensation at the same location [193, 194], and this could be thought to influence compliance judgments. However, an ideal observer combining force F and displacement x to estimate compliance using the formula $C = x/F$ would produce lower compliance estimates as force sensation is increased. Our results show an opposite tendency, so it appears unlikely that the observed effects on perceived compliance were mediated by increased sensations of applied force. Furthermore, stimuli used in Experiment 2 had a peak amplitude of 0.43 m/s^2 , less than 0.5% as large as the smallest amplitude used in the aforementioned studies.³ Furthermore, in our experiment, stimuli were felt through a shoe, whereas those used in the aforementioned studies involved direct skin contact.

It might be suggested that the observed results could be attributable to sensory adaptation of SA I afferents due to the vibromechanical stimuli, which could yield a reduction of force estimates. However, in our experiments, exposure times averaged less than 1 second, with at least 5 seconds between presentations, whereas mean adaptation times for SA I afferents are about 10 seconds [203, 204]. Additionally, Experiment 2 was based on pairwise comparison of two stimuli, only one of which could include vibrations. Also, the low-amplitude Experiment 2 stimuli were 0.6 dB weaker than the mean psychophysical detection threshold measured for our subject pool. While this might be partly attributable to a tendency of the measurement method used to overestimate the thresholds, it nonetheless appears unlikely that these stimuli could have produced a significant adaptation of SA I responses, even after long exposure times. Furthermore, no subjects reported feeling any desensitization in their feet, and several were unaware of the vibrations. Thus, it appears

³To compare stimuli, we computed accelerations used in experiments by Roll et al. [193, 194] from the stimulus properties they reported.

unlikely that sensory adaptation played a significant role.

Conversely, prior studies have demonstrated that sub-threshold levels of plantar stimulation with vibration noise can enhance cutaneous sensitivity in the foot soles, stabilizing posture [205]. Although such an effect, if present, could have improved haptic force discrimination in our experiment, it would not be expected to influence mean compliance estimates, so does not seem to be able to explain our main results.

Experiments 1 and 2 compared the perceived compliance of plates with and without vibration feedback. A priori, due to this categorical difference, subjects could have responded based on cognitive criteria unrelated to a sensation of compliance. However, there are several reasons we do not believe cognitive effects played an important role. Subjects were consistent in responding that the vibrating plates were more compliant, and no subject inverted this relation. Experiment 2 results did not indicate any tendency on the part of subjects to respond indiscriminately that the vibrating stimulus was “softer” independent of actual compliance. In addition, vibration had a significant influence on compliance at both near-threshold levels (Experiment 2) and at much higher ones (Experiment 1). Furthermore, some subjects in Experiment 2 reported that they were not consciously aware of the presence of vibration feedback. Finally, a few subjects described what they felt in a way that is consistent with the notion of a material being compressed underfoot, and similar responses have been received over the course of numerous demonstrations of the apparatus to naive users.

Taken together, our findings appear to be consistent with the hypothesis that vibration feedback supplied a cue that tended to increase perceived displacement during stepping, due to a sensorimotor contingency similar to that experienced when stepping on a natural material (e.g., snow, gravel) or displacing a mechanism with friction (e.g., a pedal or slider). Assuming this to be the case, and supposing that perceived force was not affected, an ideal observer would infer an increase in compliance that grows linearly with the increased sensation of displacement, due to the relation $C = \Delta x/F$. In this model, a relative increase in estimated displacement of 25.0% and 33.5% in the low- and high-amplitude vibration conditions, respectively, would be required to explain the shifts in median stiffness PSE values measured in Experiment 2.

One counterintuitive finding is that stimuli with amplitude envelopes that were constant could evoke an increased sensation of compliance, contrary to the idea that vibration supplies a force-dependent displacement cue. However in the conditions of this study, vi-

bromechanical energy transmitted to the leg increased with applied force F , due to the increased coupling of foot and plate, even for constant stimuli. As a result, the feedback could appear to have been generated by a stepping action even when there was no explicit relation with applied force, due to the transitive nature of foot-plate contact.

A number of disorders, the most common being diabetes, can impair cutaneous tactile sensation in the feet and have detrimental effects on locomotion [175, 176, 177]. This has led various researchers to investigate relations between sensory impairment and control of balance or locomotion. The present study suggests that vibrotactile sensation may be more involved in the regulation of walking in natural environments than has been acknowledged. One pilot study found that step-synchronized plantar vibration feedback during foot-ground contact may improve locomotion in Parkinson's disease patients, but there were insufficient controls to rule out learning or attentional effects [206]. However, it is plausible that the effects investigated here could play a role in such settings.

Through preliminary body kinematic analyses using motion capture measurements we have found indications of postural modifications during stepping when plantar vibration feedback is supplied. This would be consistent with postural kinesthetic illusions that, absent restraints, result in compensatory body sway [194]. If confirmed, such results might one day prove useful for the development of gait rehabilitation techniques or vibrotactile orthotics. We intend to explore these questions further in future work. Finally, we note that the same compliance illusion seems to be present during interaction via the hands. This is also something we plan to investigate further, in order to situate our results relative to prior literature on manual haptic perception.

Chapter 7

Stochastic Simulation of Fracture Processes in Heterogeneous Materials

Preface to Chapter 7:

The displacement of many natural ground materials is accompanied by texture-like vibrations that are produced through inelastic processes like friction and fracture. The manifestation of these processes in some disordered materials, like those found in natural ground surfaces, is analyzed in this chapter and the one that follows, using tools from stochastic physics.

Chapter 7 analyzes texture-like mechanical signals arising from contact interactions with disordered, heterogeneous materials like those commonly encountered in natural walking terrains. It proposes novel methods for simulating stress fluctuations in fiber composite materials and compressed granular matter under load, based on variations of the widely studied Fiber Bundle Model, and formulates what are arguably the first physically based algorithms for the real-time synthesis of high-frequency haptic and auditory signatures of dynamic fracture processes in quasi-brittle, heterogeneous materials.

Abstract Fracture-like processes in many quasi-brittle heterogeneous materials under load give rise to complex, effectively random patterns of failure in time. This chapter proposes efficient methods for simulating fracture processes in heterogeneous materials, based on variants of the widely used Fiber Bundle Model. This consists of a spatially distributed array of brittle elastic fibers arranged in parallel. We present a novel temporal formulation of this model based on two complementary constructions. The first is an exact stochastic jump process associated with the sequence of random fiber failures under loading. The second is a smooth, deterministic dynamical process that approximates the mean stress-strain response of the original model. We apply this construction to two failure processes that have been treated in prior literature on FBMs: fracture in fiber composites and failure in compressed granular materials. Through numerical simulations, the approximate model introduced here is demonstrated to accurately reproduce the constitutive behavior and statistical fluctuations exhibited by the original. In addition, it is efficient enough to interactively simulate stress fluctuations and acoustic emissions generated during the loading of large ensembles of fibers (thousands or more), and is amenable to the simulation of local fracture processes in a distributed medium, which could aid applications in scientific visualization or virtual reality.

7.1 Introduction

Processes associated with progressive failure in disordered, heterogeneous materials such as gravel, soil, fiberglass, or wood have attracted interest in scientific and engineering research over the course of several decades. They are relevant to applications ranging from industrial material handling, to snowboard design and snow failure prediction [207]. A full microscopic understanding of structural failure in quasi-brittle heterogeneous materials remains elusive, due to the large number of randomly arranged elements or domains that comprise them. Nonetheless, the spatial distribution of stresses in such materials is highly organized, allowing many aspects of their failure under load to be captured via comparatively simple statistical models [11, 10]. In addition, because the evolution of fracture processes is greatly influenced by the spatial composition of the materials involved, the pattern of temporal failures accompanying fracture in heterogeneous materials richly encodes their spatial disorder.

Fracture-like processes occur in a diverse variety of quasi-brittle, heterogeneous mate-

rials under load. Here, we investigate their manifestation in fiber composites and granular media. A common feature of these types of material is their tendency to bear stress along arrays of brittle, one-dimensional structures loaded in parallel (Figure 7.1). Physical phenomena associated with fracture in such settings depend both on static properties, such as typical fiber strength and material geometry, and dynamic attributes, such as response times during fracture, load redistribution or stress percolation, hardening, and relaxation or creep. Fracture evolution is reflected through temporally disordered patterns of rapid, inelastic dislocation and acoustic emission accompanying the failure of force-bearing structures. In strongly disordered materials like granular media, these fluctuations can be as important as the mean constitutive behavior [14, 13].

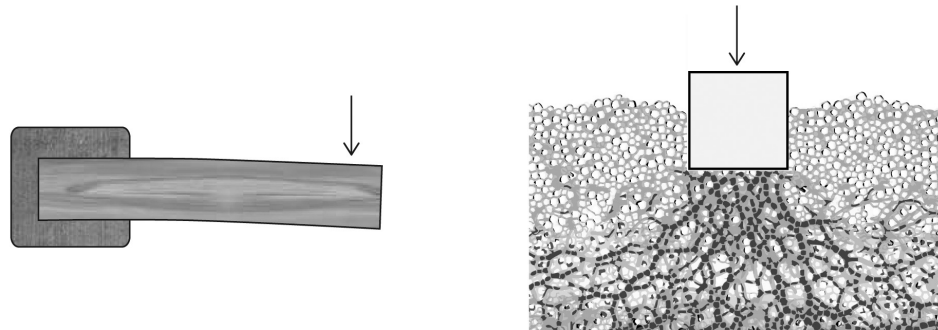


Fig. 7.1 Fiber Bundle Models have been successfully used to model fracture physics in quasi-brittle materials that effectively bear stress along arrays of one-dimensional structures loaded in parallel. Examples include natural fiber composites such as wood (left), and granular media, such as sand or gravel (right), where stress is transmitted along one-dimensional force chains (dark areas).

A class of statistical models known as Fiber Bundle Models (FBMs) and their variants have been intensively investigated during the last few decades as effective physical descriptions of fracture and other inelastic processes in heterogeneous materials [11, 208]. They consist of parallel arrays of one-dimensional (“fiber-like”) brittle elastic elements distributed over a spatial lattice. Although the spatial representation of fracture processes that they provide is greatly simplified, it captures important aspects of random failure in disordered, heterogeneous materials. In addition, they are more analytically and computationally tractable than lattice-, particle-, or continuum mechanics approaches, such as the random spring model, discrete element method, or finite element models. Despite

their simplicity, FBMs capture many of the distinctive aspects of damage in heterogeneous materials, including statistical strength distributions, stress fluctuations, reorganization accompanying failure, acoustic emissions, and accumulated damage, that standard continuum mechanics models of fracture, based on mean-field or homogenized constitutive equations, cannot [11]. Although improved finite-element methodologies have been developed to better capture such phenomena, the simulation of inelastic damage processes in quasi-brittle, heterogeneous materials that exhibit important stress fluctuations poses an outstanding challenge to research in this area [11]. Furthermore, even in relatively homogeneous solids, real-time simulation of brittle fracture using finite-element methods is only possible with severe accuracy-performance compromises. This can produce visual results that may be sufficient for entertainment or gaming, but which are of limited physical validity [209].

This paper presents new methods for simulating failure processes in fiber composites and in compressed granular matter, respectively based on variations of the Fiber Bundle Model and the so-called Inverse Fiber Bundle Model. The methods we present are based on a novel factorization of these models into an approximate mean constitutive response, describing the averaged nonlinear stress-strain behavior, and a stochastic jump process (presented here for the first time) modeling the fluctuating pattern of failures in the material. The former aspect allows the (smooth) stress-strain dynamics to be simulated deterministically, unlike standard treatments of FBMs, where it depends on the (rapidly fluctuating) random failure history in the material. The latter provides an iterative stochastic description of thresholds of failure in the material as it is loaded. Section 7.2 presents novel methods for simulating the Fiber Bundle Model for failure in fiber composites. In Section 7.3, stress fluctuations in compressed granular media are treated using a similar approach. The results of simulations are presented in Sections 7.2.3 and 7.3.3. Section 7.4 describes audio-rate real-time implementations of these algorithms. Section 7.5 concludes with a discussion of the main results and future extensions of this work.

7.2 Fracture processes in fiber composites: Fiber Bundle Model

Fiber reinforced composites consist of solid materials composed of strong fibers embedded in a matrix. Examples include natural materials like wood, or synthetic materials like fiberglass to which fibers are added to improve the mechanical performance. Fiber Bundle Models have proven to be very effective in modeling constitutive and transient aspects of

the mechanical response of such materials. They are modeled as a bundle of N fibers as a parallel array of mechanical elements, arranged in a lattice or a linear array, as illustrated in Figure 7.2. The displacement $x(t)$ of the system evolves continuously, subject to

$$\sigma(t) = N_F(b_F\dot{x} + k_Fx) + N(b_R\dot{x} + m\ddot{x}) \quad (7.1)$$

where N_F is the number of intact fibers. Fracture in a fiber occurs when its strain $x(t)$ exceeds that fiber's breaking threshold ξ . When this occurs, the load that the fiber carried is immediately redistributed among those that remain. The resulting transient response is parametrized by the effective (per-fiber) mass m , elastic constant k_F and two damping constants b_F and b_R . The breaking thresholds ξ for different fibers are distributed randomly according a probability density $p(\xi)$. Following failure, a broken fiber contributes to relaxation via the damping unit b_R , which can model creeping displacement in the matrix or sliding of fibers against it [210]. Numerous variations on this basic model are possible [208]. Elastic properties of the matrix may be introduced by placing b_R in parallel with an elastic element with stiffness k_R , or relaxation may be omitted entirely by setting $b_R = 0$. Each breaking fiber releases an amount of energy given by $E = k_F\xi^2$, which depends on the strain $x = \xi$ at the instant it fails.

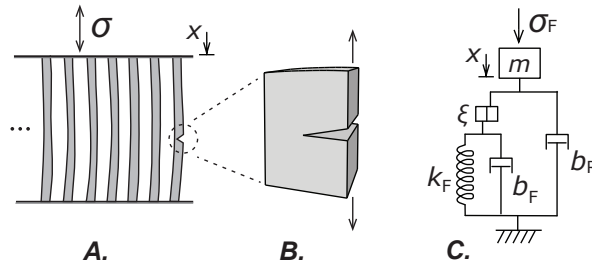


Fig. 7.2 Fiber Bundle Model of fracture. **A.** The parallel array of N brittle fibers is loaded in compression or tension with externally applied stress σ . **B.** At the crack front, the weakest surviving fiber approaches failure due to local stress $\sigma_F = \sigma/N_F$, where N_F is the number of intact fibers. **C.** A simple mechanical analog for the generation of fracture events in each fiber of the bundle. Brittle fracture is modeled by a plastic unit that breaks when the force on it is greater than a random threshold ξ , resulting in disconnection of load-bearing spring k_F and damper b_F . Post-fracture relaxation is modeled via the persistent damping factor b_R .

Although stress is redistributed locally in real materials, which can significantly affect material strength and stress fluctuations [211], we make the simplifying assumption of global load sharing between fibers, so that the per-fiber load σ_F is σ/N_F . Possible extensions of this work that would account for local load sharing are discussed in Section 5.7. Since a fracture event decreases N_F , the failure of a single fiber can increase the load on those that survive, leading to additional failures. This continues until $x(t) < \xi^*$, where ξ^* is the threshold of the weakest surviving fiber. When a critical value σ_c of the applied stress is reached, the bundle will be incapable of supporting the load, and all remaining fibers will break in order of increasing strength. The number N_F of fibers surviving at a given load depends on the random assignment of thresholds, but its expected value is $\bar{N}_F = N(1 - P(x))$, where $P(\cdot)$ is the cumulative distribution function (CDF) of $p(\cdot)$.

FBMs are normally treated as distributed models comprised of lattices of fibers with breaking thresholds ξ_j that are independently drawn from $p(\xi)$, and (at least for global load sharing models) sorted in increasing order (so that $\xi_j > \xi_{j-1}$) at the time of model instantiation. Thus, in conventional simulations, although an analytical solution is not necessarily known in advance, the evolution is completely deterministic, with the source of uncertainty hidden in the lattice initial conditions.

Although physically correct, this makes it difficult to discern the extent of interaction between the instantaneous dynamical evolution of the model and the random probability of failure at any time. In addition, the dynamical evolution of the model at any instant in time is linear, and does not reflect the nonlinear constitutive (stress-strain) behavior.

In order to derive a temporally local formulation that reflects the most salient mean and fluctuating aspects of the model, we proceed in two steps. First we derive a stochastic process that exactly governs the failure events of the model, then develop an approximation that allows us to separate the constitutive dynamical evolution from the random failure process.

7.2.1 Stochastic process formulation

At any time the evolution of the FBM is determined by the number N_F of intact fibers and, when a failure event is encountered, on the breaking threshold ξ^* of the weakest intact fiber in the bundle, which indicates when the next random failure event will occur. Upon failure, the breaking threshold of the weakest intact fiber increases by a random amount

that can be considered to be determined by $p(\xi)$ and the number of failures until that instant, equal to $N - N_F + 1$. This process can be naturally described by considering the weakest fiber threshold $\xi(t) = \xi^*$ at any instant t to be a stochastic *jump process*, defined as a temporally fluctuating, monotonically increasing function $\xi(t)$ of continuous time, whose j th piecewise-constant value $\xi(t) = \xi_j$ is computed at the instant $\xi(t - dt) = \xi_{j-1}$ is surpassed.

Here, we provide a temporally local definition of the process $\xi(t)$ that also ensures that it follows the desired strength distribution $p(\xi)$. The procedure is based on known algorithms for random variate generation [212]. First, we construct an ordered set s_j of N random variables ($s_j > s_{j-1}$, $0 \leq j \leq N$) uniformly distributed on the interval $[0, 1]$, then map these onto random variables ξ_j distributed according to $p(\cdot)$ using the inverse CDF method [212]. Let u_j be independent samples of a random variable uniformly distributed in $[0, 1]$, and set

$$s_0 = 0 \quad (7.2)$$

$$s_j = s_{j-1} + (1 - s_{j-1}) \left(1 - u_j^{1/N_F^j}\right), \quad j = 1, 2, \dots, N \quad (7.3)$$

$$\xi_j = P^{-1}(s_j), \quad j = 1, 2, \dots, N \quad (7.4)$$

where $P(\cdot)$ is the CDF of the fiber strain threshold distribution, and $N_F^j = N - j + 1$ is the number of surviving fibers prior to the j th failure. By construction, the resulting threshold sequence is equivalent to a set of N independent samples from $p(\xi)$ that have been sorted in increasing magnitude. The algorithm is illustrated in Figure 7.3.

We extend the strain threshold process to a piecewise-continuous function of continuous time by defining $\xi(t) = \xi_j$ if ξ_j is the failure strain of the weakest surviving fiber at time t . Similarly, let $N_F(t)$ denote the number of surviving fibers in the sample at time t . When a fracture event occurs, the value of $\xi(t)$ jumps and that of $N_F(t)$ decreases by one. This happens whenever the strain $x(t)$ of the weakest surviving fiber at time t exceeds $\xi(t)$. This strain is given by the solution at time t of Equation (7.1).

Expressed as a function of continuous time, a fracture event at time t is accompanied by the jump from ξ to a new value ξ' given by

$$s' = s + (1 - s) \left(1 - u^{1/N_F(t)}\right) \quad (7.5)$$

$$\xi' = P^{-1}(s'). \quad (7.6)$$

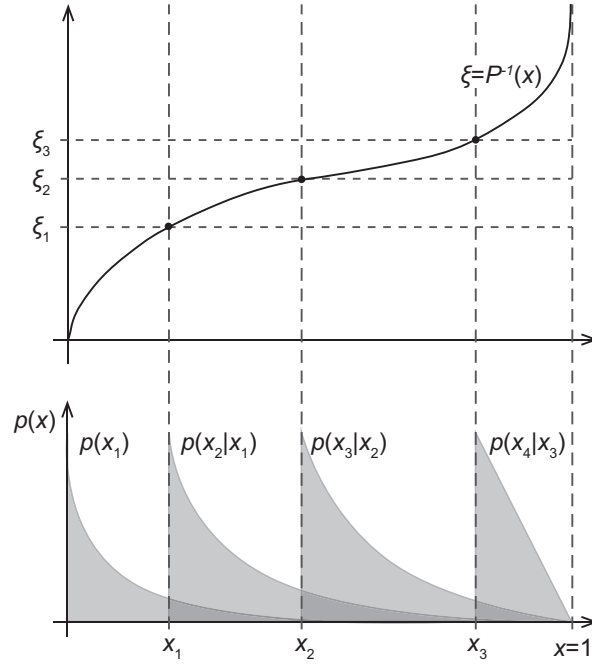


Fig. 7.3 The sequential sampling algorithm described in equations (7.2-7.4) determines the next value ξ_j of the threshold via a process that depends only on s_{j-1} , with the distribution represented by the shaded area to the right of s_j , and the number of remaining fibers, N_F^j . The modified algorithm described in the text samples $\xi(t)$ in a way that depends only on its value $\xi(t-dt)$ at the preceding instant and the load $\sigma(t)$, assuming the latter to be monotonically increasing.

Substituting the first equation into the second, and using $\xi' = P^{-1}(s')$, yields an expression for ξ' in terms of ξ and $N_F(t)$:

$$\xi' = P^{-1}\left(P(\xi) + (1 - P(\xi))\left(1 - u^{1/N_F(t)}\right)\right). \quad (7.7)$$

The size of a jump in ξ at time t depends on the state of the co-evolving random process $N_F(t)$ and on the value of $\xi(t)$, while the time at which it occurs depends on the relative values of $\xi(t)$ and the load-dependent strain $x(t)$. The algorithm result can be interpreted as a model of a single fiber that undergoes repeated fracture displacements of size $S(t_i) = \xi(t_i + dt) - \xi(t_i)$ at times $t_i = t_1, t_2, \dots, t_N$, similar to the Continuous Damage Model of Kun et al. [213]. The process $\xi(t)$ captures most of the interesting statistics of the response

of the FBM, including the distributions of time-intervals between fracture, and the fracture size distribution.

7.2.2 Mean damage approximations

In the algorithm presented above, the strain threshold $\xi(t)$ depends on the level of damage at the time of fracture (represented through N_F), which is itself a random value that depends on the history of failures in the sample. Similarly, the strain $x(t)$ depends on the stochastic evolution of damage in the bundle. We asked whether one can usefully approximate the model in such a way that the strain and damage evolve deterministically, with random effects entirely captured by ξ . Such an approximation can be obtained by replacing $N_F(t)$ in the jump and evolution equations, (7.7) and (7.1), by the expected survival number $\bar{N}_F(t)$ given the load history. The latter is indicative of the mean damage that would be expected for an ensemble of instances of the model subjected to the load $\sigma(t)$ until time t .

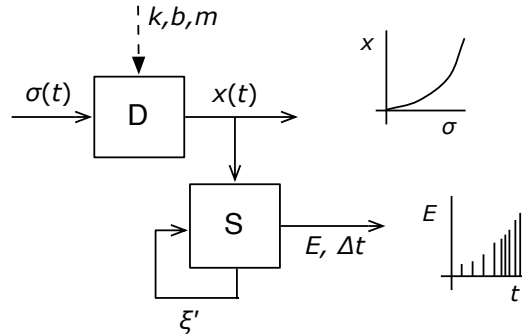


Fig. 7.4 Illustration of the mean damage model, composed of a deterministic process D describing the mean constitutive response and a stochastic process S describing the fluctuations.

The expected survival number $\bar{N}_F(t)$ depends on the strain via

$$\bar{N}_F(t) = \bar{N}_F(x^*) = N(1 - P(x^*(t))), \quad x^*(t) = \max_{t' < t} x(t'). \quad (7.8)$$

Under monotonically increasing loading, this is simply $\bar{N}_F(t) = N(1 - P(x(t)))$. Upon replacing N_F by \bar{N}_F this yields factorization of the model into a deterministic part D ,

governing the nonlinear stress-strain response,

$$\sigma(t) = \bar{N}_F(t)(b_F \dot{x} + k_F x) + N(b_R \dot{x} + m \ddot{x}) \quad (7.9)$$

and a stochastic jump process S describing the stress fluctuations:

$$\xi' = P^{-1} \left(P(\xi) + (1 - P(\xi)) \left(1 - u^{1/\bar{N}_F} \right) \right) \quad (7.10)$$

while $x(t) > \xi$.

This model system is illustrated in Figure 7.4. Both portions of the model depend, through $P(\cdot)$ and \bar{N}_F , on the form of the breaking distribution $p(\xi)$ that is adopted.

Uniform failure distribution The simplest choice of breaking distribution is that which is uniform on the unit interval $[0, 1]$. Assuming slowly increasing loading, $x^*(t) = x(t)$, so that $\bar{N}_F(t) = N(1 - x(t))$, the homogenized nonlinear stress-strain response becomes:

$$\sigma(t) = N(1 - x) (b_F \dot{x} + k_F x) + N(b_R \dot{x} + m \ddot{x}) \quad (7.11)$$

while the increased threshold ξ' is sampled as:

$$\xi' = \xi + (\xi - 1)^2 (u^{1/(N(1-\xi))} - 1), \quad (7.12)$$

where u is a sample of a random variable uniformly distributed in $[0, 1]$.

Weibull failure distribution The Weibull distribution has been found to be a good empirical statistical distribution for solid strength in materials science. The Weibull CDF is given by

$$P(\xi) = 1 - \exp(-(\xi/\lambda)^k) \Theta(\xi) \quad (7.13)$$

where λ and k are scale and shape parameters, and $\Theta(\cdot)$ is the Heaviside step function, with $\Theta(\xi) = 0$ for $\xi < 0$ and $\Theta(\xi) = 1$ for $\xi > 0$. For this choice of distribution, under slowly increasing loading, the mean damage model can be written as

$$\sigma(t) = N \exp(-x/\lambda)^k (b_F \dot{x} + k_F x) + N(b_R \dot{x} + m \ddot{x}) \quad (7.14)$$

with the jump event sampled as

$$\xi' = \lambda (\xi/\lambda)^k \log \left(1 - e^{-(\xi/\lambda)^k} \left(1 - u^{1/(N \exp(-\xi/\lambda)^k)} \right) \right)^{1/k}. \quad (7.15)$$

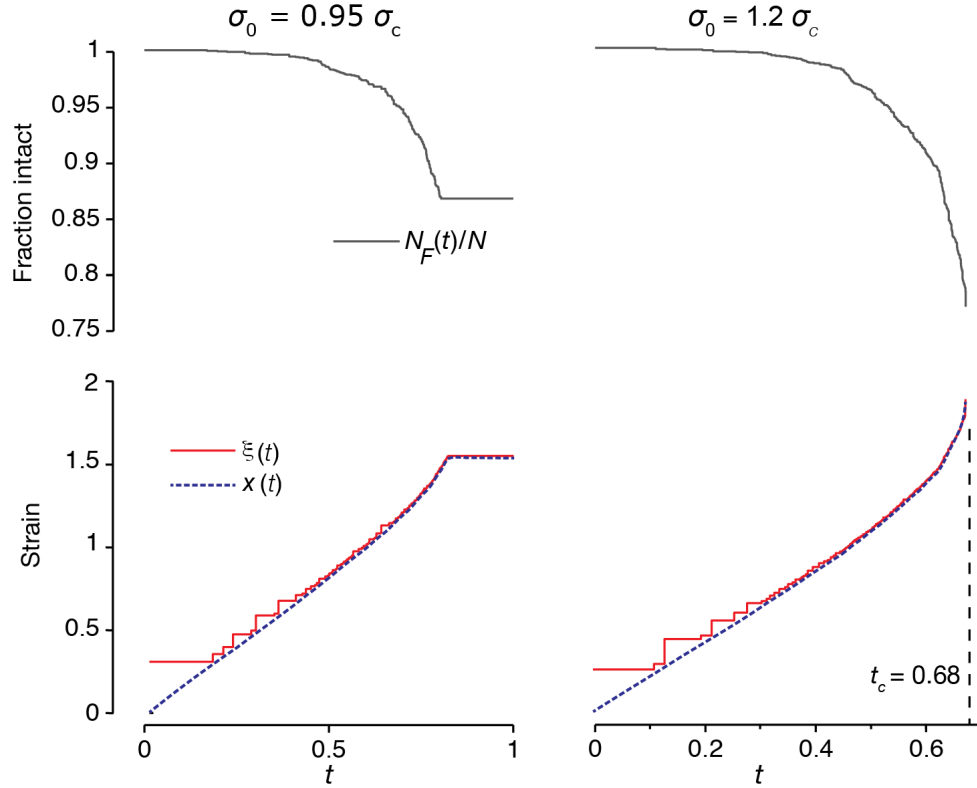


Fig. 7.5 Typical stress-controlled loading responses to $\sigma(t) = \sigma_0 r(t)$, where $r(t) = 0$ for $t \leq 0$ to $r(t) = 1$ for $t \geq 0.8$, for a simulation with 2000 fibers, and Weibull-distributed thresholds (parameters $k = 4$ and $\lambda = 2.5$). Top row: The surviving fraction $N_F(t)/N$ of fibers is shown. The maximum stress for each column is indicated at top relative to the critical stress $\sigma_c = 2800$. $\sigma_0 > \sigma_c$ in the simulation on the right hand side, and the bundle failed under load, with $N_F(t)/N$ dropping rapidly to zero at time $t_c = 0.68$. Bottom row: The fluctuating threshold $\xi(t)$ and the strain $x(t)$ are displayed.

7.2.3 Numerical simulations

For convenience, we refer to the original FBM and the mean damage version as M and \bar{M} . Although the validity of the mean damage approximation is not obvious, the most salient

phenomena to Fiber Bundle Models of fracture (e.g., the value of the critical stress σ_c , or scaling behavior of fluctuations as failure approaches (Sec. 7.2.3)) are known to depend only weakly on the precise distribution of fiber strengths [11, 208]. In addition, the relatively slower deterministic part of the \bar{M} differs from M only due to effects of fluctuations in the number N_F of intact fibers, which can be regarded as a source of high-frequency noise that should approximately average to zero. Thus, we hypothesized that even if fluctuations in N_F are significant, the resulting behavior will be similar in both cases. We evaluate this hypothesis empirically in the next sections.

To evaluate the Fiber Bundle Model algorithms presented above, we performed simulations by numerically integrating the dynamical equations, using the exact algorithm and the approximate versions. The stress-strain constitutive behavior, time to failure, and the distribution of response fluctuations for each were tested under stress-controlled loading with a slow ramping force input $\sigma(t) = \sigma_0 r(t)$, where $r(t) = 0$ for $t \leq 0$ to $r(t) = 1$ for $t \geq 0.8$. A Weibull distribution of breaking thresholds was used, as in Equations (7.14) and (7.15).

For the simulations, the ordinary differential equation (ODE) describing the system evolution between failure was integrated, and failure was tested at each time step. Upon failure, new values of the fluctuating fiber strength $\xi(t)$ were sampled using Equation (7.3) until $\xi(t) > x(t)$. When N is large, due to the frequent fracture events, the equations for model M appear to become stiff, so a variable time step implicit ODE solver was used with both, to avoid any effects of the integration method on the comparison.

Stress-controlled loading responses for both models are shown in Figure 7.5. The results for each are qualitatively indistinguishable, so examples are only given for model M . The per-fiber load increases linearly until the current threshold level $\xi(t)$ is met, at which point one or more fibers fail and a new value of $\xi(t)$ is sampled. The size and density of these failure events increase with the applied load, until the model reaches a stable point, or a critical load is achieved, causing the bundle to collapse.

The stress-strain relationships for both the exact and approximate algorithms are shown in Figure 7.6. These relationships and the critical load estimates were obtained from a sampling of 200 uniformly spaced values of the terminal load, extending from sub-critical to supra-critical values. Qualitatively the curves for each are nearly identical. Approximation \bar{M} yields a discrepancy of less than 2% in the critical load ($\sigma_c = 2850$ vs. 2800).

Figures 7.7 and 7.8 examine the empirical distributions of failure event time intervals

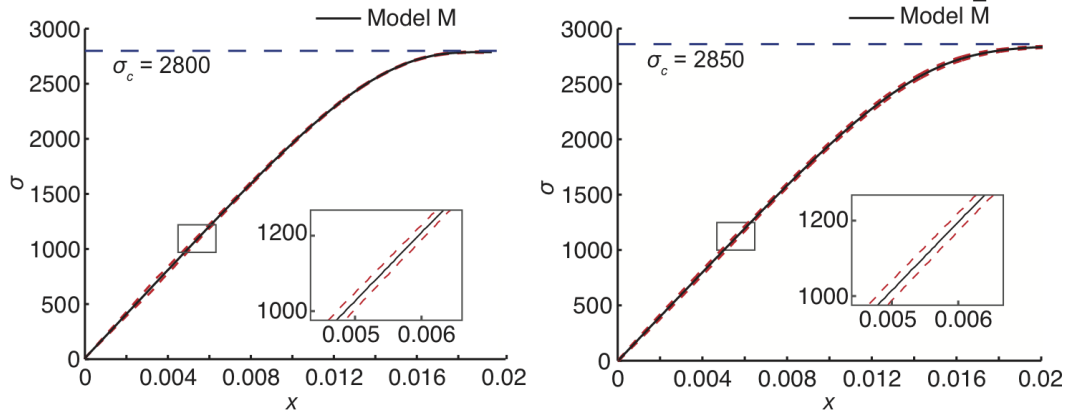


Fig. 7.6 The constitutive stress-strain relationship $\sigma(x)$ for models M and \bar{M} . Simulated measurements were made under slow ramp loading conditions, as in Figure 7.5, at supra-critical values of the applied stress, $\sigma > \sigma_c$. The curve shown is the mean of 200 simulations with 2000 fibers. The blue dashed line shows the critical stress values of $\sigma_c(M) = 2800$, $\sigma_c(\bar{M}) = 2900$ and $\sigma_c(\bar{M}) = 2850$. The mean damage approximation yields a discrepancy in σ_c of less than 2%. The dashed red lines display 95% confidence intervals.

Δt and of energy fluctuations E for the two models. The fracture of a fiber at strain x releases an amount of energy given by $E = k_F x^2$. To estimate the distribution of energy fluctuations, energy released by all events within each time window of duration 0.005 was integrated. The results for each model are qualitatively similar, and exhibit approximate power law scaling behavior expected during fracture approaching critical failure at load σ_c [208]. Modest disagreements between the distribution of event time intervals obtained with models M and \bar{M} occur at relatively frequent but small values of Δt .

7.3 Stress fluctuations in compressed granular media

Complex patterns of force fluctuations accompany the compression of stiff granular materials, which, as in the case of fiber composite materials, have been successfully modeled in terms of the inelastic failure of one-dimensional structures loaded in parallel [214, 215]. The latter arise due to the organization of stress in granular materials in highly heterogeneous force networks. Most stress in these materials is concentrated along one-dimensional chains of contacting particles. This has important consequences for the macroscopic dynamics of these materials. It can, for example, result in the clogging of granular material

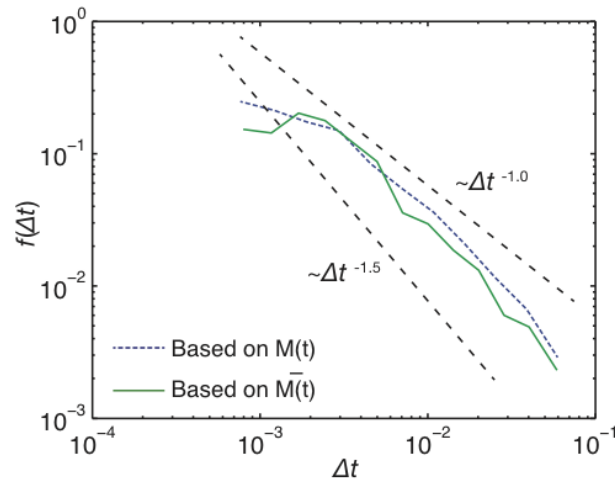


Fig. 7.7 Distribution of times between failure events, Δt , for each model, demonstrating similar, approximately power law scaling behavior, with and without the mean damage approximation. Distributions were estimated from 200 simulations of bundles with 2000 fibers subjected to ramp loading. Other simulation details were as in Figure 7.5.

flows through narrow passages in industrial hoppers, due to the formation of bridge-like structures between the surrounding walls (Fig. 7.9).

Axially compressed granular materials are supported primarily by force chains percolating along the direction of the principle axis (Fig. 7.10). When compressed, these chains are created and restructured due to relative displacements of the grains, which rearrange their positions until a stronger, stable configuration is reached. Because energy is rapidly dissipated in granular assemblies (as evidenced by the short time taken for sand poured onto a flat surface to come to rest), for stiff materials, these rearrangements occur rapidly and highly inelastically, giving rise to large transient stress fluctuations. The latter are widely used to study the evolution of force chains during loading [216, 214].

7.3.1 Inverse Fiber Bundle Model

A model for the evolution of force chains during compression was proposed by Hidalgo et al. [214, 215], as an extension of the continuous damage Fiber Bundle Model, which had been previously used to describe the failure of fiber-reinforced composites [213, 217]. They conducted experiments in which an ensemble of granular particles was monitored while it

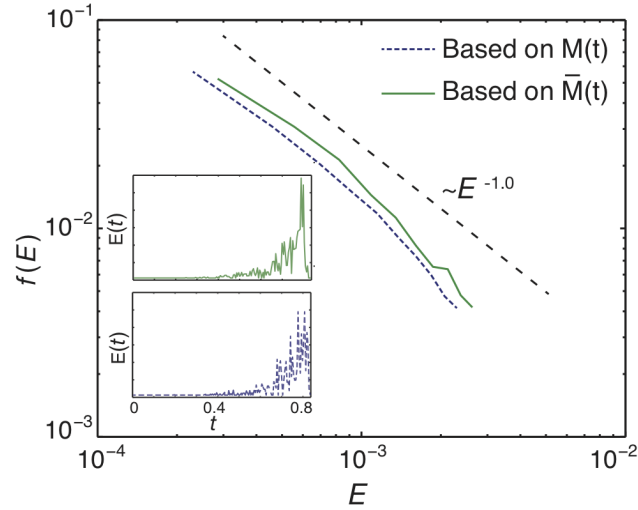


Fig. 7.8 Empirical distribution of fracture energy E in windows of duration 0.005, showing approximate power law scaling behavior for the same two models. Inset: Energy burst size vs time during one simulation trial. Distributions were estimated from 200 simulations of bundles with 2000 fibers subjected to ramp loading. Other simulation details were as in Figure 7.5.

was subjected to uniaxial compression. Their model effectively captured both the nonlinear constitutive behavior of the medium and predicted the amplitude distribution of acoustic signals emitted by microscopic rearrangements of the particles during compression, yielding excellent quantitative agreement with experimental results.

In this model, granular force chains are represented by an array of fibers loaded in parallel with randomly distributed failure thresholds. However, in contrast to the standard FBM, during compression when the load on a fiber exceeds its threshold, the chain restructures, becoming stronger, stiffer and straighter. Because failure in this system is followed by a strengthening, rather than a removal, of the affected fiber, it has been called the *inverse Fiber Bundle Model*. The stiffness of a failed chain increases multiplicatively after each failure, with

$$k' = ak = k(1 + \alpha), \quad \alpha > 0. \quad (7.16)$$

Consequently, rather than weakening as a result of damage, as in the FBM, the bundle grows progressively stronger, corresponding to the increasingly dense packing of the granular medium. If viscoelastic damping is modeled, it may be similarly increased to $b' = b(1 + \alpha)$, to preserve the same damping ratio. The constitutive dynamics of the bundle

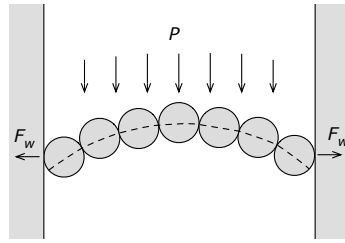


Fig. 7.9 Granular flow through a tube can become obstructed by large forces resulting from force chains bridging the walls. Such effects can disrupt industrial processes or result in costly accidents, such as the rupturing of grain silos.

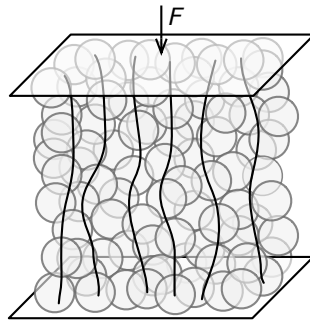


Fig. 7.10 The inverse fiber bundle effectively models a compressed granular medium as a parallel array of fibers, which represent the percolation of one-dimensional force chains through the medium.

can be described, using the parametrization of Section 7.2, by

$$\sigma(t) = A(t)(b_F \dot{x} + k_F x), \quad (7.17)$$

where

$$A(t) = \sum_{j=1}^N (1 + \alpha)^{n_j(t)} \quad (7.18)$$

and $n_j(t)$ is the number of failures of the j th fiber at time t . When a given fiber has failed a maximum number n_{\max} of times (n_{\max} is a parameter of the model), it is assumed to be unable to further restructure, attaining a maximum stiffness of $k_{\max} = k_F(1 + \alpha)^{n_{\max}}$. Subsequently, that fiber contributes a linear response. When all fibers have failed n_{\max} times, the bundle enters a linear response regime, which is also observed in packed granular

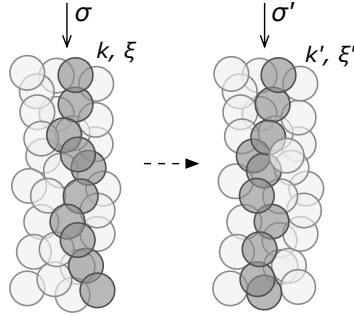


Fig. 7.11 Compression results in rapid events through which force chains are restructured, becoming stronger, stiffer and straighter.

matter.

7.3.2 Sequential algorithm and mean damage approximation

This model is amenable to a theoretical analysis of some of its statistical properties, but for present purposes we focus on simulating it using the same approach that was applied to the Fiber Bundle Model in Section 7.2.

The value of α , the relative increase in stiffness at each fracture, can be assumed to be small (in the simulations below, $\alpha = 0.005$), in which case we can approximate

$$A(t) \approx \sum_{j=1}^N (1 + \alpha n_j(t)) = N + \alpha I_F(t), \quad (7.19)$$

where $I_F(t)$ is the total number of failure events until time t .

Since the new value of the breaking threshold of a failed fiber is larger than the previous value, then if all threshold are assumed to be drawn from the same distribution, the sequential algorithm of Section 7.2.1 can be used for simulation. After a failure, the next lowest threshold of the model is drawn according to

$$\xi' = P^{-1} \left(P(\xi) + (1 - P(\xi)) \left(1 - u^{1/N_T} \right) \right). \quad (7.20)$$

In the mean damage approximation, the discrete random variables $I_F(t)$ and $N_T(t)$ appear-

ing in (7.17) and (7.20) are replaced by their expected values, yielding

$$\sigma(t) = (N + \alpha \bar{I}_F(t))(b_F \dot{x}(t) + k_F x(t)). \quad (7.21)$$

The expected number of failures $\bar{I}_F(t)$ at a given strain level is given by

$$\bar{I}_F(t) = n_{\max} N P(x^*(t)), \quad x^*(t) = \max_{t' < t} x(t'). \quad (7.22)$$

The expected survival number is, as for the Fiber Bundle Model, given by $N_F(t) = N(1 - P(x^*(t)))$. Finally, the expected value of the number of remaining failures in the bundle is $\bar{N}_T = \bar{N}_F n_{\max}$. The constitutive and fluctuating response of this model can be written as

$$\sigma(t) = N(1 + \alpha n_{\max} P(x^*)) (b_F \dot{x} + k_F x). \quad (7.23)$$

and

$$\xi' = P^{-1} \left(P(\xi) + (1 - P(\xi)) \left(1 - u^{[N n_{\max} (1 - P(x^*))]^{-1}} \right) \right). \quad (7.24)$$

Failure criteria For a material sample under a uniform, uniaxial load, either a maximum stress or maximum strain criterion may be used (the latter being identical to that employed for the fiber composite model of Section 7.2). In a local model of failure in a three-dimensional volume of granular material, the breaking threshold depends on the magnitude and directions of stresses or strains, because the load bearing force chains in the material reorganize to align with the direction of maximum stress. For coarse-grained soils or other granular media, failure can often be described by a Mohr-Coulomb yield criterion. This can be written as

$$s/n = \tan(\phi), \quad (7.25)$$

where s/n is the ratio of maximum and minimum principle stresses at the location of interest, and the parameter ϕ , the angle of repose (or angle of internal friction) of the granular material, describes the material strength.

7.3.3 Numerical simulations

The mean damage inverse Fiber Bundle Model presented above was simulated under uniaxial, stress-controlled loading, in the same manner as in Section 7.2.3. A Weibull distribution of breaking thresholds was used with the same values of the parameters as used in the previous simulations. Figure 7.12 shows typical response profiles of the model under ramp loading conditions. As noted above, the nonlinear stress-strain relation is, opposite to the case of the Fiber Bundle Model, concave, corresponding to the increasing stiffness of the granular medium as it is compressed.

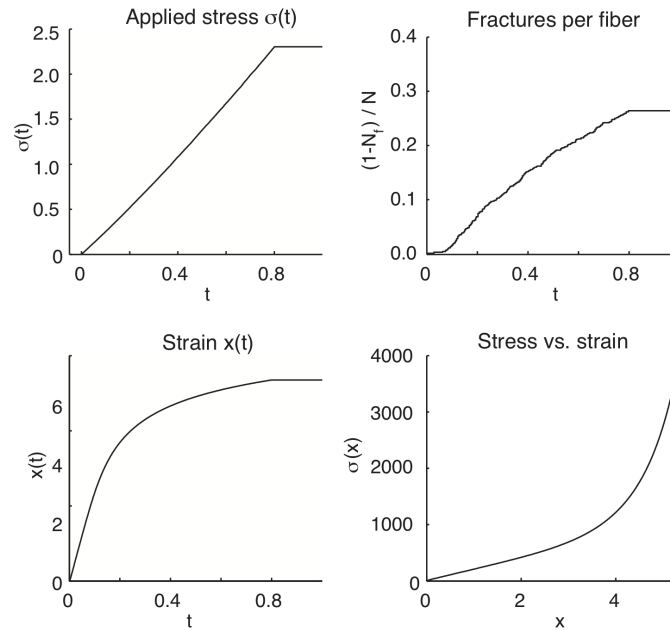


Fig. 7.12 Response of the inverse Fiber Bundle Model under ramp loading conditions. Top Left: Applied stress vs time. Top Right: Number of fracture events per fiber vs time. Bottom Left: Strain $x(t)$. Bottom right: Constitutive, stress-strain behavior. Data shown is based on 200 simulations of bundles with 2000 fibers subjected to ramp loading with maximum stress $\sigma = 2667$. Other simulation parameters were as given in Figure 7.5.

Figure 7.13 presents empirical distributions of the times Δt between failure events and of the energy fluctuations of the model during loading. Both were computed as in Section 7.2.3. Energy fluctuations are observed, for large enough values of n_{\max} , to scale as $p(E) \sim E^{-2.0}$, which is consistent with published results [214]. Theory predicts critical scaling in

this model to occur when the maximum number of permitted rearrangements n_{\max} of each fiber is large, and theoretical calculations of the values of the scaling exponents have been found to agree very well with experimental observations of fluctuations in a compressed granular system [214].

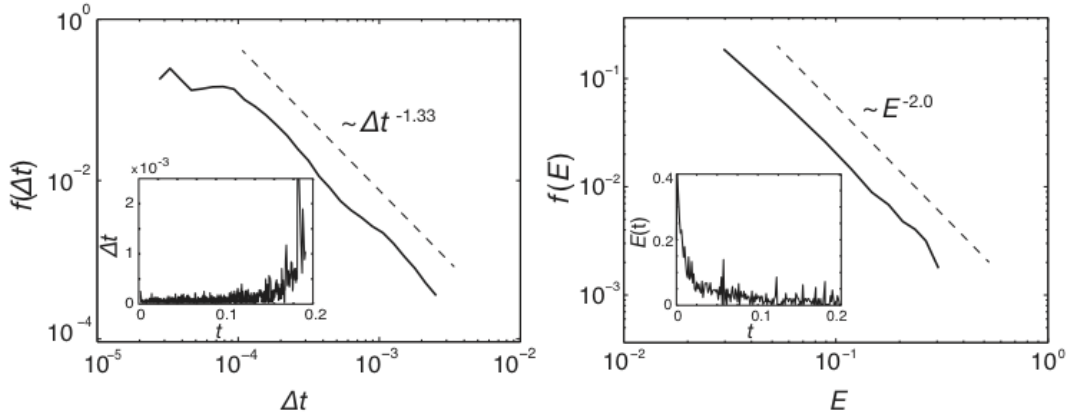


Fig. 7.13 Left: Empirical distribution of times between failure events, Δt , for the inverse Fiber Bundle Model. Right: Distribution of failure energy fluctuations (computed in windows of duration 0.005), exhibiting power-law scaling over more than one order of magnitude. Inset: Energy fluctuation size vs time during one simulation trial. Distributions were computed from 500 simulations of bundles with 200 fibers subjected to ramp loading with maximum stress $\sigma_0 = 10^5$ and $n_{\max} = 20$. Other simulation details were as given in Figure 7.5.

An example showing the response of the inverse Fiber Bundle Model to a dynamically variable applied stress (in this case, one simulating the load profile of a human footstep), is shown in Figure 7.14. Although the behavior observed is plausibly realistic, with most fracture energy produced during initial loading (heel strike) and in stress buildup prior to unloading (toe off), a more realistic response would be obtained if the spatially distributed nature of foot-ground contact were accounted for.

7.4 Real-time, interactive simulation

Interactive simulation of failure processes in quasi-brittle, heterogeneous materials is of interest for scientific visualization or immersive virtual reality. The algorithms above were

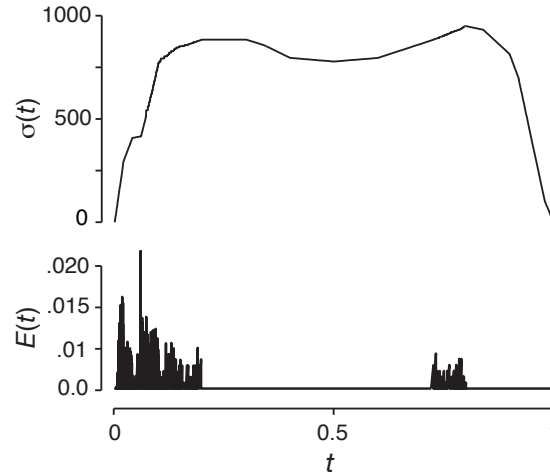


Fig. 7.14 The response of a bundle of 2000 fibers to a dynamic load, simulating that due to a footstep. Shown are the applied load $\sigma(t)$, and the energy $E(t)$ computed in windows of duration $\Delta t = 0.005$.

also implemented in real-time simulations that execute at sampling rates of 48 kHz, sufficient to reproduce stress fluctuations accompanying fracture evolution across the entire vibrotactile and audible bandwidths (Fig. 7.15). A variable stress $\sigma(t)$ (either simulated or acquired via instrumentation) is provided as a real-time input to the dynamics, resulting in a time-varying strain $x(t)$ that evokes a sequence of transient failures with energies $E = \Delta N k_F x(t)^2$, where ΔN is the number of fibers that fail in a given time-step. Discretization of the dynamics was performed via Laplace transformation of the ordinary differential equations, followed by the bilinear transform mapping from the s - to the z -plane. This explicit integration method provides a reasonable accuracy-performance tradeoff at high (audio bandwidth) sampling rates [85].

The algorithm requires minimal computation. When fracture events are sparse, most computation time is spent on the integration (model M , whose linear dynamics may be implemented as a second order IIR filter, requires five multiply-accumulate operations per sample period). When the failure rate is large, more computation time is spent updating the breaking threshold ξ after each failure, which requires calculating the inverse fiber strength CDF $P^{-1}(\cdot)$. However, by interpolating values stored in a function table or by precomputing thresholds, this cost can be reduced to a small number of operations per fracture event.

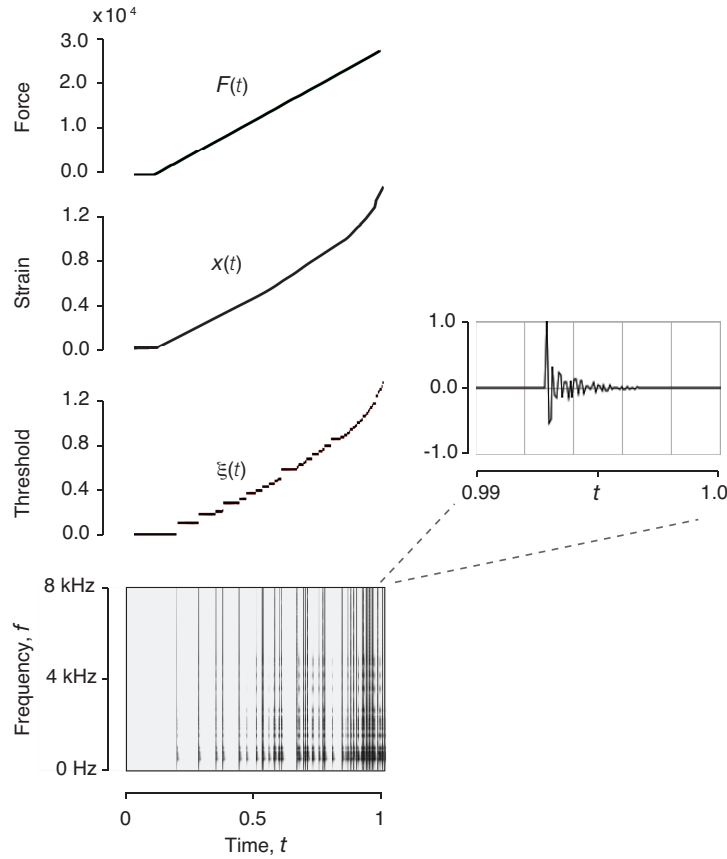


Fig. 7.15 Representative data from the interactive implementation of Fiber Bundle Model M . Data shown corresponds to a model with 350 fibers. Acoustic transfer is simulated by a resonant filter with 10 modes. Left column, Top to Bottom: Force input $F(t)$, strain $x(t)$, threshold $\xi(t)$, and time-frequency spectrogram of acoustic energy of fracture. Right: Fracture event waveform.

The simulation also includes a simple, linear filter model of acoustic transfer in the medium. It is represented by a modal resonant filter with impulse response [59]

$$h(t) = \sum_{i=1}^M A_i e^{-b_i t} \sin(2\pi f_i t). \quad (7.26)$$

Although the resonant filter parameters could, in principle, be precomputed by modeling the material geometry and constitution, we adopted a simpler approach, in which the frequencies f_i are randomly distributed as $p(f) \propto f^\alpha$, where the parameter α controls the

rate of growth of mode density with frequency, which is related to the geometry, dimension, and wave velocity of the propagating medium. The decay factors b_i describe the amount of damping in the material. The amplitudes A_i are chosen to provide a decaying spectrum envelope with $A_i = A_0 f_i^{-r}$. This rate of amplitude decrease with frequency corresponds to a decay of $6r$ dB/octave [85]. By choosing the number N_m of modes, their decay rate r with frequency, and their distribution α appropriately, the acoustic response can be shaped to qualitatively resemble the material of interest (e.g., wood, stone).

7.5 Conclusions

This paper presented algorithms for simulating failure in fiber reinforced composites and granular materials, based on new formulations of the Fiber Bundle Model and Inverse Fiber Bundle Model. A local temporal formulation of random failure evolution was provided through the identification of a stochastic jump process governing failure thresholds. A mean damage approximation was also proposed, offering the possibility to isolate the average stress-strain behavior from the fluctuating response of the model. This construction was empirically found to accurately reproduce the deterministic and stochastic response of the exact algorithm, in the case of the Fiber Bundle Model. In addition, the energy burst distribution obtained here for the Inverse Fiber Bundle agrees with published theoretical and experimental findings. An efficient implementation of these algorithms, suitable for interactive simulation, was also described. As the underlying model is temporal in nature, spatial degrees of freedom are not represented. However, the result can be regarded as an approximate model of temporal fluctuations (e.g., energy bursts, strain fluctuations, or acoustic emissions) during the dynamic loading of a quasi-brittle, heterogeneous medium.

Future work Although these results were obtained under the simplified assumption of global load sharing, the essential properties that facilitated time-domain descriptions of these systems are related to the sequential nature of failure in fiber composites, and these are still present if local load distribution is accounted for [11]. Similarly, individual fibers need not necessarily be considered to respond linearly. These cases will be investigated in future work.

This work could also be extended to address the interactive simulation of high-frequency fracture processes in a volume of a distributed granular or other heterogeneous medium

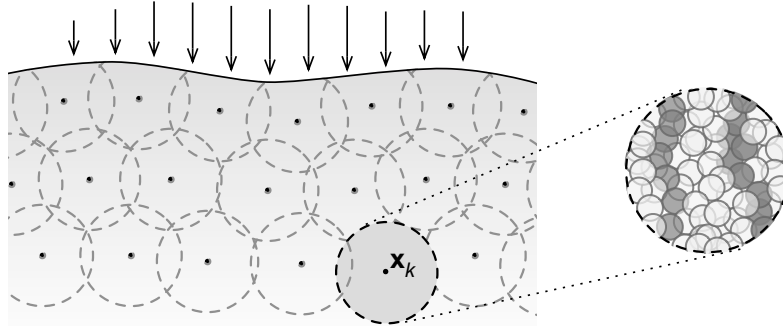


Fig. 7.16 The algorithms presented here may be amenable to the simulation of high-frequency failure processes in distributed media at interactive rates, by virtue of the separation they provide between the slower, homogenized volumetric response and the rapid fluctuations, which can be represented through local, stress-driven fracture processes associated with points \mathbf{x}_k .

(Fig. 7.16). This could, in principle, be facilitated by the mean damage approximation. In a distributed setting, the averaged nonlinear strain response (Equation (7.23) for the inverse Fiber Bundle Model) could, instead, be obtained from a homogenized continuum mechanics model of the constitutive behavior of the distributed medium, which can be simulated using finite element, elastic mesh, or point cloud based algorithms. Local fluctuations could then be synthesized by associating independent instances $\xi_k(t)$ of the breaking threshold process to points \mathbf{x}_k associated with effective volume elements defined by finite elements or by point based radial basis functions $\Phi_i(\mathbf{x})$. Conditions for fracture in the local bundle could be obtained from a measure of maximal strain obtained from the strain matrix $\boldsymbol{\varepsilon}$, similar to criteria used to nucleate and grow cracks in physics-based fracture animation for computer graphics [92, 91, 209]. Since the constitutive behavior is relatively smooth, this part of the simulation can be integrated at a lower rate than is used to render inelastic fluctuations accompanying fracture. However, this remains to be investigated in future work.

Chapter 8

A first passage time problem associated with stick-slip oscillations

Preface to Chapter 8:

This chapter investigates another fundamental category of complex physical interactions with materials encountered in many natural and man-made environments, in the form of shear sliding interactions. It analyzes the statistics of slip events in patterns of irregular stick-slip oscillations that accompany frictional sliding on, or compression of, rough or disordered surfaces, using methods from stochastic physics. The results provide a rich quantitative and qualitative portrait of stick-slip motion in different sliding regimes that can be observed in real or simulated frictional systems. In the context of virtual foot-ground interactions, they may be used to introduce material-dependent temporal irregularities in event-based algorithms for the haptic synthesis of stick-slip motion [218, 219]. However, the results presented in this chapter are relevant to a wider range of research in engineering and physics related to sliding friction dynamics and to friction-induced vibration and sound.

Abstract Frictional stick-slip motion occurs in diverse physical systems, and the oscillations that accompany it are typically pseudo-periodic or irregular, due to effectively random components in the friction force. This chapter is concerned with predicting statistical distributions of periods, sliding displacements, and slip durations for a family of stochastic sliding friction models. To this end, a novel first passage time problem associated with frictional stick-slip oscillations is formulated, and approximate solutions are developed using an asymptotic expansion due to Stratonovich [220]. A Langevin sliding friction model is used to evaluate the analytical predictions. The results of Monte Carlo simulations confirm the approximate validity of those predictions over a wide range of parameters. This system exhibits rich, pseudo-periodic motions that are not present in the deterministic limit, but are stimulated by the presence of noise, as reflected in the statistical distributions investigated here.

8.1 Introduction

Stick-slip oscillations are observed in diverse frictional settings: during macroscopic sliding friction between solid surfaces, such as vehicle brakes [221]; in the excitation of a violin string by the bow [222]; in nanoscale friction between a probe and surface atoms on an atomic substrate [223, 224]; or in the compression or shear response of a granular material [16, 13]. The pattern of these cyclic transitions between sticking and sliding between two surfaces is characteristic of the material properties, contact interfaces, and forces on the system. Stick-slip oscillations are an important source of vibration and acoustic emissions in natural and man-made mechanical systems, and a large amount of engineering research has been devoted to controlling them.

Although phenomenological models of sliding friction may be expressed in terms of mean velocities, effectively averaging over temporal and spatial variations, real friction depends on localized contact between surfaces (necessarily rough) at multiple asperities. For metals, these are superficial irregularities on the order of a few μm in size. Sliding motion results in the collision of many such asperities per second, which can be thought of as a source of noise, giving the forces a random character. In some cases the random components predominate, as in sliding on dry granular media, which is accompanied by large shear stress fluctuations [16, 15, 14, 12]. In both solid and granular friction, multiple velocity- and mass-dependent sliding regimes are observed, exhibiting irregular stick-slip

motion, periodic stick-slip oscillation, and continuous sliding [225, 16, 15], and the slip distances, force fluctuations, and slip time intervals are found to be broadly distributed, so that the regular motion predicted by deterministic friction-velocity relationships exists only in an averaged sense. While several stochastic models have been proposed to describe granular [13] and solid friction [225, 226, 221, 227, 228], as yet, no theoretical description is able to account for the complexity of oscillatory behavior observed within or between different regimes.

The goal of the present work is to explain the influence of dynamical parameters and noise characteristics on the distribution of periods, slip durations, and slip displacements in stochastic models of sliding friction. We associate these distributions with solutions of a first passage time problem associated with the velocity variable of a sliding friction system. The *first passage time* of a stochastic process refers to the length of time required for it to surpass a designated value for the first time. Determining the distribution of first passage times of such a process encompasses an important category of problems in stochastic physics [229].

While the physical setting of interest to this paper has not been directly addressed in prior literature, Lima et al. investigated a related problem, concerning the distribution of distances traveled by a block sliding on an inclined plane before it comes to rest [226]. They successfully explained prior experimental findings of Brito and Gomes [230] by means of a simple stochastic friction law, which could be expressed as a biased diffusion. The sliding distance distribution was obtained by solving a first passage time problem for the block's terminal displacement, using the Fokker-Planck equation [226].

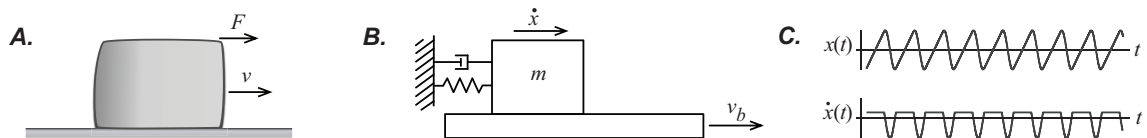


Fig. 8.1 A. A viscoelastic body sliding across a surface, an example of a system that exhibits frictional stick-slip oscillations, behavior that can be captured via B. a simple mechanical model, comprising a block, spring, damper, and sliding surface. C. When the velocity is below a critical value, the system oscillates from a sliding state, when the spring-damper force exceeds that supplied by static friction, to a sticking state, when the relative velocity is zero. At high velocities, continuous sliding motion is observed.

In the case of present interest, the presence of oscillatory dynamics makes it impossible to derive statistical descriptions of the motion from analytical solutions of the Fokker-Planck equation, using known techniques. Instead, in Section 8.2.1, approximate solutions are developed, and expressed in terms of slip-to-stick transition probabilities, using an asymptotic expansion originally due to Stratonovich [220]. This approach was motivated by research of Verechtaguina et al. on the distribution of firing intervals in resonant neuron models [231]. Section 8.3 presents analytical results for a linear Langevin stick-slip friction model, and compares these with estimates obtained by direct Monte Carlo simulation. The slip-times in this model are broadly distributed and evidence transitional behavior from periodic to irregular motion. They also predict other phenomena, such as the occurrence of sub-harmonic peaks in the distribution of oscillation periods, that are characteristic of stochastic resonance phenomena appearing in many bistable dynamical systems subjected to noise [232].

8.2 Stick-slip motion as a first passage time problem

In a simple solid friction model based, for example, on the Coulomb-Amontons law the period τ of oscillation is a single-valued function of velocity, mass, and other system parameters, equal to the sum of time spent in stick and slip phases, $\tau = T_{st} + T_{sl}$. In the reference frame of the sliding surface (Fig. 8.1), the oscillatory motion can be described as follows.

1. A stick-slip transition occurs when the spring-damper force exceeds the maximum force of static friction, at a point (x_0, v_b) in the phase space of the system (Fig. 8.2A), where v_b is the velocity of the sliding surface.
2. Sliding motion follows, until time T_{sl} , when $v(t) = v_b$, at which point the block is stationary with respect to surface.
3. Slip onset recurs after a time T_{st} , when $(x, v, t) = (x_0, v_b, \tau)$, and the cycle repeats.

Such regular motion is observed at low velocities in real systems, including some involving highly disordered materials [16]. When additional effects, such as contact aging or coupling of normal and tangential forces, become important, more complex oscillatory motion is observed, including multiple resonant oscillation periods at discrete frequencies (Fig. 8.2B). The addition of even small random forces during sliding results in growing state uncertainty

following slip onset (Fig. 8.2C), leading to a finite-width distribution $p(\tau)$ of oscillation periods τ . Here, we investigate how this distribution varies with the noise characteristics and dynamics of a class of friction models.

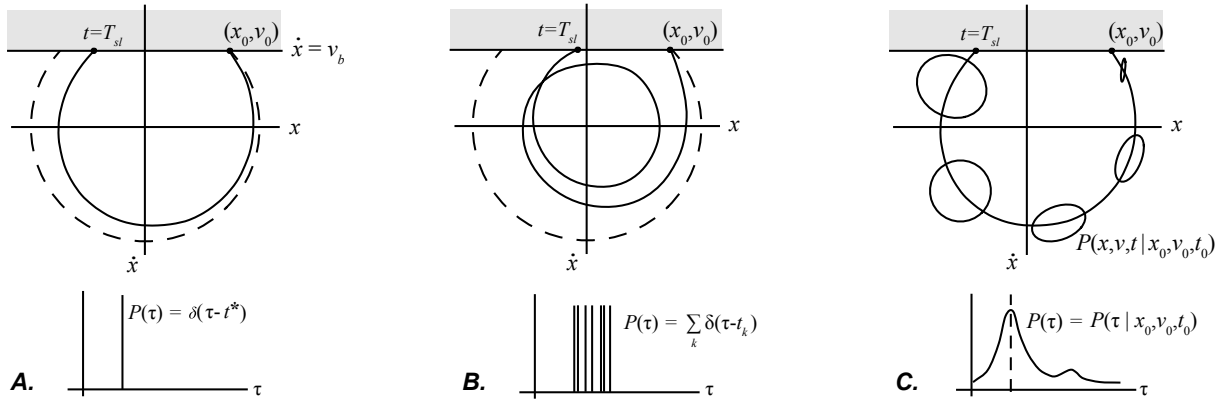


Fig. 8.2 Phase-space portraits for three model friction laws. A. Periodic phase-space orbit produced by a system conforming to a simple friction law. B. Oscillation in a friction model that incorporates multiple degrees of freedom or nonlinearities. C. Noise in a stochastic friction model, leading to a finite-width distribution $\mathcal{F}(T)$ of periods. At slip onset the state of the system is localized near (x_0, v_0) , and is subsequently described by a probability distribution $P(x, v, t | x_0, v_0, t_0)$ that spreads out in time. The ellipsoids represent level sets of P at successive times.

For the remainder, we consider models of stochastic friction that are assumed to have deterministic limits with stick-slip oscillatory regimes. Sliding motion is assumed to be governed by a continuous time Markov process:

$$\dot{\mathbf{x}} = f(\mathbf{x}(t); \eta(t)), \quad (8.1)$$

where η is a random process (the noise source), $f(\cdot)$ describes the sliding dynamics, and the vector $\mathbf{x}(t) = (x, v = \dot{x}, \dots)$ is meant to account for x , v , and any other required state variables. For simplicity, let $t_0 = 0$. After slip onset, the state distribution is localized near (x_0, v_0, \dots) , and its uncertainty grows over time, as represented via a transition probability density $P(\mathbf{x}, t | \mathbf{x}_0, t = 0)$. The initial displacement x_0 could be considered to have a random component, due to variations in local contact strength, but we ignore this possibility here, and focus on the distribution of periods of the motion $p(T | \mathbf{x}_0, 0)$, assuming a reset to sharp

initial conditions (x_0, v_0) at each slip onset.

A transition from slip to stick occurs at time T_{st} when $v(T_{st}) = v_b$. Let $\mathcal{F}(x, t)$ be the probability density for a slip to stick transition to occur at displacement x and time $T_{st} = t$. $\mathcal{F}(x, t)$ is thus the joint density of times at which the sliding motion process first passes the level $v(t) = v_b$ (ensuring stick onset), at the position x . We ignore creep motion, so that T_{st} is a deterministic function of the (random) value of the displacement $x(T_{st})$ at stick onset. The former is given by $T_{st} = (x_0 - x(T_{st}))/v_b$. Since the period of the motion $\tau = T_{st} + T_{sl}$ is the sum of durations spent in the two phases, it is distributed according to

$$p(T|\mathbf{x}_0, 0) = \int_0^T d\tau \mathcal{F}(\hat{x}(\tau), \tau), \quad \hat{x}(\tau) \equiv x_0 - v_b(T - \tau). \quad (8.2)$$

The slip duration T_{sl} and sliding displacement $d = x_0 - x(T_{sl})$ are distributed according to the marginal densities

$$p(T_{sl}) = \mathcal{F}(t = T_{sl}) = \int_{-\infty}^{\infty} dx \mathcal{F}(x, t) \quad (8.3)$$

$$p(d) = \mathcal{F}(x = x_0 - d) = \int_0^{\infty} dt \mathcal{F}(x, t) \quad (8.4)$$

where $p(d)$ is the probability density of slip displacements. Computing the densities $\mathcal{F}(x, t)$, $\mathcal{F}(x)$ and $\mathcal{F}(t)$, which are characteristic of the random stick-slip behavior of the system, requires determining the distribution of first passages of the velocity v across the value v_b , which is equivalent to solving a first passage time problem in the variable v [229].

Such problems are conventionally formulated via a Fokker-Planck partial differential equation governing the transition probability density function $P(\mathbf{x}, t) \equiv P(\mathbf{x}, t|\mathbf{x}_0, t_0)$. For the Langevin system studied in Section 8.3, it has the form [233]

$$\frac{\partial P}{\partial t} = -v \frac{\partial P}{\partial x} + U'(x) \frac{\partial P}{\partial v} + \gamma \left[\frac{\partial P}{\partial v} v P + \frac{\partial^2 P}{\partial v^2} \right] \quad (8.5)$$

with potential $U(x) = kx^2$. The required densities can be obtained from solutions of this equation in the presence of an absorbing boundary condition at $v = v_b$ [233, 229]:

$$P(x, v_b, t) = 0 \text{ with } \partial P(x, v_b, t)/\partial v > 0. \quad (8.6)$$

However, solution methods are known only for limiting cases, in which the motion is highly damped [234], the relaxation time is much shorter than the asymptotic escape time (defined in Section 8.3), or the dynamics can otherwise be reduced to a Brownian motion in a single variable (Smoluchowski approximation [235]).

The approach adopted below, based on an asymptotic expansion due to Stratonovich [220], was inspired by recent work of Verechtaguina et al. on the discharge rate of a resonant, spiking neuron model [236, 231]. The problem they treated involved first passage in the displacement variable $x(t)$ rather than velocity $v(t)$, as is relevant here. This complicates the integrals that arise, but interesting analytic approximations are possible. We first address the density $\mathcal{F}(T)$ of slip times, then treat the slip distance and oscillation period.

8.2.1 Approximate slip time densities

A set of approximations to the first passage time density $\mathcal{F}(T)$ for the slip duration can be developed, based on the following asymptotic expansion involving crossing time densities of the sliding mode dynamics [220, 231]:

$$\mathcal{F}(T) = \sum_{p=0}^{\infty} \frac{(-1)^p}{p!} \int_0^T dt_1 \cdots \int_0^T dt_p n_{p+1}(t_1, t_2, \dots, T). \quad (8.7)$$

The first term, $n_1(T)$, is the density of all upcrossings at time T . An upcrossing is a passage of the system state trajectory across the boundary $v = v_b$ from below. Thus, $n_1(t)dt$ is the probability that $v(t) < v_b < v(t + dt)$. This represents a slip-to-stick transition. This probability density depends on the sliding mode dynamics, noise distribution, and initial state, as will be elaborated in Section 8.2.3. Since multiple upcrossings are possible, $n_1(T)$ is not normalized to one, and diverges on long time scales. The terms $n_k(t_k, t_{k-1}, \dots, t_1)$ represent the joint densities of $v(t)$ performing upcrossings at the set of k times indicated.

The partial sums of Equation (8.7) can be regarded as successive approximations to $\mathcal{F}(T)$ [236]. The first, $\mathcal{F}_n^{(1)}(T) = n_1(T)$, overestimates by including all trajectories that crossed at time T , and not only those that crossed for the first time at T . The two-term estimate, $\mathcal{F}_n^{(2)}(T)$ adds a correction term accounting for all trajectories that performed one

upcrossing prior to time T :

$$\mathcal{F}_n^{(2)}(T) = n_1(T) - \int_0^T n_2(t_1, T) dt_1. \quad (8.8)$$

$\mathcal{F}_n^{(2)}(T)$ can be shown to overcompensate for trajectories with more than one upcrossing before T , leading to further approximations.

A second family of approximations is obtained by viewing $\mathcal{F}(T)$ as the waiting-time density for the set of upcrossing times t_k (Fig. 8.3), and developing a cumulant expansion associated with that of Equation (8.7) [235, 220]. Let $S(T)$ be defined by

$$\mathcal{F}(T) = \dot{S}(T)e^{-S(T)}. \quad (8.9)$$

The quantity $\dot{S}(T) = dS(T)/dT$ can be interpreted as a time-dependent escape (slip-to-stick) rate. Cumulant expansion functions g_k may be defined via

$$S(T) = - \sum_{p=1}^{\infty} \frac{(-1)^p}{p!} \int_0^T \cdots \int_0^T g_p(t_1, \dots, t_p) dt_1 \cdots dt_p. \quad (8.10)$$

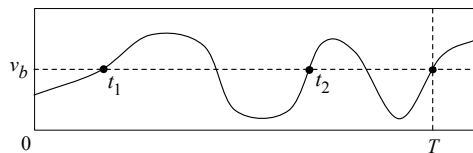


Fig. 8.3 The upcrossings of $v(t)$ may be viewed as a stochastic point process, whose sample space consists of k -tuples of upcrossing times, $0 < t_1 < t_2 < \dots < t_k < \infty$, and whose distribution functions are given by the joint upcrossing densities $n_k(t_1, t_2, \dots, t_k)$ of v .

In light of (8.9), the densities g_k are related to the n_k through:

$$\begin{aligned}
 n_1(t_1) &= g_1(t_1) \\
 n_2(t_1, t_2) &= g_2(t_1, t_2) + g_1(t_1)g_1(t_2) \\
 n_3(t_1, t_2, t_3) &= g_3(t_1, t_2, t_3) + g_1(t_1)g_2(t_2, t_3) + g_1(t_2)g_2(t_1, t_3) \\
 &\quad + g_1(t_3)g_2(t_1, t_2) + g_1(t_1)g_2(t_2)g_3(t_3) \\
 &\quad \vdots
 \end{aligned} \tag{8.11}$$

The advantage of this representation is that if the crossing times t_k occur independently, all g_k for $k > 1$ vanish. If the points are assumed to occur almost independently, then the g_k will decrease rapidly in magnitude [235]. Thus, replacing $S(T)$ by its partial sums in Eq. (8.10), corresponds to an approximation in which the upcrossing times nearly decouple. From the relations (8.11), this is equivalent to replacing the joint upcrossing distributions n_k of each order k by a product of one point distributions n_1 . When $g_2(t_1, t_2) = 0$, it therefore follows that $n_2(t_1, t_2) = n_1(t_1)n_2(t_2)$, and likewise for $k > 2$. This leads to a first order decoupling approximation, $\mathcal{F}_g^{(1)}(T)$, in which all higher order densities are approximated via n_1 . The terms in the infinite sum of Equation (8.7) then form an exponential series, yielding

$$\mathcal{F}_g^{(1)}(T) = n_1(T) \exp\left(-\int_0^T n_1(t)dt\right). \tag{8.12}$$

Higher-order decoupling approximations $\mathcal{F}_g^{(k)}(T)$ can also be defined [231]. Unlike the truncations of Eq. (8.7), they are normalized for all positive times, due to the form of Equation (8.9).

8.2.2 Joint first passage densities

The foregoing approximations can be readily extended to the case of the joint density $\mathcal{F}(x, T)$, which describes the infinitesimal probability for a slip-to-stick transition to occur at position x and time T . Equation (8.7) generalizes to

$$\mathcal{F}(x, T) = \sum_{p=0}^{\infty} \frac{(-1)^p}{p!} \int_0^T dt_1 \int_{-\infty}^{\infty} dx_1 \cdots \int_0^T dt_p \int_{-\infty}^{\infty} dx_p n_{p+1}(x_1, t_1; x_2, t_2; \dots; x, T). \tag{8.13}$$

The joint upcrossing densities n_k in x and t describe the joint density of $v(t)$ performing an upcrossing at the intermediate times t_1, t_2, \dots, t_k and positions x_1, x_2, \dots, x_k . As above, truncation approximations $\mathcal{F}_n^{(k)}(x, T)$ are obtained by retaining a finite number of terms in the sum, with $\mathcal{F}_n^{(1)}(x, T) = n_1(x, T)$ being the first order estimate. Decoupling approximations are obtained by assuming that the intermediate crossings (x_k, t_k) occur approximately independently. Assuming full independence, the higher order crossing densities can be expressed in terms of $n_1(x, t)$, and the infinite series in Equation (8.13) forms an exponential sum, yielding

$$\mathcal{F}_g^{(1)}(x, T) = n_1(x, T) \exp\left(-\int_0^T n_1(t) dt\right). \quad (8.14)$$

where the marginalization property $n_1(T) = \int_{-\infty}^{\infty} n_1(x, T) dx$ was used to simplify the exponent.

Oscillation period density The probability density for the oscillation period was determined in (8.2) to be given by

$$p(\tau = T) = \int_0^T d\tau \mathcal{F}(\hat{x}, \tau), \quad \hat{x} \equiv x_0 - v_b(T - \tau). \quad (8.15)$$

It can be estimated by substituting the approximations for $\mathcal{F}(x, T)$ obtained above.

Slip length density Slip length is given by $d = x_0 - x_{sl}$, where $x_{sl} = x(T_{sl})$ is the displacement at stick onset. The density governing the latter is obtained by marginalizing $\mathcal{F}(x, T)$ over time, yielding

$$p(d = x_0 - x) = \int_0^{\infty} dT \mathcal{F}(x, T). \quad (8.16)$$

Since this involves an integral over all time, the non-normalized estimates $\mathcal{F}_n(x, T)$ may not be used without further normalization in time (for example, by defining them to be zero for $T > T^*$ for suitable T^*). However, the decoupling approximations may be directly applied to estimate $p(d)$.

8.2.3 Upcrossing densities

In order to compute the distributions of interest for a particular friction model, expressions for the upcrossing densities n_k are needed. To facilitate this, a simplifying assumption is made that the sliding mode dynamics constitute a Markov process in variables (x, v) , with additive noise, described by

$$\dot{v}(t) = f(x(t), v(t)) + \eta(t), \quad \dot{x}(t) = v(t), \quad \dot{v}(t) = a(t). \quad (8.17)$$

Motivation for assuming an additive noise term is provided in the next section.

For an upcrossing to occur at a time $t > t_0$, the velocity should lie in the range $v_b - a dt < v(t) < v_b$. The probability for this to occur is

$$\int_{v_b - a dt}^{v_b} dv P(x, v, a, t | x_0, v_0, t_0) = |a| P(x, v_b, a, t | x_0, v_0, t_0) dt. \quad (8.18)$$

$P(x, v, a, t | x_0, v_0, t_0)$ is the conditional probability density for the process to be at (x, v, a) at time t . It can be expressed as:

$$\begin{aligned} P(x, v, a, t | x_0, v_0, t_0) &= P(x, v_b, t | x_0, v_0, t_0) P(a | x, v_b, t, x_0, v_0, t_0) \\ &= P_{10} P(a | x, v_b), \end{aligned} \quad (8.19)$$

where the first factor, $P_{10} \equiv P(x, v, t | x_0, v_0, t_0)$ is the transition probability density. The conditional distribution of $a(t)$ appearing in the second factor depends only on x and v , because it is fully determined at any time t by Equation (8.17). It has a mean given by $\mu_a(t) = f(x(t), v_b(t))$, with a distribution about this mean given by that of the noise process $\eta(t)$.

Since $a > 0$ is required for an upcrossing, $n_1(x, v_b, t)$ is obtained by integrating Equation (8.18) over all values of $a > 0$:

$$\begin{aligned} n_1(x, v_b, t) &= \int_0^\infty da a P(x, v_b, a, t | x_0, v_0, t_0) \\ &= P_{10} \int_0^\infty da a P(a | x, v_b) \equiv P_{10} I_a(x, v). \end{aligned} \quad (8.20)$$

The density $n_1(t)$ of upcrossings across the entire boundary $v = v_b$ is thus

$$n_1(t) = \int_{-\infty}^{\infty} dx P(x, v_b, t | x_0, v_0, t_0) I_a(x, v_b). \quad (8.21)$$

Similarly, $n_2(t_1, t_2)$ can be demonstrated to be given by

$$n_2(t_1, t_2) = \int_{-\infty}^{\infty} dx_1 P_{10} I_{a_1}(x_1, v_1) n_1(t_2 | x_1, v_1, t_1). \quad (8.22)$$

where $n_1(t_2 | x_1, v_1, t_1)$ is the upcrossing density from an initial state (x_1, v_1, t_1) . The k th density, n_k , is given by a similar integral, with factors like those that appear in n_1 and n_2 together with the joint upcrossing densities of lower order.

8.3 Stick-slip motion in a Langevin friction model

As an illustrative example, consider a system undergoing stick-slip motion, with sliding dynamics corresponding to a damped harmonic oscillator driven by additive, Gaussian noise. It is described by the Langevin equation:

$$\dot{x} = v, \quad a = \dot{v} = -\omega_0^2 x - \zeta v + \eta(t). \quad (8.23)$$

Here, the random force $\eta(t)$ is assumed to be Gaussian white noise, with $\langle \eta(\tau)\eta(\tau+t) \rangle = 2D\delta(t)$, but analogous results can be obtained with colored noise. This equation has been used to model experimentally observed sliding friction in the presence of noise generated via collisions with surface asperities or particles [225, 13]. Although surface noise will generally be velocity and history dependent during sliding, Johansen et al. found that omitting this dependence did not degrade the ability of their model to explain experimental observations of a solid friction system during continuous sliding [225].

As the system (8.23) is linear and the noise is Gaussian, the transition probability density $P_{10} = P(x, v, t | x_0, v_0, t_0)$ is a bivariate Gaussian process. The explicit solution in the free-sliding regime is well-known [237, 238]. The mean trajectories $\mu_x(t)$ and $\mu_v(t)$ of P_{10} are given by the equations of motion for the damped harmonic oscillator:

$$\mu_x(t) = Ae^{-\zeta t} \sin(\omega_1 t + \phi), \quad \mu_v(t) = d\mu_x/dt \quad (8.24)$$

with angular frequency $\omega_1^2 = \omega_0^2 - \zeta/4$. The initial conditions are fixed through the initial amplitude A and phase angle ϕ , which depend on x_0 and v_0 . The variances are

$$\begin{aligned}\Sigma_{xx} &= w_0^2 f_+(t) \\ \Sigma_{vv} &= f_-(t) \\ \Sigma_{xv} &= D\omega_1^2 e^{-\zeta t} \sin(\omega_1 t)^2\end{aligned}\quad (8.25)$$

where the functions $f_{\pm}(t)$ are given by

$$f_{\pm}(t) = \frac{D}{\zeta} \left(1 - \omega_1^{-2} e^{-\zeta t} (\omega_1^2 + \frac{1}{2} \zeta^2 \sin(\omega_1 t)^2 \pm z\omega_1 \sin(\omega_1 t) \cos(\omega_1 t)) \right). \quad (8.26)$$

8.3.1 Upcrossing density

From Equation (8.20), the upcrossing density $n_1(x, v_b, t)$ across velocity barrier $v = v_b$ is

$$n_1(x, v_b, t) = P_{10} I_a(x, v) = P_{10} \int_0^{\infty} da a P(a|x, v_b) \quad (8.27)$$

The conditional distribution $P(a|x, v_b)$ for the acceleration is fully determined by Eq. (8.23), and has the form of a Gaussian probability distribution, $P(a|x, v_b) = N(a; \mu_a, \sigma^2)$, with a mean given by $\mu_a = -\omega_0^2 x - \zeta v$, and variance $\sigma^2 = 2D$. One can compute that

$$I_a(x, v) = \int_0^{\infty} da a N(a; \mu_a, \sigma^2) \quad (8.28)$$

$$\begin{aligned}&= \sqrt{\frac{\sigma^2}{2\pi}} \exp\left(-\frac{\mu_a^2}{2\sigma^2}\right) - \frac{\mu_a}{2} \operatorname{erfc}\left(\frac{\mu_a}{\sqrt{2}\sigma}\right), \\ &\equiv I_{a,1}(x, v) + I_{a,2}(x, v).\end{aligned}\quad (8.29)$$

The upcrossing density $n_1(T)$ is given as in Eq. (8.21):

$$n_1(T) = \int_{-\infty}^{\infty} dx P_{10}(x, v_b, T) I_a(x, v_b). \quad (8.30)$$

The first factor, the transition probability density P_{10} , is a Gaussian function of the integration variable x . An analytic expression for $n_1(T)$ can be obtained as follows. The

product $P_{10}I_{a,1}$ is a bivariate Gaussian function of $\mathbf{x} = (x, v)$. One can write:

$$\begin{aligned} P_{10}(x, v) &= N(\mathbf{x}; \mu, \Sigma) \\ I_{a,1}(x, v) &= \sqrt{\frac{\sigma^2}{2\pi}} \exp\left(-\frac{1}{2}\mathbf{x}^t S \mathbf{x}\right) \end{aligned} \quad (8.31)$$

where N is the bivariate Gaussian (normal) distribution and

$$\mu = (\mu_x \ \mu_v)^t \quad (8.32)$$

$$\Sigma = \begin{pmatrix} \Sigma_{xx} & \Sigma_{xv} \\ \Sigma_{xv} & \Sigma_{vv} \end{pmatrix} \quad (8.33)$$

$$\Sigma^{-1} \equiv \begin{pmatrix} C_{xx} & C_{xv} \\ C_{xv} & C_{vv} \end{pmatrix} = C \quad (8.34)$$

$$S = \begin{pmatrix} \omega_0^4 & \omega_0^2 \zeta \\ \omega_0^2 \zeta & \zeta^2 \end{pmatrix} \sigma^2 \quad (8.35)$$

The equations of motion for the covariances Σ and means μ were given in Section 8.3. However, the result for $n_1(T)$ does not depend on their explicit form, but only on the linearity of the system, the additive, Gaussian nature of the noise, and the sliding mode barrier $v = v_b$.

The integrand $P_{10}I_{a,1}$ is a product of bivariate Gaussian functions, which can be written as

$$P_{10}(x, v, t)I_{a,1}(x, v) = \tilde{Z}N(\mathbf{x}; \tilde{\mu}, \tilde{\Sigma}), \quad (8.36)$$

with

$$\tilde{Z} = \frac{\sigma}{\sqrt{2\pi}} |1 + \Sigma S|^{-1/2} \exp\left(-\frac{1}{2}\mu^t Q \mu\right) \quad (8.37)$$

$$\tilde{\Sigma} = (\Sigma^{-1} + S)^{-1} \quad (8.38)$$

$$Q = S(1 + \Sigma S)^{-1} \quad (8.39)$$

$$\tilde{\mu} = \tilde{\Sigma}\Sigma^{-1}\mu \quad (8.40)$$

The integral over x then gives

$$\int_{-\infty}^{\infty} dx P_{10} I_{a,1} = \tilde{Z} N(v; \tilde{\mu}_v, \tilde{\Sigma}_{vv}). \quad (8.41)$$

The second factor in the integral for $n_1(t)$ is $P_{10}(x, v) I_{a,2}(x, v)$, which is the product of a Gaussian function of x and a complementary error function. Carrying out the integral yields

$$\int_{-\infty}^{\infty} dx P_{10} I_{a,2} = Z' \left(n\sqrt{\pi} \operatorname{erfc}(nq) + (q^{-2} - 1)e^{-n^2q^2} \right) \quad (8.42)$$

with:

$$Z' = \frac{\sigma |2\pi\Sigma|^{-1/2}}{2\sqrt{C_{xx}}} \exp\left(-\frac{1}{2}(v - \mu_v)^2 C_{vv}\right) \quad (8.43)$$

$$n = \frac{\sqrt{2}}{\sigma} \left(v \left(\zeta - \frac{C_{xv}}{C_{xx}} \omega_0^2 \right) + \mu_x \omega_0^2 \right) \quad (8.44)$$

$$q = \left(1 + \frac{4\omega_0^4}{\sigma^2 C_{xx}} \right)^{-1/2}. \quad (8.45)$$

The expression for the first upcrossing density $n_1(t)$ is thus

$$n_1(t) = \tilde{Z} N(v; \tilde{\mu}_v, \tilde{\Sigma}_{vv}) + Z' \left(n\sqrt{\pi} \operatorname{erfc}(nq) + (q^{-1} - q)e^{-n^2q^2} \right). \quad (8.46)$$

Higher order joint upcrossing densities can also be reduced to multiple integrals involving factors that are linear, Gaussian, and of Error Function type in the variables of integration. Although complex, they can be computed via repeated numerical integration.

$n_1(T)$ is used to compute the first-order truncation and cumulant approximations, $\mathcal{F}_n^{(1)}(T) = n_1(T)$ and $\mathcal{F}_g^{(1)}(T) = n_1(T) \exp(-\int_{-\infty}^{\infty} n_1(T) dt)$. The joint upcrossing density $n_1(x, T)$ of Eq. (8.27) is similarly used to estimate the probability density $p(T)$ of oscillation periods (Eq. (8.15)), and the distribution $p(d)$ of slip displacements (Eq. (8.16)). In the next section, these approximations are evaluated via stochastic simulations.

8.3.2 Results

The analytic approximations for the densities of interest were compared with estimates obtained by Monte Carlo simulation, based on the stochastic harmonic oscillator system

of Section 8.3. The estimates were computed by integrating the equivalent Itô stochastic differential equation (SDE) in time. Each simulated instance was numerically integrated using the Euler-Maruyama method, beginning from the starting configuration (x_0, v_0, t_0) until first passage, i.e., until time T at which it reached the boundary $v = v_b$. Figure 8.4 illustrates examples of phase space trajectories until first passage. Each density estimate was based on 10^5 to 10^6 simulation runs. The integration time step was $h = 0.002$, and other parameters were as noted in the figure captions.

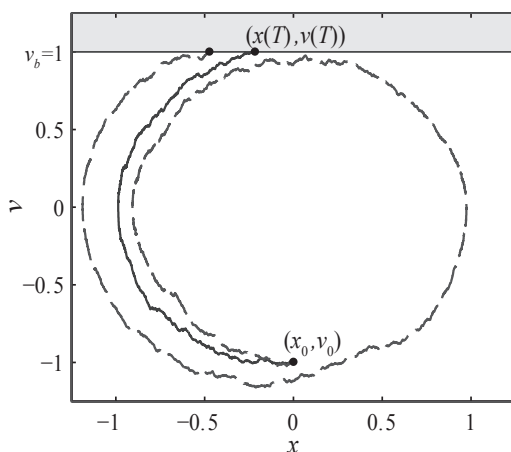


Fig. 8.4 Two phase space trajectories $(x(t), v(t))$ for the stochastic harmonic oscillator system, simulated by numerical integration of the equivalent SDE from a localized initial state $(x_0(t), v_0(t))$ until the time T of first passage, $v(T) = v_b$. The solid line trajectory belongs to the fundamental mode of stick-slip oscillation with mean frequency ω' , and the dashed line to an oscillation with approximate frequency $\omega = \omega'/2$. Parameters are $D = 0.0005, v_b = 1.0, \omega_0 = 1, \zeta = 0.01$. The integration timestep $h = 0.001$.

The evolution of this system can be usefully characterized by three different time scales. The first two are the oscillation period $\tau = 2\pi/\omega_1 = 2\pi/\sqrt{\omega_0^2 - \zeta^2/4}$ and the relaxation time $t_r = 2/\zeta$, which determine the evolution of the mean trajectories. The third time scale, related to relative magnitude of the noise, is

$$T_R = 1/n_0, \quad n_0 = \lim_{T \rightarrow \infty} n_1(T) = \frac{\omega_0}{2\pi} \exp\left(-\frac{v_b \zeta}{2D}\right). \quad (8.47)$$

n_0 is known as the Rice frequency [239], and is associated with the asymptotic mean time between upcrossings, $T_R = 1/n_0$. The values of these three time scales, and that of the

sliding velocity v_b , give rise to qualitative differences in the distributions of interest for this system.

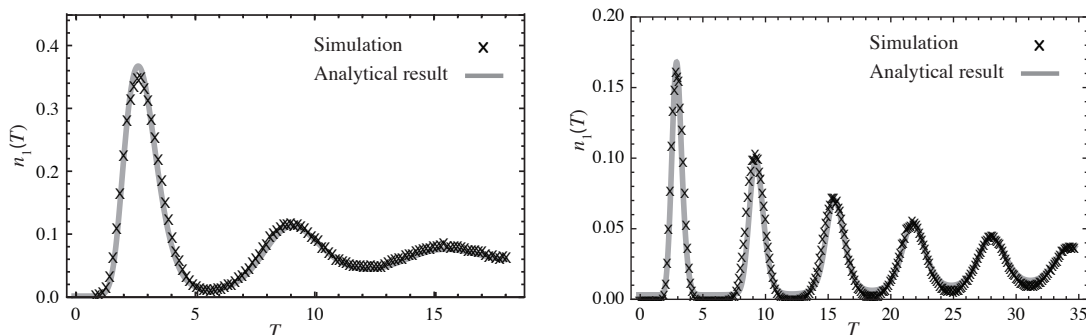


Fig. 8.5 The first upcrossing density, $n_1(t)$, which describes the level crossing behavior of the system in the absence of absorption from to slip-to-stick transitions. The exact analytic result of Equation (8.46) (gray line) is compared with a Monte Carlo estimate (x's). Left: $D = 0.4, v_b = 1.0, x_0 = 0.0, v_0 = -1.0, \omega_0 = 1, \zeta = 0.1$. Right: $D = 0.04, v_b = 1.3, x_0 = 0.3, \omega_0 = 1, \zeta = 0.11$.

Upcrossing density Figure 8.5 compares the analytic result for the upcrossing density $n_1(T)$ (Eq. (8.46)) with the estimate obtained by Monte Carlo simulation, for two different values of the system parameters. The analytic result is in close agreement with the simulation result in both cases. This is as expected, since no approximation was entailed here. The largest maximum of the upcrossing distribution lies close to the value determined by the mean free-sliding trajectory, corresponding to the oscillation period τ .

Slip duration The distribution of slip durations is given by the first passage time density $\mathcal{F}(T)$. Figure (8.6) compares the two approximations with results of simulations. The first, $\mathcal{F}_n^{(1)}(T) = n_1(T)$, shows good correspondence with the first maximum of $\mathcal{F}(T)$, but overestimates subsequent ones, since $n_1(T)$ also counts all upcrossings after the first. At large times, it overestimates the value of $\mathcal{F}(T)$ by an amount equal to the asymptotic upcrossing frequency n_0 (Eq. (8.47)). The decoupling approximation, $\mathcal{F}_g^{(1)}(T)$, exhibits no such asymptotic error, but, in the example of Fig. 8.6, it underestimates the first maximum and overestimates the second. The relative merits of these approximations in different regimes are extensively analyzed in one of the references [231], so a detailed discussion is omitted here. Figure (8.7) examines the decoupling approximation in different noise and damping

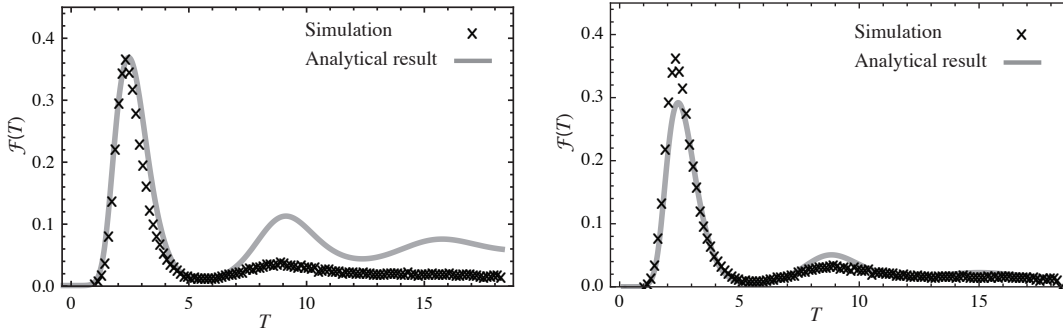


Fig. 8.6 Comparison of two different analytic approximations for the first passage time density. Left: The approximation $\mathcal{F}_n^{(1)}(T) = n_1(T)$ in terms of the upcrossing density is compared with the Monte Carlo estimate of $\mathcal{F}(T)$ (marked as \times). There is good qualitative agreement on the first maximum, but subsequent maxima are overestimated or erroneously included. Right: The same comparison for the decoupling approximation $\mathcal{F}_g^{(1)}(T)$. There is an undershoot of the first maximum and overestimation of the second. Parameters are $D = 0.4$, $v_b = 1.0$, $x_0 = 0.0$, $v_0 = -1.0$, $\omega_0 = 1$, $\zeta = 0.1$.

conditions. The locations and approximate sizes of the maxima are correctly reproduced, despite discrepancies in the high noise conditions. When the oscillation period is significantly longer than the escape time (high noise condition) or when the relaxation time is short (high damping condition), only a single prominent maximum appears (Fig. 8.6).

In the underdamped regime, $t_r > \tau$, when the noise level D is moderate, it can happen that a trajectory of the stochastic dynamical system “misses” a slip-to-stick transition on one oscillation cycle, but achieves it on the next. Those that pass N cycles of the motion before crossing contribute to a peak of the temporal distributions with mean period $N\tau$ (e.g., Fig. 8.5, right panel). In the present example, although they occur at subharmonic frequencies of the fundamental period, they are randomly spaced in time, so do not contribute to any stationary subharmonic mode of oscillation. Similarly, in the high-velocity regime, where stick-slip oscillations would not manifest in the deterministic limit, they can occur randomly in the presence of noise, as evidenced here by the appearance of peaks in the temporal distributions. Further discussion is provided below.

Oscillation period and stochastic resonance The distribution of oscillation periods, $p(T)$, was computed using Equation (8.15) and the decoupling approximation $\mathcal{F}_g^{(1)}(x, T)$

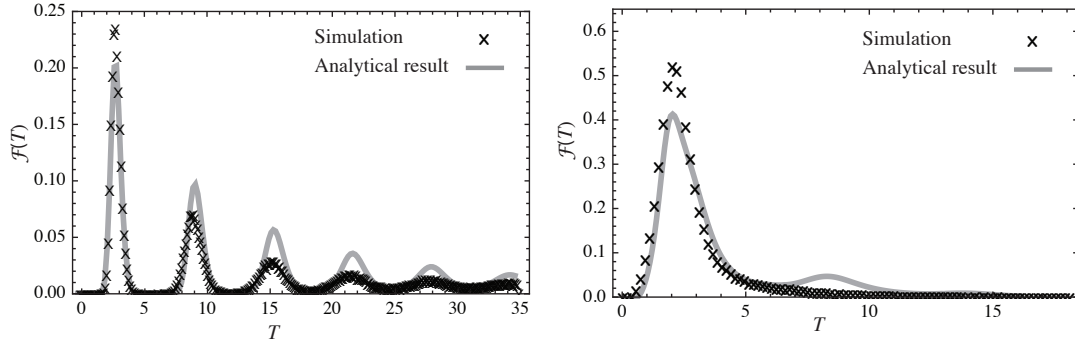


Fig. 8.7 Comparisons of the analytic approximation $\mathcal{F}_g^{(1)}(T)$ with simulation results. Left: $\zeta = 0.11, D = 0.04, v_b = 1.0, \omega_0 = 1, T_R = 3.9$. Right: $D = 0.33, v_b = 1.0, \omega_0 = 1, \zeta = 0.125, T_R = 0.8$.

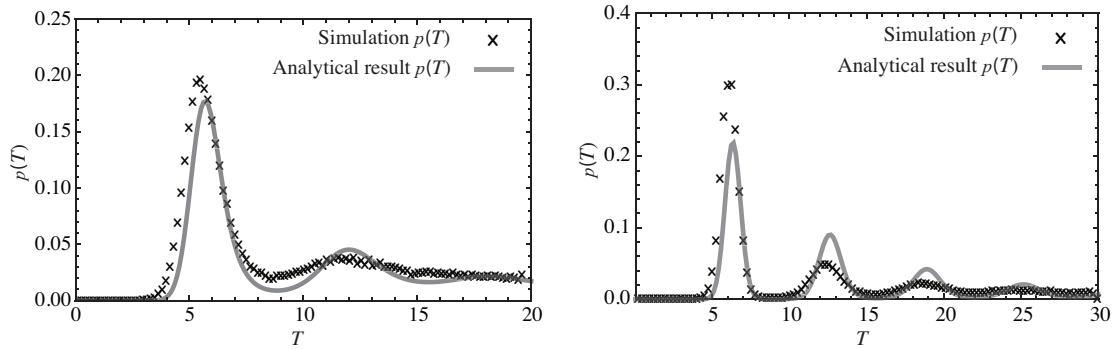


Fig. 8.8 The distribution of stick-slip oscillation periods, $p(T)$. Analytic results were based on the decoupling approximation $\mathcal{F}_g^{(1)}(x, T)$ for the joint first passage density. Left: $\zeta = 0.4, \omega_0 = 1, D = 0.1, v_b = 1.0$. Right: $\zeta = 0.11, \omega_0 = 1, D = 0.04, v_b = 1.0$

for the joint first passage density. The results are qualitatively similar to those for $\mathcal{F}(T)$: At lower values of the damping, there is a decaying sequence of maxima, which are also apparent in the approximation, yielding quasi-periodic oscillations with periods spaced at integer multiples of the free-sliding period. At sufficiently high velocities, they lie at multiples of the fundamental stick-slip oscillation period, since little time is spent in the stick phase, but as mentioned above, they do not correspond to any stationary subharmonic oscillation mode of the system, since they are randomly distributed in time. However, transient subharmonic oscillations do occur in real frictional systems, including stringed

musical instruments [222], and are observed in deterministic friction models that account for dynamical degrees of freedom related to contact area, coupling of normal and tangential oscillation modes, or coupling to other resonant degrees of freedom [221, 240].

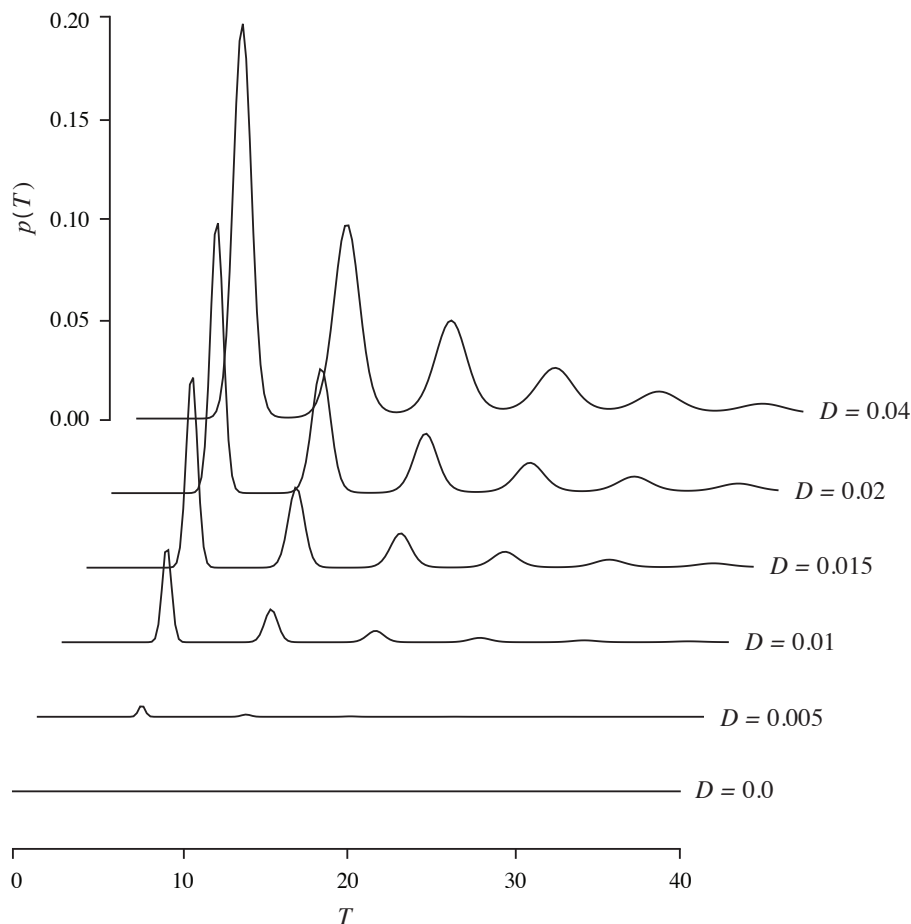


Fig. 8.9 Noise-driven excitation of stick-slip oscillations. The distribution of stick-slip oscillation periods, $p(T)$, is shown for different values of the amplitude, D , evaluated using the analytical decoupling approximation, $\mathcal{F}_g^{(1)}(x, T)$. Other parameters were: $\zeta = 0.11, \omega_0 = 1, v_b = 1.0, x_0 = 0.1$.

These trajectories can be regarded as noise induced attractors, since they are not present in the deterministic limit. The appearance of noise-stimulated peaks in the waiting time distribution of a stochastic dynamical system passing a threshold is one of the characteristic features of stochastic resonance phenomena [232]. Figure 8.9 illustrates its manifestation in the present system in further detail. In the absence of noise, there is not enough energy for

the system to reach first passage (the sliding velocity, v_b , and damping, ζ , being too large). The addition of modest amounts of noise stimulates transient oscillations at a hierarchy of periods subharmonically related to the resonant frequency of the free sliding oscillation mode.

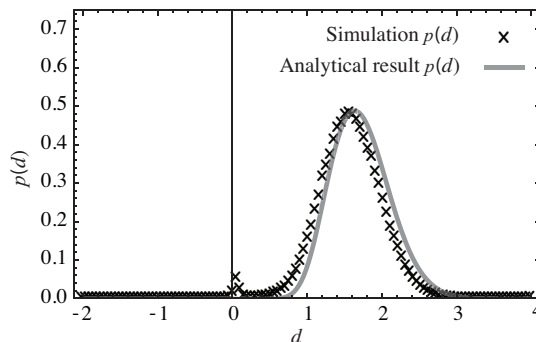


Fig. 8.10 The distribution $p(d)$ of slip displacements: analytical result and Monte Carlo estimate. Here, $\zeta = 0.4, \omega_0 = 1, D = 0.1, v_b = 0.45, x_0 = 0.9$.

Slip displacement For comparison with simulations, the slip displacement distribution was computed via Equation (8.16) using the decoupling approximation for $\mathcal{F}(x, T)$. Figure 8.10 shows a typical example, which also demonstrates good qualitative agreement with simulations. The slip length distribution is found to have an approximately Gaussian shape in all cases examined. The simulation indicates a small non-zero probability for slip displacements near $d = 0$, corresponding to the resumption of sticking immediately after slip onset. Although predicted by the model here, this should be regarded as an unphysical artifact, since transient slip dynamics and presliding displacement effects, which would greatly influence such transitions at the microscopic level, are not accounted for in the simple Langevin friction model.

Although no analytic formula was obtained for them, higher order approximations (based on $\mathcal{F}_n^{(k)}(T)$ and $\mathcal{F}_g^{(k)}(T), k > 1$) can be computed via numerical integration. However, because of the complex form of the equations and the multiple integrals involved, to do so is not more computationally efficient than direct Monte Carlo simulation.

8.4 Conclusion

This chapter presented an investigation of the role of noise in stick-slip oscillations, by formulating a novel first passage time problem for a class of stochastic sliding friction models. Analytical approximations were obtained for the finite-width distributions of the period, slip time, and slip length. The first-order versions of these approximations were evaluated for a sliding friction model based on the Langevin equation, demonstrating close agreement with simulations in some regions of the parameter space, and significant departures, despite qualitative similarity, in others. Higher-order approximations would be expected to provide more accurate results, but the repeated integrals involved must be evaluated numerically, which is not necessarily more instructive or efficient than direct Monte Carlo simulation.

Although these results are promising, further investigation is needed to compare predictions with experimental results on sliding friction or other systems exhibiting stick-slip behavior, and to apply the analytical techniques used here to other models of friction. Furthermore, when noise and damping are modest, it is observed that, in the Langevin friction model, the slip period distribution is well approximated by a mixture of Gaussian distributions centered at multiples of the fundamental period. It may be possible to derive such an approximation as an extension of the results presented here, but this remains to be explored in future work.

Despite these limitations, the results presented here may shed further light on effects of friction noise on stick-slip motion. This type of knowledge is useful in several areas of engineering and physics related to vibration and sound, ranging from noise reduction in vehicle brakes, to the simulation of material responses in virtual reality, or the analysis of bowed musical instruments. The particular distributions derived here could facilitate efficient real-time simulation of friction oscillations in ways that accurately capture the rich, pseudo-periodic motions that manifest in the presence of modest levels of noise.

Chapter 9

Conclusions

This thesis is the first to address the simulation of experiences of walking on virtual ground surfaces via a vibrotactile display and to evaluate the influence of feedback of this type on the perception of ground surfaces. It is also one of the first attempts to investigate haptic rendering of transient, texture-like effects produced during interaction with complex, heterogeneous materials, such as fiber reinforced composites (e.g., fracturing wood) or granular media (gravel, sand). This document provides practical guidelines for the engineering of hardware interfaces, algorithms, and interaction methods, and also provides a physically based characterization of stochastic textures produced through normal and shear interactions with complex, deformable ground surfaces.

9.1 Results

9.1.1 Devices

Four variants of the vibrotactile floor interface were presented, in Chapters 3, 4, 5, and 6. The re-engineered display introduced in Chapter 4 provides a well-characterized platform for presenting controlled vibrotactile stimuli for perceptual or psychophysics experiments. The variable compliance version introduced in Chapter 6 proved to be an effective experimental setup for studying a novel effect of vibrotactile sensory information on the perception of mechanical compliance, and could also be used to explore related effects on the control and kinematics of walking. The distributed floor surface presented in Chapter 5 provides an efficient, reproducible platform for the design of multi-user interactions with

virtual ground surfaces over an extended area.

The decision to restrict the haptic feedback that was supplied to the vibrotactile frequency band greatly simplified and reduced costs associated with this interface. This simplification came at the expense of kinesthetic information that might otherwise be supplied via low frequency force feedback. The latter could be provided by a haptic locomotion interface, such as the Sarcos Biport [53], but costs would be greatly increased and bandwidth severely limited. A better option would be to augment such a kinesthetic locomotion interface with high-frequency vibrations supplied by vibrotactile actuators embedded in the footpads, but this has never, to our knowledge, been attempted.

9.1.2 Information Display and Interaction Techniques

As presented in Chapter 3, vibrotactile communication messages presented through floor surfaces provide an unobtrusive means of displaying ambient information in a wide range of intelligent environments without requiring their users to don any specialized apparel or equipment. They might be used to support activities ranging from assisted living in smart home environments to accessible transit in public spaces. Prior literature has investigated the usability of haptic messages presented via handheld devices or body-worn displays. The notion of using ubiquitous foot-floor contact to transmit similar information was investigated here for the first time, although vibrotactile communication with the foot has been previously proposed for musical performance [70], motor rehabilitation [206], or enhancing the use of an exercise machine [112].

This thesis also developed simple techniques for interacting with virtual ground material simulations and user interfaces realized via a distributed multimodal floor interface. In this approach, foot-floor interactions are mediated by cursor-like contact centroids, whose positions can be accurately estimated from intrinsic force measurements,. Similar results could be obtained via surface-mounted force sensing, but much larger numbers of sensing elements would be needed, increasing costs and complexity. A number of demonstration applications were presented, along with guidelines for touch-surface interface design based on an empirical study of their usability.

9.1.3 Perception

A broad hypothesis motivating this research was that vibration feedback that is similar to what is felt when stepping onto natural materials could evoke sensations of walking on the same materials [62, 241]. However, it was an unexpected result of this thesis that similar vibrations could compensate for missing kinesthetic information, due to a perceptual illusion in which the apparent compliance was increased when plantar vibration feedback was supplied. The observed effect proved highly reproducible, scaled monotonically with amplitude, depended only weakly on the vibration waveform used, and remained robust at vibration amplitudes near to the psychophysical detection threshold for the stimuli. Prior literature has studied the contribution of vibrotactile cues produced during the relative sliding of a hand and a surface to the perception of movement [242, 243, 244], but the relevance of these results to the effect observed here is unclear. The only pertinent haptic simulation we are aware of involves vibrations produced by a virtual rolling ball in a hand-held rod [79]. In addition, although postural effects of plantar vibration feedback have been documented in prior research, the effect observed here does not appear to be in any way directly related, as discussed in Chapter 6.

9.1.4 Mechanical Interactions

Mechanical interactions with complex, heterogeneous materials give rise to texture-like high-frequency vibrations whose random character can be effectively captured via statistical models. Chapter 7 presented algorithms for simulating stress fluctuations in fiber composite materials and compressed granular matter under load, based on variations of the widely studied fiber bundle model. The latter has been demonstrated to capture the most characteristic statistical properties of these systems despite its simplicity. The novel formulations presented here are based on an effective model that can be considered to represent a single stochastic fiber undergoing failure at successive, random levels of an applied strain. The results are the first practical algorithms for haptic synthesis of high-frequency fracture processes in quasi-brittle, heterogeneous materials. While there are some similarities between the aforementioned algorithms and stochastic models that have been used to render haptic surface textures associated with scraping solid objects, the latter have not been used to render textures produced through inelastic compression of stiff materials. Existing physically inspired algorithms for the synthesis of acoustic [59, 98] or haptic textures

(e.g., Chapters 4 and 5 and [62, 241]) in collective or volumetric material interactions can produce qualitatively evocative effects, but have heretofore been based on heuristics lacking in physical justification.

Haptic rendering of interactions with fracturing materials could, alternatively, be based on finite-element, mesh or point-based models like those used for rendering brittle fracture in computer graphics [92, 209]. A related model that has been used in scientific studies of spatial disorder in heterogeneous materials is the random spring model [11]. However, to the best of our knowledge none of these has ever been applied for haptic rendering. It appears unlikely that any of them may be usable for interactive simulation at moderately high spatial resolution and at the high sampling frequencies (several kHz) required for stable, accurate haptic rendering or for the synthesis of high-frequency vibrotactile effects, even granted severe speed-accuracy tradeoffs.

Chapter 8 of this thesis derived the statistical properties of irregular stick-slip oscillations accompanying shear sliding, through solutions of a novel first passage time problem associated with the motion. The results characterize motion in different sliding regimes observed in real or simulated frictional systems, and provide a statistical model of temporal irregularities arising from material disorder. In the context of virtual foot-ground interactions, they could be used to integrate material-dependent temporal irregularities in event-based models of stick-slip motion [218, 219].

9.2 Future Work

The most obvious application of the results of this thesis would be to aid the design of interactions with virtual ground surfaces in virtual or augmented reality, or with multimodal touch surface interfaces. The former could improve the sense of immersion or presence in the virtual environment, while the latter could improve the viability of human-computer interaction via the feet in diverse contexts like those discussed in Chapters 3 and 5.

The stochastic fracture and friction models developed here provide a physical basis for the development of haptic rendering algorithms that can preserve the characteristic fluctuations during complex physical interactions with disordered, heterogeneous materials. Chapter 7 presented models of fluctuations in fiber composite and compressed granular media based on a mean damage approximation to the inverse fiber bundle model, and as further discussed in Section 7.4, this could provide a basis for render local stress fluctuations

within larger effective volume elements whose constitutive response is obtained from a lower-rate simulation of a distributed, homogenized medium, based on finite element, point-based, or spring mesh methods.

Stick-slip motion accompanying displacement between rough or disordered surfaces is of fundamental interest in physics and material science, and the results presented in Chapter 8 may shed further light on the nature of friction-induced vibrations. Potential applications of these results can be envisaged in fields such as vibration control, brake noise reduction, or musical instrument analysis and simulation. In addition, while this investigation provided a novel description of irregular stick-slip motion as a stochastic resonance phenomenon, further research is needed to clarify the extent to which this may shed further light on the dynamics of sliding friction.

The ability of vibrations presented through an otherwise rigid floor surface to evoke an illusory sense of compliance suggests that vibrotactile channels play a larger role in the control of locomotion than has been previously acknowledged. This effect may find applications in the scientific study of human locomotion, and could lead to the development of gait rehabilitation techniques involving plantar vibration stimulation or to the development of vibrotactile orthotics. Further hints as to the potential for such applications were provided by preliminary observations that postural modifications are evoked during stepping onto a surface through which vibration feedback is supplied, although further analysis and research is needed. In addition, we have found, through informal investigations, that the same perceptual effect accompanies vibration feedback supplied to the hands, but this remains to be investigated in future work. If this is the case, it could be used to improve haptic virtual reality simulations for the hands, or to render virtual compliance effects associated with controls presented via manually operated touch screen interfaces.

References

- [1] J. Perry, *Gait analysis: normal and pathological function*. SLACK incorporated, 1992.
- [2] F. Galbraith and M. Barton, “Ground loading from footsteps,” *Journal of the Acoustical Society of America*, vol. 48, Jan 1970.
- [3] X. Li, R. J. Logan, and R. E. Pastore, “Perception of acoustic source characteristics: Walking sounds,” *Journal of the Acoustical Society of America*, vol. 90, no. 6, pp. 3036–3049, 1991.
- [4] A. Ekimov and J. Sabatier, “Vibration and sound signatures of human footsteps in buildings,” *Journal of the Acoustical Society of America*, vol. 120, Jan 2006.
- [5] B. G. Watters, “Impact noise characteristics of female hard-heeled foot traffic,” *J. Acoust. Soc. Am.*, vol. 37, pp. 619–630, 1965.
- [6] D. H. Cress, “Terrain considerations and data base development for the design and testing of devices to detect intruder-induced ground motion,” Tech. Rep. M-78-1, U.S. Army Engineer Waterways Experiment Station, Vicksburg, Miss., 1978.
- [7] A. Ekimov and J. Sabatier, “A review of human signatures in urban environments using acoustic and seismic methods,” in *Proc. of IEEE Technologies for Homeland Security*, 2008.
- [8] K. Houston and D. McGaffigan, “Spectrum analysis techniques for personnel detection using seismic sensors,” in *Proceedings of SPIE*, vol. 5090, p. 162, 2003.
- [9] A. Ebrahimpour, A. Hamam, R. L. Sack, and W. Patten, “Measuring and modeling dynamic loads imposed by moving crowds,” *Journal of Structural Engineering*, pp. 1468–1474, 1996.
- [10] H. Herrmann and S. Roux, *Statistical models for the fracture of disordered media*. North Holland, 1990.
- [11] M. Alava, P. Nukala, and S. Zapperi, “Statistical models of fracture,” *Advances in Physics*, vol. 55, no. 3, pp. 349–476, 2006.

-
- [12] F. Adjémian and P. Evesque, “Different regimes of stick-slip in granular matter: from quasi-periodicity to randomness,” *EGS XXVII General Assembly, Nice, 21-26 April 2002*, 2002.
- [13] A. Baldassarri, F. Dalton, A. Petri, S. Zapperi, G. Pontuale, and L. Pietronero, “Brownian forces in sheared granular matter,” *Physical Review Letters*, vol. 96, no. 11, p. 118002, 2006.
- [14] F. Dalton, F. Farrelly, A. Petri, L. Pietronero, L. Pitolli, and G. Pontuale, “Shear stress fluctuations in the granular liquid and solid phases,” *Physical Review Letters*, vol. 95, no. 13, p. 138001, 2005.
- [15] S. Nasuno, A. Kudrolli, and J. Gollub, “Friction in granular layers: hysteresis and precursors,” *Physical Review Letters*, vol. 79, no. 5, pp. 949–952, 1997.
- [16] S. Nasuno, A. Kudrolli, A. Bak, and J. Gollub, “Time-resolved studies of stick-slip friction in sheared granular layers,” *Physical Review E*, vol. 58, no. 2, pp. 2161–2171, 1998.
- [17] M. Trulsson, “Mechanoreceptive afferents in the human sural nerve,” *Experimental Brain Research*, vol. 137, no. 1, pp. 111–116, 2001.
- [18] P. M. Kennedy and J. T. Inglis, “Distribution and behaviour of glabrous cutaneous receptors in the human foot sole,” *Journal of Physiology*, vol. 583, no. 3, pp. 995–1002, 2002.
- [19] S. Weinstein, “Intensive and extensive aspects of tactile sensitivity as a function of body part, sex, and laterality,” in *The Skin Senses* (D. R. Kenshalo, ed.), Thomas, 1968.
- [20] C. Wells, L. M. Ward, R. Chua, and J. T. Inglis, “Regional Variation and Changes With Ageing in Vibrotactile Sensitivity in the Human Footsole,” *J Gerontol A Biol Sci Med Sci*, vol. 58, no. 8, pp. B680–686, 2003.
- [21] M. Morioka and M. J. Griffin, “Absolute thresholds for the perception of fore-and-aft, lateral, and vertical vibration at the hand, the seat, and the foot,” *Journal of Sound and Vibration*, vol. 314, no. 1-2, pp. 357–370, 2008.
- [22] A. Tax, B. van Wezel, and V. Dietz, “Bipedal reflex coordination to tactile stimulation of the sural nerve during human running,” *J Neurophysiology*, vol. 73, no. 5, 1995.
- [23] E. P. Zehr, R. B. Stein, and T. Komiyama, “Function of sural nerve reflexes during human walking,” *Journal of Physiology*, vol. 507, pp. 305–314, 1998.

-
- [24] S. Rossignol, R. Dubuc, and J. Gossard, "Dynamic sensorimotor interactions in locomotion," *Physiological Reviews*, vol. 86, no. 1, p. 89, 2006.
- [25] J. M. Kinsella-Shaw, B. Shaw, and M. T. Turvey, "Perceiving "walk-on-able" slopes," *Ecological Psychology*, vol. 4, no. 4, pp. 223–239, 1992.
- [26] D. Ferris, M. Louie, and C. Farley, "Running in the real world: adjusting leg stiffness for different surfaces.," *Proceedings of the Royal Society B: Biological Sciences*, vol. 265, no. 1400, p. 989, 1998.
- [27] S. Dixon, A. Collop, and M. Batt, "Surface effects on ground reaction forces and lower extremity kinematics in running.," *Med Sci Sports Exerc*, vol. 32, no. 11, pp. 1919–1926, 2000.
- [28] E. Hardin, A. van den Bogert, and J. Hamill, "Kinematic adaptations during running: effects of footwear, surface, and duration," *Medicine & Science in Sports & Exercise*, vol. 36, no. 5, p. 838, 2004.
- [29] C. Moritz and C. Farley, "Passive dynamics change leg mechanics for an unexpected surface during human hopping," *Journal of Applied Physiology*, vol. 97, no. 4, p. 1313, 2004.
- [30] C. Moritz, S. Greene, and C. Farley, "Neuromuscular changes for hopping on a range of damped surfaces," *Journal of Applied Physiology*, vol. 96, no. 5, p. 1996, 2004.
- [31] D. Marigold and A. Patla, "Adapting locomotion to different surface compliances: neuromuscular responses and changes in movement dynamics," *Journal of neurophysiology*, vol. 94, no. 3, p. 1733, 2005.
- [32] M. MacLellan and A. Patla, "Adaptations of walking pattern on a compliant surface to regulate dynamic stability," *Experimental Brain Research*, vol. 173, no. 3, pp. 521–530, 2006.
- [33] Y. Kobayashi, R. Osaka, T. Hara, and H. Fujimoto, "How accurately people can discriminate the differences of floor materials with various elasticities," *IEEE Transactions on Neural Systems and Rehabilitation Engineering*, vol. 16, no. 1, pp. 99–105, 2008.
- [34] T. Rosburg, "Tactile ground surface indicators in public places," in *Human Haptic Perception: Basics and Applications* (M. Grunwald, ed.), pp. 491–499, Basel, Boston, Berlin: Birkhäuser, 2008.
- [35] A. Courtney and H. M. Chow, "A study of tile design for tactile guide pathways," *International Journal of Industrial Ergonomics*, vol. 25, no. 6, pp. 693–698, 2000.

-
- [36] Y. Kobayashi, T. Takashima, M. Hayashi, and H. Fujimoto, "Gait analysis of people walking on tactile ground surface indicators," *IEEE Transactions on Neural Systems and Rehabilitation Engineering*, vol. 13, pp. 53–59, March 2005.
- [37] Y. Visell, F. Fontana, B. Giordano, R. Nordahl, S. Serafin, and R. Bresin, "Sound design and perception in walking interactions," *International Journal of Human-Computer Studies*, 2009.
- [38] B. Giordano, Y. Visell, J. R. Cooperstock, H. Yao, V. Hayward, and S. McAdams, "Non-visual identification of ground materials during walking," *Journal of the Acoustical Society of America*, (Submitted) 2010.
- [39] L. A. Jones and S. J. Lederman, *Human Hand Function*. Oxford University Press, 2006.
- [40] S. Ballesteros and M. A. Heller, "Haptic object identification," in *Human Haptic Perception: Basics and Applications* (M. Grunwald, ed.), pp. 207–222, Basel, Boston, Berlin: Birkhäuser, 2008.
- [41] S. J. Lederman and R. L. Klatzky, "Haptic perception: A tutorial," *Attention, Perception, & Psychophysics*, vol. 71, no. 7, pp. 1439–1459, 2009.
- [42] R. Klatzky and S. Lederman, "Tactile roughness perception with a rigid link interposed between skin and surface," *Perception and Psychophysics*, vol. 61, no. 4, pp. 591–607, 1999.
- [43] M. Hollins and S. Risner, "Evidence for the duplex theory of tactile texture perception.," *Perception & Psychophysics*, vol. 62, no. 4, pp. 695–705, 2000.
- [44] S. Bensmaia and M. Hollins, "The vibrations of texture.," *Somatosens Mot Res*, vol. 20, no. 1, pp. 33–43, 2003.
- [45] S. Bensmaia and M. Hollins, "Pacinian representations of fine surface texture," *Perception & psychophysics*, vol. 67, no. 5, p. 842, 2005.
- [46] R. Klatzky, S. Lederman, C. Hamilton, M. Grindley, and R. Swendsen, "Feeling textures through a probe: Effects of probe and surface geometry and exploratory factors," *Perception & Psychophysics*, vol. 65, no. 4, p. 613, 2003.
- [47] A. Okamura, J. Dennerlein, and R. Howe, "Vibration feedback models for virtual environments," in *1998 IEEE International Conference on Robotics and Automation, 1998. Proceedings*, vol. 1, 1998.
- [48] W. Schiff and E. Foulke, *Tactual perception: a sourcebook*. Cambridge Univ Pr, 1982.

-
- [49] M. Hollins, S. Bensmaïa, and E. Roy, “Vibrotaction and texture perception,” *Behavioural brain research*, vol. 135, no. 1-2, pp. 51–56, 2002.
- [50] M. Hollins, A. Fox, and C. Bishop, “Imposed vibration influences perceived tactile smoothness,” *Perception*, vol. 29, no. 12, pp. 1455–1466, 2000.
- [51] M. Slater, M. Usoh, and A. Steed, “Taking steps: the influence of a walking technique on presence in virtual reality,” *ACM Transactions on Computer-Human Interaction (TOCHI)*, vol. 2, no. 3, p. 219, 1995.
- [52] H. Iwata, “Haptic interface,” in *The Human-Computer Interaction Handbook* (A. Sears and J. A. Jacko, eds.), New York: Lawrence Erlbaum Assoc., 2nd ed., 2008.
- [53] J. Hollerbach, “Locomotion interfaces and rendering,” in *Haptic Rendering: Foundations, Algorithms and Applications* (M. Lin and M. Otaduy, eds.), A K Peters, Ltd, 2008.
- [54] D. Swapp, J. Williams, and A. Steed, “The implementation of a novel walking interface within an immersive display,” in *3D User Interfaces (3DUI), 2010 IEEE Symposium on*, pp. 71–74, IEEE, 2010.
- [55] J. Templeman, P. Denbrook, and L. Sibert, “Virtual locomotion: Walking in place through virtual environments,” *Presence*, vol. 8, no. 6, pp. 598–617, 1999.
- [56] S. Razzaque, Z. Kohn, and M. Whitton, “Redirected walking,” in *Proc of EUROGRAPHICS*, pp. 289–294, 2001.
- [57] K. E. MacLean, “Foundations of transparency in tactile information design,” *IEEE Transactions on Haptics*, vol. 1, no. 2, pp. 84–95, 2008.
- [58] P. Cook, “Modeling Bill’s Gait: Analysis and Parametric Synthesis of Walking Sounds,” *Proceedings of the AES 22nd International Conference on Virtual, Synthetic, and Entertainment Audio*, pp. 73–78, 2002.
- [59] P. Cook, *Real Sound Synthesis for Interactive Applications*. AK Peters, Ltd., 2002.
- [60] S. Papetti, F. Fontana, M. Civolani, A. Berrezag, and V. Hayward, “Audio-tactile Display of Ground Properties Using Interactive Shoes,” *Haptic and Audio Interaction Design*, pp. 117–128, 2010.
- [61] S. Serafin, L. Turchet, R. Nordahl, S. Dimitrov, A. Berrezag, and V. Hayward, “Identification of virtual grounds using virtual reality haptic shoes and sound synthesis,” *Proceedings of Eurohaptics*, p. 61, 2010.

-
- [62] Y. Visell, J. Cooperstock, B. L. Giordano, K. Franinovic, A. Law, S. McAdams, K. Jathal, and F. Fontana, “A vibrotactile device for display of virtual ground materials in walking,” in *Proceedings of Eurohaptics*, 2008.
- [63] J. Sinclair, P. Hingston, and M. Masek, “Considerations for the design of exergames,” in *Proc of the 5th Int ACM Conf on Comp Graphics and Interactive Techniques, Southeast Asia*, p. 295, 2007.
- [64] G. Pearson and M. Weiser, “Of moles and men: the design of foot controls for workstations,” in *Proc of the ACM SIGCHI conf on Human factors in Comp Sys*, pp. 333–339, ACM New York, NY, USA, 1986.
- [65] T. Augsten, K. Kaefer, R. Meusel, D. K. Caroline Fetzer, T. Stoff, T. Becker, C. Holz, and P. Baudisch, “Multitoe: High-precision interaction with back-projected floors based on high-resolution multi-touch input,” in *Proc. of UIST 2010*, 2010.
- [66] J. LaViola Jr, D. Feliz, D. Keefe, and R. Zeleznik, “Hands-free multi-scale navigation in virtual environments,” in *Proc of the 2001 symposium on Interactive 3D graphics*, pp. 9–15, ACM New York, NY, USA, 2001.
- [67] A. F. Rovers and H. van Essen, “Guidelines for haptic interpersonal communication applications,” *Virtual Reality*, vol. 9, pp. 177–191, 2006.
- [68] R. Velazquez, “On-shoe tactile display,” in *Proc. of the IEEE Intl. Workshop on Haptic Audio Visual Env. and Their Applications*, 2008.
- [69] J. A. Michon, ed., *Generic Intelligent Driver Support*. CRC Press, 1993.
- [70] J. Rován and V. Hayward, “Typology of tactile sounds and their synthesis in gesture-driven computer music performance,” in *Trends in Gestural Control of Music* (M. Wanderley and M. Battier, eds.), Editions IRCAM, 2000.
- [71] M. Addlesee, A. H. Jones, F. Livesey, and F. S. Samaria, “The ORL active floor,” *IEEE Personal Communications*, vol. 4, pp. 35–41, 1997.
- [72] T. Delbrueck, A. Whatley, R. Douglas, K. Eng, K. Hepp, and P. Verschure, “A tactile luminous floor for an interactive autonomous space,” *Robotics and Autonomous Systems*, vol. 55, no. 6, pp. 433–443, 2007.
- [73] R. J. Orr and G. D. Abowd, “The smart floor: a mechanism for natural user identification and tracking,” in *ACM CHI extended abstracts*, (New York, NY, USA), pp. 275–276, ACM, 2000.

-
- [74] J. Paradiso, C. Ablar, K.-y. Hsiao, and M. Reynolds, “The magic carpet: physical sensing for immersive environments,” in *ACM CHI extended abstracts*, (New York, NY, USA), pp. 277–278, ACM, 1997.
- [75] R. F. Pinkston, “A touch sensitive dance floor/midi controller,” *Journal of the Acoustical Society of America*, vol. 96, no. 5, pp. 3302–3302, 1994.
- [76] P. Srinivasan, D. Birchfield, G. Qian, and A. Kidané, “A pressure sensing floor for interactive media applications,” in *ACE '05: Proceedings of the 2005 ACM SIGCHI International Conference on Advances in computer entertainment technology*, (New York, NY, USA), pp. 278–281, ACM, 2005.
- [77] K. Yin and D. K. Pai, “Footsee: an interactive animation system,” in *SCA '03: Proceedings of the 2003 ACM SIGGRAPH/Eurographics symposium on Computer animation*, (Aire-la-Ville, Switzerland, Switzerland), pp. 329–338, Eurographics Association, 2003.
- [78] E. Miranda and M. Wanderley, *New Digital Musical Instruments: Control And Interaction Beyond the Keyboard*. AR Editions, 2006.
- [79] H. Yao and V. Hayward, “An experiment on length perception with a virtual rolling stone,” in *Proceedings of Eurohaptics*, pp. 325–330, 2006.
- [80] J. Romano, T. Yoshioka, and K. Kuchenbecker, “Automatic filter design for synthesis of haptic textures from recorded acceleration data,” in *Robotics and Automation (ICRA), 2010 IEEE International Conference on*, pp. 1815–1821, IEEE, 2010.
- [81] G. Champion and V. Hayward, “Fundamental Limits in the Rendering of Virtual Haptic Textures,” in *Proceedings of the First Joint Eurohaptics Conference and Symposium on Haptic Interfaces for Virtual Environment and Teleoperator Systems*, p. 270, IEEE Computer Society, 2005.
- [82] V. Hayward and K. Maclean, “Do it yourself haptics, Part I,” *IEEE Robotics and Automation Magazine*, vol. 14, December 2007.
- [83] H.-Y. Yao and V. Hayward, “Design and analysis of a recoil-type vibrotactile transducer,” *Journal of the Acoustical Society of America*, vol. 128, no. 2, pp. 619–627, 2010.
- [84] M. Lin and M. Otaduy, *Haptic rendering: foundations, algorithms, and applications*. AK Peters Ltd, 2008.
- [85] J. Smith, *Physical audio signal processing*. J. O. Smith, 2004.

-
- [86] N. Bell, Y. Yu, and P. Mucha, “Particle-based simulation of granular materials,” in *Proceedings of the 2005 ACM SIGGRAPH/Eurographics symposium on Computer animation*, p. 86, ACM, 2005.
- [87] Y. Zhu and R. Bridson, “Animating sand as a fluid,” in *Proceedings of the 2005 ACM SIGGRAPH/Eurographics Symposium on Computer Animation*, p. 972, ACM, 2005.
- [88] T. Lenaerts, B. Adams, and P. Dutré, “Porous flow in particle-based fluid simulations,” *ACM Transactions on Graphics (TOG)*, vol. 27, no. 3, p. 49, 2008.
- [89] K. Hirota, Y. Tanoue, and T. Kaneko, “Generation of crack patterns with a physical model,” *The Visual Computer*, vol. 14, no. 3, pp. 126–137, 1998.
- [90] A. Norton, G. Turk, B. Bacon, J. Gerth, and P. Sweeney, “Animation of fracture by physical modeling,” *The Visual Computer*, vol. 7, no. 4, pp. 210–219, 1991.
- [91] J. O’Brien and J. Hodgins, “Graphical modeling and animation of brittle fracture,” in *Proc of the 26th annual conference on Computer graphics and interactive techniques*, pp. 137–146, ACM Press/Addison-Wesley Publishing Co. New York, NY, USA, 1999.
- [92] M. Pauly, R. Keiser, B. Adams, P. Dutré, M. Gross, and L. Guibas, “Meshless animation of fracturing solids,” *Proceedings of the 2005 ACM SIGGRAPH/Eurographics Symposium on Computer Animation*, vol. 24, no. 3, pp. 957–964, 2005.
- [93] C. Zheng and D. James, “Rigid-body fracture sound with precomputed soundbanks,” *ACM Transactions on Graphics (TOG)*, vol. 29, no. 4, pp. 1–13, 2010.
- [94] J. Siira and D. Pai, “Haptic texturing—a stochastic approach,” in *IEEE International Conference on Robotics and Automation*, pp. 557–562, 1996.
- [95] D. Green and J. Salisbury, “Texture sensing and simulation using the PHANToM: Towards remote sensing of soil properties,” in *Proceedings of the Second PHANToM Users Group Workshop*, pp. 19–22, 1997.
- [96] F. Avanzini, S. Serafin, and D. Rocchesso, “Interactive simulation of rigid body interaction with friction-induced sound generation,” *IEEE Transactions on Speech and Audio Processing*, vol. 13, no. 5, p. 1073, 2005.
- [97] A. J. Farnell, “Marching onwards – procedural synthetic footsteps for video games and animation,” in *Proceedings of the Pd Convention*, 2007.
- [98] F. Fontana and R. Bresin, “Physics-based sound synthesis and control: crushing, walking and running by crumpling sounds,” in *Proc. Colloquium on Musical Informatics*, (Florence, Italy), pp. 109–114, May 2003.

-
- [99] F. Avanzini and D. Rocchesso, "Modeling Collision Sounds: Non-linear Contact Force," *Proc. COST-G6 Conf. Digital Audio Effects (DAFX-01)*, pp. 61–66, 2001.
- [100] A. Wilska, "On the vibrational sensitivity in different regions of the body surface," *Acta Physiologica Scandinavica*, vol. 31, pp. 285–289, 1954.
- [101] M. Trulsson, "Microreceptive afferents in the human sural nerve," *Exp Brain Res*, vol. 137, pp. 111–116, 2001.
- [102] E. Ribot-Ciscar, J. P. Vedel, and J. P. Roll, "Vibration sensitivity of slowly and rapidly adapting cutaneous mechanoreceptors in the human foot and leg," *Neuroscience Letters*, vol. 104, no. 130–135, 1989.
- [103] J. Inglis, P. Kennedy, C. Wells, and R. Chua, "The role of cutaneous receptors in the foot," *Adv Exp Med Biol.*, vol. 508, pp. 111–117, 2002.
- [104] Y. Visell, "Tactile sensory substitution: Models for enactment in HCI," *Interacting with Computers*, vol. (In press), 2009.
- [105] A. Gallace, H. Z. Tan, and C. Spence, "The body surface as a communication system: The state of the art after 50 years," *Presence: Teleoper. Virtual Environ.*, vol. 16, no. 6, pp. 655–676, 2007.
- [106] G. A. Gescheider and R. T. Verrillo, "Vibrotactile frequency characteristics as determined by adaptation and masking procedures," in *Sensory Functions of the Skin of Humans* (D. R. Kenshalo, ed.), Plenum, 1978.
- [107] E. Ribot-Ciscar, J. P. Roll, and G. M. Gauthier, "Comparative effects of whole body vibration on sensorimotor performance achieved with a mini-stick and a macro-stick in force and position control modes," *Aviat. Space Environ. Med.*, vol. 57, pp. 792–799, 1986.
- [108] J. P. Roll and J. C. Gilhodes, "Proprioceptive sensory codes mediating movement trajectory perception: human hand vibration-induced drawing illusions," *Canadian J. of Physiology and Pharmacology*, vol. 73, no. 2, pp. 295–304, 1995.
- [109] A. Priplata, J. Niemi, M. Salen, J. Harry, L. A. Lipsitz, and J. J. Collins, "Noise-enhanced human balance control," *Physical Review Letters*, vol. 89, no. 23, p. 238101, 2002.
- [110] A. W. Law, B. V. Peck, Y. Visell, P. G. Kry, and J. R. Cooperstock, "A multi-modal floor-space for displaying material deformation underfoot in virtual reality," in *Proc. of the IEEE Intl. Workshop on Haptic Audio Visual Environments and Their Applications*, 2008.

-
- [111] L. A. Jones and N. B. Sarter, "Tactile displays: Guidance for their design and application," *Human Factors*, vol. 50, no. 1, pp. 90–111, 2008.
- [112] A. R. Ferber, M. Peshkin, and J. E. Colgate, "Using haptic communications with the leg to maintain exercise intensity," in *Proc. of 16th IEEE International Conference on Robot and Human Interactive Communication (RO-MAN)*, 2007.
- [113] A. A. Priplata, B. L. Patritti, J. B. Niemi, R. Hughes, D. C. Gravelle, L. A. Lipsitz, A. Veves, J. Stein, P. Bonato, and J. J. Collins, "Noise-enhanced balance control in patients with diabetes and patients with stroke," *Annals of Neurology*, vol. 59, no. 1, pp. 4–12, 2006.
- [114] J. Hijmans, J. Geertzen, B. Schokker, and K. Postema, "Development of vibrating insoles," *Int J Rehabil Res*, vol. 30, no. 4, 2007.
- [115] L. M. Brown, S. A. Brewster, and H. C. Purchase, "Tactile crescendos and sforzandos: Applying musical techniques to tactile icon design," in *Proc. of the ACM 2006 Conference on Human Factors in Computing Systems*, 2006.
- [116] J. B. F. van Erp and M. M. A. Spape, "Distilling the underlying dimensions of tactile melodies," in *Proceedings of Eurohaptics*, 2003.
- [117] D. Ternes and K. E. MacLean, "Designing large sets of haptic icons with rhythm," in *Proceedings of Eurohaptics*, 2008.
- [118] W. H. Warren and R. R. Verbrugge, "Auditory perception of breaking and bouncing events: a case study in ecological acoustics," *Journal of Experimental Psychology: Human Perception and Performance*, vol. 10, no. 5, 1984.
- [119] C. Cadoz, "Instrumental gesture and musical composition," in *Proc. of the Intl. Computer Music Conf. (ICMC)*, International Computer Music Association, 1988.
- [120] D. Arfib, "Digital synthesis of complex spectra by means of multiplication of non-linear distorted sine waves," *Journal of the Audio Engineering Society*, vol. 27, no. 10, pp. 757–779, 1979.
- [121] D. Rocchesso and F. Fontana, eds., *The Sounding Object*. Florence, Italy: Edizioni di Mondo Estremo, 2003.
- [122] K. H. Hunt and F. R. E. Crossley, "Coefficient of restitution interpreted as damping in vibroimpact," *ASME Journal of Applied Mechanics*, vol. 42, no. 2, pp. 440–445, 1975.

-
- [123] E. Hoggan and S. Brewster, “Designing audio and tactile crossmodal icons for mobile devices,” in *Proceedings of the 2007 ACM Intl. Conference on Multimodal Interfaces*, 2007.
- [124] M. Enriquez, K. E. MacLean, and C. Chita, “Haptic phonemes: Basic building blocks of haptic communication,” in *Proceedings of the 2006 ACM International Conference on Multimodal Interfaces*, 2006.
- [125] S. A. Brewster, “Non-speech auditory output,” in *The Human-Computer Interaction Handbook* (A. Sears and J. A. Jacko, eds.), New York: Lawrence Erlbaum Assoc., 2nd ed., 2008.
- [126] Y. Visell, A. Law, J. Ip, S. Smith, and J. R. Cooperstock, “Interaction Capture in Immersive Virtual Environments via an Intelligent Floor Surface,” in *Proc. of IEEE Virtual Reality*, 2010 (To appear).
- [127] Y. Visell, A. Law, S. Smith, J. Ip, R. Rajalingham, and J. Cooperstock, “Contact sensing and interaction techniques for a distributed multimodal floor display,” in *Proceedings of the 2010 IEEE Symposium on 3D User Interfaces (3DUI)*, 2010.
- [128] Y. Visell, J. Cooperstock, B. Giordano, K. Franinovic, A. Law, S. McAdams, K. Jathal, and F. Fontana, “A Vibrotactile Device for Display of Virtual Ground Materials in Walking,” *Lecture Notes in Computer Science*, vol. 5024, p. 420, 2008.
- [129] I. Poupyrev, S. Maruyama, and J. Rekimoto, “Ambient touch: designing tactile interfaces for handheld devices,” in *Proceedings of UIST*, ACM, 2002.
- [130] M. Fukumoto and T. Sugimura, “Active click: tactile feedback for touch panels,” in *ACM CHI extended abstracts*, pp. 121–122, ACM, 2001.
- [131] A. Nashel and S. Razzaque, “Tactile virtual buttons for mobile devices,” in *Proceedings of CHI*, pp. 854–855, ACM, 2003.
- [132] H. Yao, V. Hayward, and R. Ellis, “A tactile enhancement instrument for minimally invasive surgery,” *Computer Aided Surgery*, vol. 10, no. 4, pp. 233–239, 2005.
- [133] K. Kuchenbecker, J. Fiene, *et al.*, “Improving contact realism through event-based haptic feedback,” *IEEE Transactions on Visualization and Computer Graphics*, pp. 219–230, 2006.
- [134] V. Hayward and K. Maclean, “Do It Yourself Haptics: Part I,” *IEEE Robotics & Automation Magazine*, p. 89, 2007.
- [135] L. Meirovitch, *Dynamics and control of structures*. John Wiley & Sons, 1990.

-
- [136] F. Fahy, *Foundations of engineering acoustics*. Academic Press, 2001.
- [137] N. Fletcher and T. Rossing, *The physics of musical instruments*. Springer Verlag, 1998.
- [138] H. Tramberend, F. Hasenbrink, G. Eckel, U. Lechner, and M. Goebel, “CyberStage – An Advanced Virtual Environment,” *ERCIM News*, vol. 31, October 1997.
- [139] M. Magana and R. Velazquez, “On-shoe tactile display,” in *Proc. of the IEEE Intl Workshop on Haptic Audiovisual Environments and Games*, 2008.
- [140] A. Rovers and H. Van Essen, “Guidelines for haptic interpersonal communication applications: an exploration of foot interaction styles,” *Virtual Reality*, vol. 9, no. 2, pp. 177–191, 2006.
- [141] A. Priplata, J. Niemi, J. Harry, L. Lipsitz, and J. Collins, “Vibrating insoles and balance control in elderly people,” *The Lancet*, vol. 362, no. 9390, pp. 1123–1124, 2003.
- [142] J. Hollerbach, “Locomotion interfaces and rendering,” *Haptic Rendering: Foundations, Algorithms and Applications*. AK Peters, Ltd, 2008.
- [143] J. Sabatier and A. Ekimov, “A Review of Human Signatures in Urban Environments Using Seismic and Acoustic Methods,” in *2008 IEEE Conference on Technologies for Homeland Security*, pp. 215–220, 2008.
- [144] G. Burdea and M. Akay, *Force and touch feedback for virtual reality*. Wiley New York, 1996.
- [145] J. Fiene, K. Kuchenbecker, and G. Niemeyer, “Event-based haptics with grip force compensation,” in *Proc IEEE Haptic Symposium*, 2006.
- [146] S. J. Dixon and A. Cooke, “Shoe-surface interaction in tennis,” in *Biomedical engineering principles in sports* (G. K. Hung and J. M. Pallis, eds.), ch. 6, pp. 125–182, New York: Kluwer Academic, 2004.
- [147] V. H. Stile, I. T. James, S. J. Dixon, and I. N. Guisasola, “Natural turf surfaces: the case for continued research,” *Sports medicine*, vol. 39, no. 1, pp. 65–84, 2009.
- [148] S. Barrass and M. Adcock, “Interactive granular synthesis of haptic contact sounds,” in *AES 22nd International Conference on Virtual, Synthetic and Entertainment Audio*, 2002.
- [149] A. Crossan, J. Williamson, and R. Murray-Smith, “Haptic granular synthesis: Targeting, visualisation and texturing,” in *Proc. Intl Symposium on Non-visual & Multimodal Visualization*, pp. 527–532, 2004.

- [150] V. Hayward, "Physically-based haptic synthesis," in *Haptic Rendering: Foundations, Algorithms and Applications* (M. Lin and M. Otaduy, eds.), AK Peters, Ltd, 2007.
- [151] M. Mahvash and V. Hayward, "Haptic rendering of cutting: A fracture mechanics approach," *Haptics-e*, vol. 2, no. 3, pp. 1–12, 2001.
- [152] Y. Visell, A. Law, and J. Cooperstock, "Touch Is Everywhere: Floor Surfaces as Ambient Haptic Interfaces," *IEEE Transactions on Haptics*, 2009.
- [153] J. Kee Paik, A. Thayamballi, and G. Sung Kim, "The strength characteristics of aluminum honeycomb sandwich panels," *Thin-walled structures*, vol. 35, no. 3, pp. 205–231, 1999.
- [154] S. Rapoport, J. Mizrahi, E. Kimmel, O. Verbitsky, and E. Isakov, "Constant and Variable Stiffness and Damping of the Leg Joints in Human Hopping," *Journal of Biomechanical Engineering*, vol. 125, 2001.
- [155] D. Marigold and A. Patla, "Adapting locomotion to different surface compliances: neuromuscular responses and changes in movement dynamics," *Journal of neurophysiology*, vol. 94, no. 3, p. 1733, 2005.
- [156] C. Farley and O. Gonzalez, "Leg stiffness and stride frequency in human running," *Journal of Biomechanics*, vol. 29, no. 2, pp. 181–186, 1996.
- [157] L. Zhang, D. Xu, M. Makhsous, and F. Lin, "Stiffness and viscous damping of the human leg," in *24th Annual Meeting, American Society of Biomechanics, Chicago, IL*, 2000.
- [158] T. A. Kern, "Modeling the User," in *Engineering Haptic Devices* (T. A. Kern, ed.), Springer Verlag, 2009.
- [159] S. Bensmaia and M. Hollins, "Complex tactile waveform discrimination," *Journal of the Acoustical Society of America*, vol. 108, p. 1236, 2000.
- [160] J. Taylor and Q. Huang, *CRC Handbook of Electrical Filters*. CRC, 1997.
- [161] K. Chandrashekhara and A. Agarwal, "Active vibration control of laminated composite plates using piezoelectric devices: a finite element approach," *Journal of Intelligent Material Systems and Structures*, vol. 4, no. 4, p. 496, 1993.
- [162] U. Stobener and L. Gaul, "Modal vibration control for PVDF coated plates," *Journal of Intelligent Material Systems and Structures*, vol. 11, no. 4, p. 283, 2000.
- [163] N. Tanaka and T. Sanada, "Modal control of a rectangular plate using smart sensors and smart actuators," *Smart Materials and Structures*, vol. 16, no. 1, pp. 36–46, 2007.

-
- [164] A. Schmidt, M. Strohbach, K. v. Laerhoven, A. Friday, and H.-W. Gellersen, "Context acquisition based on load sensing," in *UbiComp '02: Proceedings of the 4th international conference on Ubiquitous Computing*, (London, UK), pp. 333–350, Springer-Verlag, 2002.
- [165] L. Wauben, M. van Veelen, D. Gossot, and R. Goossens, "Application of ergonomic guidelines during minimally invasive surgery: a questionnaire survey of 284 surgeons," *Surgical endoscopy*, vol. 20, no. 8, pp. 1268–1274, 2006.
- [166] Y. Visell and J. Cooperstock, "Optimized Design of a Vibrotactile Display via a Rigid Surface," in *Proc. of IEEE Haptics Symposium*, 2010.
- [167] A. Bicchi, J. Salisbury, and D. Brock, "Contact sensing from force measurements," *The Int J of Robotics Research*, vol. 12, no. 3, p. 249, 1993.
- [168] K. Hunt and F. Crossley, "Coefficient of restitution interpreted as damping in vibroimpact," *Journal of Applied Mechanics*, vol. 42, p. 440, 1975.
- [169] M. Kaltenbrunner, T. Bovermann, R. Bencina, and E. Costanza, "Tuio: A protocol for table-top tangible user interfaces," in *Proc of Gesture Workshop 2005*, Gesture Workshop, 2005.
- [170] I. MacKenzie, "Fitts' law as a research and design tool in human-computer interaction," *Human-Computer Interaction*, vol. 7, no. 1, pp. 91–139, 1992.
- [171] J. Jacko and A. Sears, *The human-computer interaction handbook: fundamentals, evolving technologies, and emerging applications*. Lawrence Erlbaum Assoc Inc, 2003.
- [172] P. Albinsson and S. Zhai, "High precision touch screen interaction," in *Proc of the ACM SIGCHI conference on Human factors in computing systems*, pp. 105–112, ACM New York, NY, USA, 2003.
- [173] R. L. Potter, L. J. Weldon, and B. Shneiderman, "Improving the accuracy of touch screens: an experimental evaluation of three strategies," in *CHI '88: Proc of the SIGCHI conference on Human factors in computing systems*, (New York, NY, USA), pp. 27–32, ACM, 1988.
- [174] E. Hoffmann, "A comparison of hand and foot movement times.," *Ergonomics*, vol. 34, no. 4, p. 397, 1991.
- [175] R. Simmons, C. Richardson, and R. Pozos, "Postural stability of diabetic patients with and without cutaneous sensory deficit in the foot," *Diabetes Research and Clinical Practice*, vol. 36, no. 3, pp. 153–160, 1997.

- [176] G. Simoneau, J. Ulbrecht, J. Derr, M. Becker, and P. Cavanagh, "Postural instability in patients with diabetic sensory neuropathy.," *Diabetes Care*, vol. 17, no. 12, p. 1411, 1994.
- [177] M. Mueller, S. Minor, S. Sahrman, J. Schaaf, and M. Strube, "Differences in the gait characteristics of patients with diabetes and peripheral neuropathy compared with age-matched controls," *Physical Therapy*, vol. 74, no. 4, p. 299, 1994.
- [178] F. Stål, P. A. Fransson, M. Magnusson, and M. Karlberg, "Effects of hypothermic anesthesia of the feet on vibration-induced body sway and adaptation," *Journal of Vestibular Research*, vol. 13, no. 1, pp. 39–52, 2003.
- [179] R. Harper and S. S. Stevens, "Subjective hardness of compliant materials," *Quarterly Journal of Experimental Psychology*, vol. 16, pp. 204–215, 1964.
- [180] G. Scott-Blair and F. Coppen, "The subjective judgement of the elastic and plastic properties of soft bodies," *British Journal of Psychology*, vol. 31, pp. 61–79, 1940.
- [181] F. Freyberger and B. Färber, "Compliance discrimination of deformable objects by squeezing with one and two fingers," in *Proceedings of Eurohaptics*, vol. 2006, pp. 271–276, 2006.
- [182] H. Tan, N. Durlach, G. Beauregard, and M. Srinivasan, "Manual discrimination of compliance using active pinch grasp: The roles of force and work cues," *Perception and Psychophysics*, vol. 57, no. 4, pp. 495–510, 1995.
- [183] M. Srinivasan and R. LaMotte, "Tactual discrimination of softness," *Journal of Neurophysiology*, vol. 73, no. 1, p. 88, 1995.
- [184] R. LaMotte, "Softness discrimination with a tool," *Journal of Neurophysiology*, vol. 83, no. 4, p. 1777, 2000.
- [185] R. Friedman, K. Hester, B. Green, and R. LaMotte, "Magnitude estimation of softness," *Experimental brain research*, vol. 191, no. 2, pp. 133–142, 2008.
- [186] W. Bergmann Tiest and A. Kappers, "Cues for haptic perception of compliance," *IEEE Transactions on Haptics*, vol. 2, no. 4, pp. 189–199, 2009.
- [187] L. A. Jones and I. W. Hunter, "A perceptual analysis of stiffness," *Experimental Brain Research*, vol. 79, pp. 150–156, 1990.
- [188] R. Howe and M. Cutkosky, "Sensing skin acceleration for slip and texture perception," in *Proc. IEEE International Conference on Robotics and Automation*, vol. 1, pp. 145–150, 1989.

-
- [189] B. L. Giordano, S. McAdams, Y. Visell, J. Cooperstock, H. Yao, and V. Hayward, “Non-visual identification of walking grounds,” *Journal of the Acoustical Society of America*, vol. 123, no. 5, p. 3412, 2008.
- [190] P. F. Meyer, L. I. E. Oddsson, and C. J. D. Luca, “The role of plantar cutaneous sensation in unperturbed stance,” *Experimental brain research*, vol. 156, no. 4, pp. 505–512, 2004.
- [191] J. M. Donelan, R. Kram, and A. D. Kuo, “Mechanical work for step-to-step transitions is a major determinant of the metabolic cost of human walking,” *Journal of Experimental Biology*, vol. 205, no. 23, pp. 3717–3727, 2002.
- [192] T. Lockhart, J. Woldstad, J. Smith, and J. Ramsey, “Effects of age related sensory degradation on perception of floor slipperiness and associated slip parameters,” *Safety science*, vol. 40, no. 7-8, pp. 689–703, 2002.
- [193] R. Roll, A. Kavounoudias, and J. Roll, “Cutaneous afferents from human plantar sole contribute to body posture awareness,” *Neuroreport*, vol. 13, no. 15, p. 1957, 2002.
- [194] A. Kavounoudias, R. Roll, and J. Roll, “The plantar sole is a ‘dynamometric map’ for human balance control,” *Neuroreport*, vol. 9, no. 14, p. 3247, 1998.
- [195] C. Maurer, T. Mergner, B. Bolha, and F. Hlavacka, “Human balance control during cutaneous stimulation of the plantar soles,” *Neuroscience letters*, vol. 302, no. 1, pp. 45–48, 2001.
- [196] C. Thompson, M. Bélanger, and J. Fung, “Effects of plantar cutaneo-muscular and tendon vibration on posture and balance during quiet and perturbed stance,” *Human Movement Science*, p. In press, 2010.
- [197] Y. Ivanenko, R. Grasso, and F. Lacquaniti, “Influence of leg muscle vibration on human walking,” *Journal of Neurophysiology*, vol. 84, no. 4, p. 1737, 2000.
- [198] G. Courtine, A. D. Nunzio, M. Schmid, M. Beretta, and M. Schieppati, “Stance- and locomotion-dependent processing of vibration-induced proprioceptive inflow from multiple muscles in humans,” *Journal of neurophysiology*, vol. 97, no. 1, p. 772, 2007.
- [199] S. Verschueren, S. Swinnen, K. Desloovere, and J. Duysens, “Effects of tendon vibration on the spatiotemporal characteristics of human locomotion,” *Experimental brain research*, vol. 143, no. 2, pp. 231–239, 2002.
- [200] Y. Visell and J. R. Cooperstock, “Design of a vibrotactile display via a rigid surface,” in *Proc. of the IEEE Haptics Symposium*, 2010.

-
- [201] A. Oppenheim and R. Schaffer, “Discrete-time signal processing,” *Prentice Hall Signal Processing*, p. 1120, 2009.
- [202] W. Lecluyse and R. Meddis, “A simple single-interval adaptive procedure for estimating thresholds in normal and impaired listeners,” *Journal of the Acoustical Society of America*, vol. 126, p. 2570, 2009.
- [203] Y. Leung, S. Bensmaia, S. Hsiao, and K. Johnson, “Time-course of vibratory adaptation and recovery in cutaneous mechanoreceptive afferents,” *Journal of neurophysiology*, vol. 94, no. 5, p. 3037, 2005.
- [204] S. Bensmaia, Y. Leung, S. Hsiao, and K. Johnson, “Vibratory adaptation of cutaneous mechanoreceptive afferents,” *Journal of neurophysiology*, vol. 94, no. 5, p. 3023, 2005.
- [205] A. Priplata, J. Niemi, M. Salen, J. Harry, L. Lipsitz, and J. Collins, “Noise-enhanced human balance control,” *Physical Review Letters*, vol. 89, no. 23, p. 238101, 2002.
- [206] P. Novak and V. Novak, “Effect of step-synchronized vibration stimulation of soles on gait in Parkinson’s disease: a pilot study,” *Journal of NeuroEngineering and Rehabilitation*, vol. 3, no. 1, p. 9, 2006.
- [207] I. Reiweger, J. Schweizer, J. Dual, and H. Herrmann, “Modelling snow failure with a fibre bundle model,” *Journal of Glaciology*, vol. 55, no. 194, pp. 997–1002, 2009.
- [208] S. Pradhan, A. Hansen, and B. Chakrabarti, “Failure processes in elastic fiber bundles,” *Reviews of Modern Physics*, vol. 82, no. 1, pp. 499–555, 2010.
- [209] E. Parker and J. O’Brien, “Real-time deformation and fracture in a game environment,” in *Proceedings of the 2009 ACM SIGGRAPH/Eurographics Symposium on Computer Animation*, pp. 165–175, ACM, 2009.
- [210] R. Hidalgo, F. Kun, and H. Herrmann, “Slow relaxation of fiber composites, variable range of interaction approach,” *Physica A: Statistical Mechanics and its Applications*, vol. 347, pp. 402–410, 2005.
- [211] F. Kun, Y. Moreno, R. Hidalgo, and H. Herrmann, “Creep rupture has two universality classes,” *EPL (Europhysics Letters)*, vol. 63, p. 347, 2003.
- [212] L. Devroye, *Non-Uniform Random Variate Generation*. Springer Verlag, 1986.
- [213] F. Kun, S. Zapperi, and H. Herrmann, “Damage in fiber bundle models,” *The European Physical Journal B-Condensed Matter and Complex Systems*, vol. 17, no. 2, pp. 269–279, 2000.

- [214] R. Hidalgo, C. Grosse, F. Kun, H. Reinhardt, and H. Herrmann, “Evolution of percolating force chains in compressed granular media,” *Physical review letters*, vol. 89, no. 20, p. 205501, 2002.
- [215] R. C. Hidalgo, H. J. Herrmann, F. Kun, and E. Partelli, “Force chains in granular packings,” in *The Physics of Complex Systems* (F. Mallamace and H. Stanley, eds.), Amsterdam: IOS Press, 2004.
- [216] R. Koerner, W. McCabe, and A. Lord Jr, “Acoustic emission behavior and monitoring of soils,” in *Acoustic emissions in geotechnical engineering practice: a symposium*, p. 93, ASTM International, 1981.
- [217] R. Hidalgo, F. Kun, and H. Herrmann, “Bursts in a fiber bundle model with continuous damage,” *Physical Review E*, vol. 64, no. 6, p. 66122, 2001.
- [218] M. Konyo, H. Yamada, S. Okamoto, and S. Tadokoro, “Alternative Display of Friction Represented by Tactile Stimulation without Tangential Force,” *Haptics: Perception, Devices and Scenarios*, pp. 619–629, 2008.
- [219] A. Nahvi, J. Hollerbach, R. Freier, and D. Nelson, “Display of friction in virtual environments based on human finger pad characteristics,” in *Proc. ASME Dynamic Systems and Control Division, DSC*, vol. 64, pp. 179–184, 1998.
- [220] R. Stratonovich, *Topics in the theory of random noise*. Gordon and Breach, 1967.
- [221] M. Bengisu and A. Akay, “Stick–slip oscillations: Dynamics of friction and surface roughness,” *The Journal of the Acoustical Society of America*, vol. 105, p. 194, 1999.
- [222] J. Woodhouse, “Physical modeling of bowed strings,” *Computer Music Journal*, vol. 16, no. 4, 1992.
- [223] A. Socoliuc, R. Bennewitz, E. Gnecco, and E. Meyer, “Transition from stick-slip to continuous sliding in atomic friction: entering a new regime of ultralow friction,” *Physical review letters*, vol. 92, no. 13, p. 134301, 2004.
- [224] B. N. J. Persson, *Sliding Friction, Physical Properties and Applications*. Springer, Berlin, 2nd ed., 2000.
- [225] A. Johansen, P. Dimon, C. Ellegaard, J. Larsen, and H. Rugh, “Dynamic phases in a spring-block system,” *Physical Review E*, vol. 48, no. 6, pp. 4779–4790, 1993.
- [226] A. Lima, C. Moukarzel, I. Grosse, and T. Penna, “Sliding blocks with random friction and absorbing random walks,” *Physical Review E*, vol. 61, no. 3, pp. 2267–2271, 2000.

- [227] A. Mauger, “Anomalous motion generated by the Coulomb friction in the Langevin equation,” *Physica A: Statistical Mechanics and its Applications*, vol. 367, pp. 129–135, 2006.
- [228] S. L. Qiao and R. A. Ibrahim, “Stochastic dynamics of systems with friction-induced vibration,” *Journal of Sound and Vibration*, vol. 223, no. 1, pp. 115–140, 1999.
- [229] S. Redner, *A guide to first-passage processes*. Cambridge Univ Press, 2001.
- [230] V. Brito and M. Gomes, “Block avalanches on a chute,” *Physics Letters A*, vol. 201, no. 1, pp. 38–41, 1995.
- [231] T. Verechtchaguina, I. Sokolov, and L. Schimansky-Geier, “First passage time densities in resonate-and-fire models,” *Physical Review E*, vol. 73, no. 3, p. 31108, 2006.
- [232] L. Gammaitoni, P. Hänggi, P. Jung, and F. Marchesoni, “Stochastic resonance,” *Reviews of Modern Physics*, vol. 70, no. 1, pp. 223–287, 1998.
- [233] C. Gardiner, *Handbook of stochastic methods*. Springer Berlin, 1985.
- [234] H. Risken, *The Fokker-Planck equation: Methods of solution and applications*. Springer Verlag, 1996.
- [235] N. G. van Kampen, *Stochastic processes in physics and chemistry*. North Holland, 1992.
- [236] T. Verechtchaguina, I. Sokolov, and L. Schimansky-Geier, “First passage time densities in non-Markovian models with subthreshold oscillations,” *EPL (Europhysics Letters)*, vol. 73, p. 691, 2006.
- [237] M. Wang and G. Uhlenbeck, “On the theory of the Brownian motion II,” *Reviews of Modern Physics*, vol. 17, no. 2-3, pp. 323–342, 1945.
- [238] S. Chandrasekhar, “Dynamical Friction. I. General Considerations: the Coefficient of Dynamical Friction,” *The Astrophysical Journal*, vol. 97, p. 255, 1943.
- [239] S. Rice, “Mathematical theory of random noise,” *Bell. System Tech. J.*, vol. 25, pp. 46–156, 1945.
- [240] G. Csernák, G. Stépán, and S. Shaw, “Sub-harmonic resonant solutions of a harmonically excited dry friction oscillator,” *Nonlinear Dynamics*, vol. 50, no. 1, pp. 93–109, 2007.
- [241] R. Nordahl, A. Berrezag, S. Dimitrov, L. Turchet, V. Hayward, and S. Serafin, “Preliminary experiment combining virtual reality haptic shoes and audio synthesis,” in *Proceedings of Eurohaptics*, vol. 6192 of *LNCS*, Springer, 2010.

-
- [242] E. Meftah, L. Belingard, A. Depeault, and C. Chapman, “Relative effects of spatial and temporal characteristics of scanned surfaces on human tactile perception of speed,” *Abstracts Society of Neuroscience*, vol. 626, no. 4, 2005.
- [243] B. Edin, G. Essick, M. Trulsson, and K. Olsson, “Receptor encoding of moving tactile stimuli in humans. I. Temporal pattern of discharge of individual low-threshold mechanoreceptors,” *Journal of Neuroscience*, vol. 15, no. 1, p. 830, 1995.
- [244] B. Whitsel, O. Franzen, D. Dreyer, M. Hollins, M. Young, G. Essick, and C. Wong, “Dependence of subjective traverse length on velocity of moving tactile stimuli,” *Somatosensory and Motor Research*, vol. 3, no. 3, pp. 185–196, 1986.